COMPUTATIONAL MODELING OF ELECTRICAL AND PHONON PROPERTIES

OF SKUTTERUDITES AND TWO-DIMENSIONAL TRANSITION METAL

DICHALCOGENIDES

by

Izaak Gene Williamson

A dissertation

submitted in partial fulfillment

of the requirements for the degree of

Doctorate of Philosophy in Materials Science and Engineering

Boise State University

May 2017

BOISE STATE UNIVERSITY GRADUATE COLLEGE

DEFENSE COMMITTEE AND FINAL READING APPROVALS

of the dissertation submitted by

Izaak Gene Williamson

Dissertation Title: Computational Modeling of Electrical and Phonon Properties of Skutterudites and Two-Dimensional Transition Metal Dichalcogenides

Date of Final Oral Examination: 24 March 2017

The following individuals read and discussed the dissertation submitted by student Izaak Gene Williamson, and they evaluated his presentation and response to questions during the final oral examination. They found that the student passed the final oral examination.

Lan Li, Ph.D.   Co-Chair, Supervisory Committee

Rick Ubic, Ph.D.   Co-Chair, Supervisory Committee

Winnie Wong-Ng, Ph.D.   Member, Supervisory Committee

Eric Jankowski, Ph.D.   Member, Supervisory Committee

David Estrada, Ph.D.   Member, Supervisory Committee

The final reading approval of the dissertation was granted by Lan Li, Ph.D. and Rick Ubic, Ph.D., Co-Chairs of the Supervisory Committee. The dissertation was approved by the Graduate College.

DEDICATION

This dissertation is dedicated to my wife and children. Delanie, you have been a constant companion for me throughout my entire career in higher education. Our love has inspired, encouraged, and supported me through every obstacle, test, setback, success, and achievement. Without you, I would not have come this far. You have shown exceptional strength and patience by taking care of our family whenever I travelled and through late nights, long weekends, and impending deadlines. Kyah and Tayson, I love you more than you will ever realize. Your joy and laughter keeps me smiling, your wonder keeps me motivated, your struggles keep me grounded, and your hearts keep me inspired. The world would be a brighter place if we could all love as you do.

ACKNOWLEDGEMENTS

Many factors have contributed to the progress and success I have experienced during my educational career. I am thankful to Boise State University, the Micron School of Materials Science and Engineering, and the Idaho National Laboratory (INL) for their facilities, programs, and computational resources. Also, I have had exceptional support from family, friends, teachers, professors, advisors, collaborators, and classmates. This dissertation would not have been possible without a great deal of help, so I am exceedingly grateful for all the encouragement, assistance, and advice.

First, I would like to acknowledge my advisor, Dr. Lan Li. She has been instrumental for the inception of this dissertation by providing the foundation for my quantum mechanics and DFT knowledge and introducing me to the topics presented in this work. With her assistance and support, I have garnered a number of travel, presentation, collaboration, and internship opportunities which have been crucial for my personal development and the development of this work. Dr. Li remains driven and dedicated to my success for which I will always be grateful.

Next, I would like to thank the members of my committee for their time, support, and suggestions over the past few years. Dr. Rick Ubic has been a large factor in my education, including contributions on: crystallography and microscopy courses, advising my undergraduate senior project, and working with him as editorial assistant for the *Materials Research Bulletin* (MRB). Dr. Winnie Wong-Ng at the National Institute of Standards and Technology (NIST) has collaborated with our group on numerous projects

ABSTRACT

This dissertation documents the computational modeling of skutterudite and two-dimensional transition metal dichalcogenide (2D TMD) materials for energy and electronic applications by analyzing the effects of materials doping and heterostructure formation on structural, energetic, electrical, phonon, and thermal properties. These topics remain largely unexplored and can accelerate materials development by providing insight on structure-properties-performance relationships.

Skutterudites are commonly studied for thermoelectric applications because they are low-cost, easy to process, and offer good intrinsic transport properties. They also exist as large, open structures which can be altered through filler atoms or substitutional dopants. A density functional theory (DFT)-based investigation of dopant effects on skutterudite compounds provided insight to advance the understanding of electrical and phonon properties that experiments could not measure. This also offered a good benchmark material for developing a modeling scheme that was employed for 2D TMD materials. 2D TMD nanosheets also exhibit large variability in structure type, dimensionality, and composition and have attracted much interest for their magnetic, electronic, optoelectronic, catalytic, and thermoelectric properties. Their low dimensionality makes them promising candidates for field-effect transistor (FET) device applications and introduces quantum confinement effects and diffusive boundary scattering, potentially improving their electrical and transport properties. The exploration

of composition, substitutional doping, and heterostructure effects is needed for further 2D TMD materials development and property improvement.

This dissertation offers an analysis of the structure-property relationships for a wide range of properties on bulk skutterudite and 2D TMD materials. The three key outcomes of this work are: (1) a high throughput approach to compute and analyze electrical and phonon properties, (2) a screening method for investigating 2D TMD materials and highlighting preferred compositions, and (3) design principles for predicting structures and properties to guide experiments. The optimized high throughput approach encompasses: DFT-based total energy minimization calculations to investigate the geometric, energetic, and electronic structure data; Boltzmann transport theory, in combination with electronic band energies, to estimate electrical conductivity (σ), Seebeck coefficient (S), and power factor ($S^2\sigma$) values; density functional perturbation theory (DFPT)-based second-order force constant calculations to determine phonon dispersion and density of states (DoS) spectra; and the atomistic Green's function (AGF) method, using force constants as input, to compute interfacial heat flux, phonon transmission coefficients, and thermal boundary conductance (TBC). Error mitigation was handled by optimizing model parameters and validating results through comparison with literature and experimental data. Through the optimized high throughput approach, dozens of 2D TMD structures can now be analyzed within days, whereas initial optimization calculations for each structure took up to one week to compute. Overall, these materials offer great potential for materials-by-design exploration and understanding their structural, electrical, and phonon properties are essential for advancement towards commercial applications.

TABLE OF CONTENTS

LIST OF TABLES

LIST OF FIGURES

LIST OF ABBREVIATIONS

2D	Two-dimensional
2D TMD	Two-dimensional transition metal dichalcogenide
3D	Three-dimensional
a	Lattice constant
Å	Angström
AGF	Atomistic Green's function
BoltzTraP	Boltzmann transport properties
CBM	Conduction band minimum
DFT	Density functional theory
DFT+U	Density functional theory with Hubbard U correction
DoS	Density of States
$d_{S\text{-}S}$	Vertical distance between S chalcogens in 2D MS_2's
E_{cut}	Cutoff energy
E_f	Formation energy
E_F	Fermi level
E_g	Electronic bandgap
EMD	Equilibrium molecular dynamics
eV	Electron volts
FET	Field-effect transistor
GKF	Green Kubo formula

GGA	Generalized gradient approximation
h-BN	Hexagonal boron nitride
J	On-site exchange potential
κ	Thermal conductivity
LDA	Local density approximation
PAW	Projector augmented wave
PBE	Perdew-Burke-Ernzerhof
σ	Electrical conductivity
S	Seebeck coefficient
$S^2\sigma$	Power factor
τ	Relaxation time
TBC	Thermal boundary conductance
TMD	Transition metal dichalcogenide
TMO	Transition metal dioxide
μV	Micro-volts
U	On-site Coulomb potential
VASP	Vienna *ab initio* simulation package
VBM	Valence band maximum
vdW	van der Waals
ZT	Thermoelectric figure of merit

CHAPTER ONE: INTRODUCTION

1.1 Research Goal and Motivation

To accelerate materials development, this dissertation aims to derive basic

materials design principles through high-throughput computational screening methods.

By generating large and rich data sets and analyzing the data to capture changes in trends

and relationships between structure, properties, and performance, we can optimize

materials' properties and performance by tailoring their structures.

This dissertation focuses on the area of electronic and energy applications and

how they can be directly improved through the implementation and successful

completion of this research goal. For the past fifty years, the semiconductor industry, for

example, has been striving to maintain growth in line with Moore's Law, which predicts

that the number of transistors present in an integrated circuit would double every two

years. The industry has managed to keep pace with this prediction through a number of

innovations in chip design, photolithography, and processing techniques. Smaller feature

sizes approach physical limitations as well as dimensionality constraints. Thus, it is

crucial to understand electrical transport behavior in this regime as quantum effects take

over.

With reduction in the size of device features comes an increase in energy density

within the chips. Joule heating, via the conversion of electrical power to thermal energy,

causes internal temperatures to exceed that of safe, operable conditions. This leads to

excessive wear, premature device failure, and safety hazards for people operating these

devices. The issue of understanding electrical and thermal properties is nontrivial and further work is needed to improve such devices.

This work investigates the key parameters that influence electrical and thermal properties. They include the analysis of electron and phonon density of states (DoS) spectra and the calculation of electrical conductivity, σ, and the Seebeck coefficient, S, which is a material's voltage response to a temperature gradient (useful for thermoelectric and thermocouple applications). Materials systems with potential applications in these fields include skutterudites and two-dimensional transition metal dichalcogenides (2D TMDs). These have good intrinsic electrical properties and tailorable structures, making them good candidates for energy and electronic applications, but more work is needed to further improve their properties. To achieve the research goal, the effects of two main structural changes have been investigated: (1) doping and (2) the formation of a heterojunction.

1.2 Objectives

This project has four research objectives.

Objective 1: Understand dopant and filler atom effects on skutterudite materials (Chapter Four) This includes the analysis of bulk $(Fe,Co)Sb_3$ skutterudites and how they are affected by Ca/Ce filler and Te/Ge substitutional dopants. This allows for the analysis of dopant effects on electrical and phonon properties in a three-dimensional material while also acting as a foundation for the development of the computational approach.

Objective 2: Computationally screen 2D TMD material compositions (Chapter Five) The physical features of six different constituent metals (Mo, Ni, Sc, Ti, V, and W) are

compared with respect to three different chalcogenide (S, Se, and Te) compounds while translating the previous computational approach to a lower dimensionality.

Objective 3: Understand the effects of substitutional dopants in 2D TMDs (Chapter Six) Each of the six transition metals from objective 2 are individually substituted into metal-sites within the 2D MoX_2 and WX_2 (X = S, Se, or Te) structures. Structural, electrical, and phonon properties are analyzed, focusing on the effect of substitution concentration and type.

Objective 4: Evaluate the impact of a lateral heterojunction between 2D TMDs (Chapter Seven) The effects of laterally joining 2D MoS_2 with 2D MS_2 (M = Cr, Sc, Ti, and W) to form a heterostructure are investigated. Structural, electrical, and phonon effects are compared.

1.3 Dissertation Summary

This dissertation includes the investigation of structural, electrical, and phonon properties of 3D skutterudite materials and 2D TMD nanosheets from first-principles. At the time this dissertation is being written, three peer-reviewed papers have been published from this work in the *Journal of Applied Physics*, *JOM*, and *Chemical Physics Letters* and another has been submitted to the *Journal of Applied Physics*. The chapters are arranged as follows. Chapter 2 gives a more in-depth explanation of the structure and current state of research for the skutterudite and 2D TMD materials systems while chapter 3 explains the methodology and theory behind the models employed in this work. Chapter 4 includes the investigation of Ca/Ce filler atoms in $FeSb_3$ and Te/Ge substitutional dopants on the Sb site in $CoSb_3$.[1] The work in chapter 5 screens a range of transition metals in 2D TMD materials comparing common oxidation states, atomic

masses, and atomic radii.[2] Chapter 6 investigates the effects of metal-site substitutional dopants in 2D MoS_2 and WS_2 sheets. The work presented in this chapter is divided into two subsections: dopant concentration[3] and dopant type.[4] Chapter 7 investigates the effect of heterostructure formation between 2D MoS_2 and MS_2 (M = Cr, Sc, Ti, W). Chapter 8 summarizes and concludes this dissertation.

References

(1)   Williamson, I.; Her, L. J. Y.; Su, X. L.; Yan, Y. G.; Wong-Ng, W.; Li, L. Improved thermoelectric performance of (Fe,Co)Sb-3-type skutterudites from first-principles. J Appl Phys 2016, 119, 055101.

(2)   Williamson, I.; Correa Hernandez, A.; Wong-Ng, W.; Li, L. High-Throughput Computational Screening of Electrical and Phonon Properties of Two-Dimensional Transition Metal Dichalcogenides. JOM 2016, 68, 2666.

(3)   Williamson, I.; Li, S.; Correa Hernandez, A.; Lawson, M.; Chen, Y.; Li, L. Structural, electrical, phonon, and optical properties of Ti- and V-doped two-dimensional MoS2. Chemical Physics Letters 2017, 674, 157.

(4)   Williamson, I.; Wilson, N.; Lawson, M.; Li, S.; Chen, Y.; Li, L. Computational Screening of Metal-Site Dopants in Two-Dimensional MX2 (M = Mo, W; X = S, Se, Te). J Appl Phys 2017, submitted.

CHAPTER TWO: MATERIALS SYSTEMS

The materials of interest in this dissertation are bulk skutterudites and two-dimensional transition metal dichalcogenides (2D TMDs). Both offer a variety of compositional options and tailorable structures and geometries which can significantly affect materials properties and performance, specifically in electronic and energy applications. High-throughput computational screening methods were employed to analyze the effects of doping (including filler atoms and substitutions) and heterostructures for the two materials that are of interest.

2.1 Skutterudites

Skutterudite compounds are low-cost and easy to process materials with intrinsically good electrical transport properties and tunable thermal transport properties.[1-10] The term "skutterudite" refers to minerals that have a cobalt arsenide, $CoAs_3$-type crystal structure. They form in space group $Im3$ and consist of cage-like structures with the general formula AB_3, where A is a transition metal and B is a pnictogen atom. Figure 2.1 shows the crystal structure of a filled skutterudite featuring M filler atoms and B rings in an A sublattice, where M = La, Te, Ge, Ba, In, or Yb; A = Fe, Ru, Co, Ni, or Os; and B = Sb, P, or As. Sb-based skutterudites are extensively studied due to their high mobility, atomic masses, electrical conductivity, and Seebeck coefficients.[11]
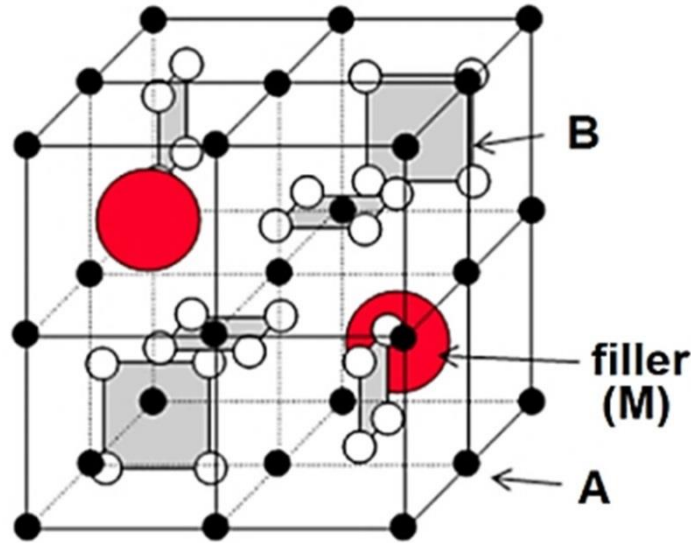
Figure 2.1. **Crystal structure of a filled M₂A₈B₂₄ skutterudite with filler atom M in red, B in white, and A in black. The gray substructures outlined by B atoms are referred to as pnictogen rings.**

Specifically, these novel characteristics make skutterudites of great interest for

thermoelectric applications. Thermoelectric devices can be used to recover waste heat by

converting it back into electrical power. This is known as the Seebeck effect. The

performance metric of thermoelectric materials is known as the thermoelectric figure of

merit,

$$ZT = \frac{S^2\sigma}{\kappa}T \qquad (2.1)$$

where S is the Seebeck coefficient, σ is the electrical conductivity, the combined $S^2\sigma$

term is referred to as the power factor, κ is the thermal conductivity, and T is the absolute

temperature. The implementation of thermoelectric devices has many promising

commercial applications including in-home power and heating, automobile energy

recovery, solar cells, and semiconductors. Unfortunately, it is difficult to obtain

thermoelectric figures of merit that exceed unity (*i.e.*, $ZT > 1$) in macroscale devices. In

order to improve these devices and bring them into large-scale use, there are a number of

issues left to resolve. A greater understanding of transport phenomena is needed to

overcome these obstacles. Skutterudite compounds generally have a *ZT* value around 1 and maintain large carrier concentrations and moderate Seebeck coefficients.[12,13] $CoSb_3$ is of particular interest because of its high power factor and moderately high temperature stability.[12] The most important task for improvement then comes from the reduction of thermal conductivity (without affecting carrier mobility).

<u>Current State of Skutterudite Materials Research</u>

The structure of a skutterudite has large degrees of freedom for doping and alloying, making them attractive for customization and design studies. A promising approach to improving skutterudite performance is therefore to modify their crystal structure by either filling structural voids with guest atoms or through substitutional dopants.[11,14] The introduction of filler atoms has been widely studied because they offer increased electrical conductivity with negligible effects on Seebeck coefficient and decreased thermal phonon conductivity through a "rattling effect."[15] Calculations performed by Feldman *et al.*,[16] and eventually experimental work by Koza *et al.*,[17] have since challenged the rattling effect. Nevertheless, filler atoms can modify the phonon dispersion and *ab initio* calculations have shown a reduction in thermal conductivity through an increase in anharmonic scattering rates and reduction of group velocities.[18] Alkaline earths have previously been used as fillers[2] and Yang *et al.*[19] have shown that a double-filled skutterudite, having one alkaline earth and one lanthanide (Ba and Ce) filler, is even more effective at reducing the lattice thermal conductivity than using two alkaline earths (Ba and Sr). Previous experimental work from our collaborators[20] used Ca and Ce fillers (which have a greater mass difference, 71%, than that of Ba and Ce, 2%) and found that for the double-filled $(Ca_xCe_{1-x})Fe_4Sb_{12}$ series (x = 0, 0.25, 0.5, 0.75, and

1), only the $x = 0.5$ compound was stable. They also measured this compound to have a higher *ZT* value than that of the end members due to its decreased thermal conductivity.

Alternatively, substitutional doping has been shown to improve skutterudite performance. Co site substitutions that have been investigated for the $CoSb_3$ structure include Cr,[21] Ni,[22] or Fe.[20] These substitutions reveal significant changes in transport properties such as an increase in electrical conductivity and a decrease in thermal conductivity; however, experimental and theoretical calculations have shown that substitution on the pnictogen rings (Sb site) is more effective for reducing thermal conductivity due to the rings' dominance of the phonon thermal conductivity spectrum.[16,23,24] Laser flash thermal diffusivity measurements on $CoSb_{3-x}Te_x$ compounds have shown a reduction in lattice thermal conductivity through atomic mass fluctuation and size strain.[25] This effect is increased through the incorporation of electric-charge compensating Ge and Sn substitution on the Sb site which disrupt the bonding and symmetry of the rings.[26]

Despite the amount of research conducted for this material system, there have not been major improvements in the thermoelectric figure of merit for skutterudites since the early 1990s. Therefore, a fundamental investigation of fillers and substitutions and their effects on the electrical and phonon properties of skutterudite compounds is important for materials development.

2.2 Two-Dimensional Transition Metal Dichalcogenides (2D TMDs)

The variability and interesting transport properties inherent in skutterudites makes them a great benchmark material for building a transport properties modeling scheme.

The approach can be translated to study similar phenomena in other materials. Here, we turned to a lower dimensionality and investigated 2D TMDs.

TMDs, having the chemical formula MX_2 (M = transition metal, X = chalcogen, *e.g.*, S, Se, Te), have received attention over the years for having interesting magnetic[27,28] and photoelectric[29] properties. Bulk three-dimensional transition metal dichalcogenides (3D TMDs) can exist as layered structures wherein each layer consists of a transition metal (M) sheet sandwiched between two chalcogen (X) sheets. These layers exist in one of two structure types: 2H-type having D_{6h} point group symmetry and 1T-type having D_{3d} point group symmetry (see Figure 2.2). Strong covalent bonding exists within the MX_2 layers (along the *a* and *b* axes) while much weaker van der Waals (vdW) interactions exist between the layers (along the *c* axis). This allows individual MX_2 layers to be separated via mechanical exfoliation.[30]
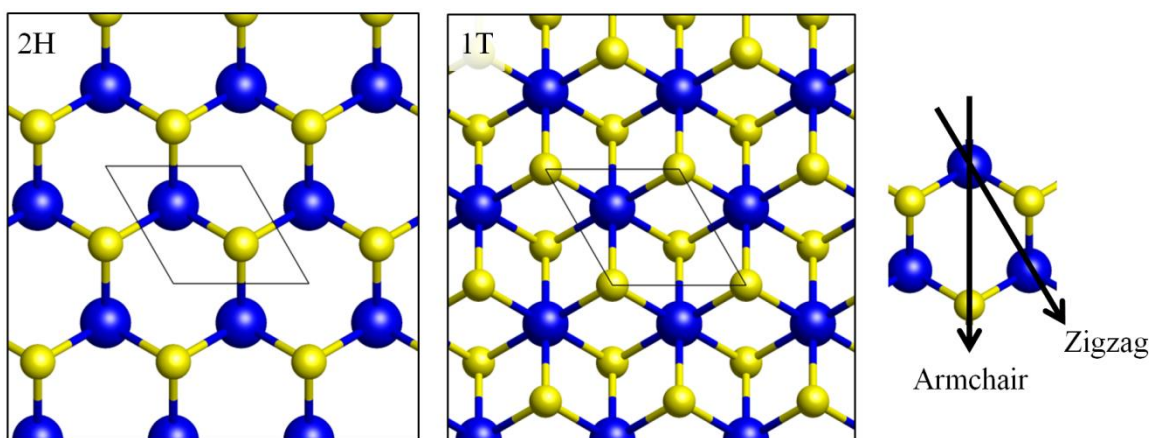
Figure 2.2. **Top-down view of 2D TMD sheets having 2H- or 1T-type structures. Cyan and yellow spheres represent M and X atoms, respectively. Thin black lines frame the unit cell. Armchair and zigzag directions are depicted with bold black arrows.**

The separated 2D TMD materials have recently attracted much interest for a variety of applications including electronics,[31-35] optoelectronics,[36-39] catalysts,[40,41] and thermoelectrics.[42-45] In addition, the quantum confinement effect and sharp features in the electronic density of states (DoS) are beneficial for improving thermoelectric properties, such as increasing the Seebeck coefficient, S, in 2D TMDs compared to that of the bulk structures.[46-48] It is also predicted that the lower dimensionality increases diffusive boundary scattering, effectively reducing the thermal conductivity, κ. Lowering the dimensionality of Si, for example, has shown strong reductions in κ and implications for enhanced thermoelectric performance.[49,50] With a large number of potential 2D TMD compounds, it is important to identify key structure–property–performance relationships in order to screen preferred materials.

2D TMD materials are of particular interest for applications in electronic devices. With their wide compositional variety comes a variety of electronic structures including metals and direct or indirect bandgap semiconductors. The lower dimensionality further expands the range of properties beyond that of the bulk TMD materials. For example, bulk MoS_2 has an indirect bandgap of 1.2 eV while 2D MoS_2 has a direct bandgap of 1.8 eV.[51,52] Reduced dimensionality also offers the potential for smaller device features and has been shown to greatly reduce short-channel effects, increase the on–off ratio, and reduce switching voltage in field-effect transistors (FETs).[33,36] With these characteristics, 2D TMDs could potentially substitute for Si in electronic devices.[53-55] Each of these factors contributes to the strong motivation for further understanding the behavior of 2D TMDs.

Current State of TMD Materials Research

TMD studies focus on the stability and electronic structure of 2D TMDs and TMOs (transition metal dioxides) using density functional theory (DFT).[31,32] These offer a general analysis of trends across a broad range of compositions and identify most structures to be semiconducting with small indirect bandgaps. Rasmussen *et al.*[32] found that only CrX_2, MoX_2, and WX_2 systems exhibit direct bandgaps. From these works, it is useful to identify more favorable 2D TMD compositions in terms of stability, electrical properties, and optical properties; however, none have been directed at what compositions are possible. Graedel *et al.*[56] developed a method for quantifying the environmental implications, supply risk, and vulnerability to supply restrictions for 62 transition metals and metalloids. These "criticality scores" can be used to identify preferred materials and narrow the focus for screening potential compositions in order to develop high-performance, cost-effective, and environmentally friendly materials. Along with reduced dimensionality and identification of novel compositions and structures, strategies for further improvement of 2D TMD properties and performance include doping and heterostructure formation.[57,58]

Metal-site substitutional dopants yield interesting changes in the intrinsic properties of 2D TMDs. These dopants can cause enhancements such as inducing magnetism[59-62] and tuning of the electrical conductivity.[62] They also offer the ability to modify the bandgap and photoluminescence[63] and control whether it is a *p*- or *n*-type semiconductor.[64] Experimental work has shown that these dopants are stable in 2D TMDs and that they are a substitutional dopant rather than an interstitial impurity.[65-68]

This type of defect tends to be more stable because the dopant inherits the strong covalent bonds within the TMD sheet.

The formation of lateral heterostructures is another promising approach for improving optical and electrical properties.[57] Lateral epitaxy has been used to synthesize high quality heterostructures with type II (staggered) band alignment which has potential for optoelectronic applications.[69,70] Raman spectroscopy techniques have been used to analyze both the physical and phonon structures of heterostructures.[71] Experimental work reveals that 2D TMDs prefer to form heterostructures along the "zigzag" direction of the honeycomb structure (see Figure 2.2).[72] First-principles calculations have found interesting electronic structure effects of these zigzag junctions. For example, the bandgap of the lateral MoS_2-WS_2 heterostructure has been calculated to be about 1.58 eV, smaller than that of MoS_2 and WS_2.[73] Band offset calculations confirm type II band alignment between MoX_2-WX_2 heterostructures and reveal an increase in both the conduction band minimum (CBM) and valence band maximum (VBM) with increasing M and X atomic numbers.[74]

A thorough investigation into the structural, electrical, and phonon properties of 2D TMDs is crucial for the development of these materials. This can be achieved by identifying novel compositions and understanding the effects of substitutional dopants and heterostructures.

2.3 Computational Modeling Approaches

The choice of computational modeling technique can be based on a number of factors including: length scale, what variables are needed/relevant (*e.g.*, time, temperature), and the governing physics of the properties in question. For example, an

investigation of bonding characteristics requires the use of quantum mechanics and a very small length scale (nanometer) whereas thermal energy propagation in a nuclear reactor core may be on the order of meters and involve a continuum modeling approach. For this dissertation, the scope is narrowed to smaller length scales and methods that can be used to investigate electrical and phonon properties.

Equilibrium molecular dynamics (EMD) is one approach that can be used to calculate transport coefficients via the Green-Kubo formula (GKF).[75,76] This is a widely studied approach due to its ability to yield accurate thermal properties of large materials;[77-79] however, it does not account for electrical properties and is not well suited for 2D materials. For investigating the nanoscale regime, the use of density functional theory (DFT) is preferred because it incorporates electron density.

In this dissertation, the quantum mechanics-based method of DFT was employed to investigate these materials. Within DFT, there are a number of options for calculating transport properties of a material. Traditionally, DFT has been shown to underestimate bandgaps[80] so many approaches have been proposed for improving band structure calculations. Among the more rigorous calculations include the use of hybrid functionals[81-84] which incorporate some exact exchange into the exchange correlation interaction term and the GW approximation[85] which involves the expansion of self-energies with respect to the single-particle Green's function, G, and the screened Coulomb interaction, W. These calculations have the advantage of generating more accurate band structures without relying on empirical data; however, they greatly increase computational costs and are not easily suited for screening purposes. The semi-empirical method of DFT+U,[86] which adds a Hubbard-like on-site Coulomb potential term to

account for strongly correlated electronic states, can be quickly and easily implemented to correct the overestimation and produce good quality band structures with negligible computational costs.

The calculation of thermal conductivity from first-principles is made possible through the full linearization of the Boltzmann transport equation for phonons.[87] This is a very rigorous approach and involves the calculation of third-order force constants to account for phonon anharmonicity within the material. The computational costs are too high for screening purposes and it is not yet fully implemented for 2D materials; however, second-order force constant calculations can account for normal processes with only moderate computational costs. The use of density functional perturbation theory (DFPT)[88] allows for the calculation of necessary force constants and can produce phonon dispersion and density of states (DoS). This does not allow for the calculation of thermal conductivity but can provide useful phonon property information for materials screening.

This dissertation employs the use of DFT to screen structural, bonding, electrical, and phonon properties of 3D skutterudite and 2D TMD materials focusing on the effects of doping and heterostructures. The problem of understanding electrical and thermal transport in these materials is one of multiscale and multiphysics. There remains a lack of general knowledge that must be addressed through the use of large-scale materials screening processes before more-rigorous calculations can be utilized. More information about the methods used in this work can be found in Chapter 3.

References

(1)   Tan, G. J.; Wang, S. Y.; Li, H.; Yan, Y. G.; Tang, X. F. Enhanced thermoelectric performance in zinc substituted p-type filled skutterudites CeFe4-xZnxSb12. *Journal of Solid State Chemistry* **2012**, *187*, 316.

(2)   Dyck, J. S.; Chen, W. D.; Uher, C.; Chen, L.; Tang, X. F.; Hirai, T. Thermoelectric properties of the n-type filled skutterudite Ba0.3Co4Sb12 doped with Ni. *J Appl Phys* **2002**, *91*, 3698.

(3)   Wong-Ng, W.; Kaduk, J. A.; Tan, G.; Yan, Y.; Tang, X. X-ray powder reference patterns of the Fe(Sb2+xTe1-x) skutterudites for thermoelectric applications. *Powder Diffraction* **2014**, *29*, 260.

(4)   Tan, G. J.; Liu, W.; Chi, H.; Su, X. L.; Wang, S. Y.; Yan, Y. G.; Tang, X. F.; Wong-Ng, W.; Uher, C. Realization of high thermoelectric performance in p-type unfilled ternary skutterudites FeSb2+xTe1-x via band structure modification and significant point defect scattering. *Acta Materialia* **2013**, *61*, 7693.

(5)   Yan, Y. G.; Wong-Ng, W.; Kaduk, J. A.; Tan, G. J.; Xie, W. J.; Tang, X. F. Correlation of thermoelectric and microstructural properties of p-type CeFe4Sb12 melt-spun ribbons using a rapid screening method. *Appl Phys Lett* **2011**, *98*.

(6)   He, T.; Chen, J. Z.; Rosenfeld, H. D.; Subramanian, M. A. Thermoelectric properties of indium-filled skutterudites. *Chem Mater* **2006**, *18*, 759.

(7)   Huang, B.; Kaviany, M. Filler-reduced phonon conductivity of thermoelectric skutterudites: Ab initio calculations and molecular dynamics simulations. *Acta Materialia* **2010**, *58*, 4516.

(8)   Hara, R.; Inoue, S.; Kaibe, H. T.; Sano, S. Aging effects of large-size n-type CoSb3 prepared by spark plasma sintering. *Journal of Alloys and Compounds* **2003**, *349*, 297.

(9)   Kim, H.; Kaviany, M.; Thomas, J. C.; Van der Ven, A.; Uher, C.; Huang, B. L. Structural Order-Disorder Transitions and Phonon Conductivity of Partially Filled Skutterudites. *Phys Rev Lett* **2010**, *105*, 265901.

(10)   Luo, P. F.; Tang, X. F.; Xiong, C.; Zhang, Q. J. Effect of multiwalled carbon nanotubes on the thermoelectric properties of p-type Ba0.3FeCo3Sb12 compounds. *Acta Phys Sin-Ch Ed* **2005**, *54*, 2403.

(11)   Rull-Bravo, M.; Moure, A.; Fernandez, J. F.; Martin-Gonzalez, M. Skutterudites as thermoelectric materials: revisited. *Rsc Adv* **2015**, *5*, 41653.

(12)   Morelli, D. T.; Caillat, T.; Fleurial, J. P.; Borshchevsky, A.; Vandersande, J.; Chen, B.; Uher, C. Low-Temperature Transport-Properties of P-Type Cosb3. *Phys Rev B* **1995**, *51*, 9622.

(13)   Caillat, T.; Borshchevsky, A.; Fleurial, J. P. Properties of single crystalline semiconducting CoSb3. *J Appl Phys* **1996**, *80*, 4442.

(14)   Sootsman, J. R.; Chung, D. Y.; Kanatzidis, M. G. New and Old Concepts in Thermoelectric Materials. *Angew Chem Int Edit* **2009**, *48*, 8616.

(15)   Slack, G. A.; Tsoukala, V. G. Some Properties of Semiconducting Irsb3. *J Appl Phys* **1994**, *76*, 1665.

(16)   Feldman, J. L.; Singh, D. J. Lattice dynamics of skutterudites: First-principles and model calculations for CoSb3. *Phys Rev B* **1996**, *53*, 6273.

(17)   Koza, M. M.; Johnson, M. R.; Viennois, R.; Mutka, H.; Girard, L.; Ravot, D. Breakdown of phonon glass paradigm in La- and Ce-filled Fe(4)Sb(12) skutterudites. *Nature Materials* **2008**, *7*, 805.

(18)   Li, W.; Mingo, N. Thermal conductivity of fully filled skutterudites: Role of the filler. *Phys Rev B* **2014**, *89*, 184304.

(19)   Yang, J.; Zhang, W.; Bai, S. Q.; Mei, Z.; Chen, L. D. Dual-frequency resonant phonon scattering in BaxRyCo4Sb12 (R=La, Ce, and Sr). *Appl Phys Lett* **2007**, *90*, 192111.

(20)   Yan, Y. G.; Wong-Ng, W.; Li, L.; Levin, I.; Kaduk, J. A.; Suchomel, M. R.; Sun, X.; Tan, G. J.; Tang, X. F. Structures and thermoelectric properties of double-filled (CaxCe1-x)Fe4Sb12 skutterudites. *Journal of Solid State Chemistry* **2014**, *218*.

(21)   Yang, J.; Endres, M. G.; Meisner, G. P. Valence of Cr in skutterudites: Electrical transport and magnetic properties of Cr-doped CoSb3. *Phys Rev B* **2002**, *66*.

(22)   Yang, J.; Morelli, D. T.; Meisner, G. P.; Chen, W.; Dyck, J. S.; Uher, C. Influence of electron-phonon interaction on the lattice thermal conductivity of Co1-xNixSb3. *Phys Rev B* **2002**, *65*.

(23)   Dimitrov, I. K.; Manley, M. E.; Shapiro, S. M.; Yang, J.; Zhang, W.; Chen, L. D.; Jie, Q.; Ehlers, G.; Podlesnyak, A.; Camacho, J.; Li, Q. A. Einstein modes in the phonon density of states of the single-filled skutterudite Yb0.2Co4Sb12. *Phys Rev B* **2010**, *82*, 174301.

(24)   Chi, H.; Kim, H.; Thomas, J. C.; Su, X. L.; Stackhouse, S.; Kaviany, M.; Van der Ven, A.; Tang, X. F.; Uher, C. Configuring pnicogen rings in skutterudites for low phonon conductivity. *Phys Rev B* **2012**, *86*, 195209.

(25)   Liu, W. S.; Zhang, B. P.; Zhao, L. D.; Li, J. F. Improvement of Thermoelectric Performance of CoSb3-xTex Skutterudite Compounds by Additional Substitution of IVB-Group Elements for Sb. *Chem Mater* **2008**, *20*, 7526.

(26)   Su, X. L.; Li, H.; Wang, G. Y.; Chi, H.; Zhou, X. Y.; Tang, X. F.; Zhang, Q. J.; Uher, C. Structure and Transport Properties of Double-Doped CoSb2.75Ge0.25-xTex (x=0.125-0.20) with in Situ Nanostructure. *Chem Mater* **2011**, *23*, 2948.

(27)   Ogawa, S. Magnetic-Properties of 3d Transition-Metal Dichalcogenides with the Pyrite Structure. *J Appl Phys* **1979**, *50*, 2308.

(28)   Shishidou, T.; Freeman, A. J.; Asahi, R. Effect of GGA on the half-metallicity of the itinerant ferromagnet CoS2. *Phys Rev B* **2001**, *64*, 180401.

(29)   Tributsch, H. Solar Energy-Assisted Electrochemical Splitting of Water. *Z Naturforsch A* **1977**, *32*, 972.

(30)   Coleman, J. N.; Lotya, M.; O'Neill, A.; Bergin, S. D.; King, P. J.; Khan, U.; Young, K.; Gaucher, A.; De, S.; Smith, R. J.; Shvets, I. V.; Arora, S. K.; Stanton, G.; Kim, H. Y.; Lee, K.; Kim, G. T.; Duesberg, G. S.; Hallam, T.; Boland, J. J.; Wang, J. J.; Donegan, J. F.; Grunlan, J. C.; Moriarty, G.; Shmeliov, A.; Nicholls, R. J.; Perkins, J. M.; Grieveson, E. M.; Theuwissen, K.; McComb, D. W.; Nellist, P. D.; Nicolosi, V. Two-Dimensional Nanosheets Produced by Liquid Exfoliation of Layered Materials. *Science* **2011**, *331*, 568.

(31)   Ataca, C.; Sahin, H.; Ciraci, S. Stable, Single-Layer MX2 Transition-Metal Oxides and Dichalcogenides in a Honeycomb-Like Structure. *Journal of Physical Chemistry C* **2012**, *116*, 8983.

(32)   Rasmussen, F. A.; Thygesen, K. S. Computational 2D Materials Database: Electronic Structure of Transition-Metal Dichalcogenides and Oxides. *Journal of Physical Chemistry C* **2015**, *119*, 13169.

(33)   Butler, S. Z.; Hollen, S. M.; Cao, L. Y.; Cui, Y.; Gupta, J. A.; Gutierrez, H. R.; Heinz, T. F.; Hong, S. S.; Huang, J. X.; Ismach, A. F.; Johnston-Halperin, E.; Kuno, M.; Plashnitsa, V. V.; Robinson, R. D.; Ruoff, R. S.; Salahuddin, S.; Shan, J.; Shi, L.; Spencer, M. G.; Terrones, M.; Windl, W.; Goldberger, J. E. Progress, Challenges, and Opportunities in Two-Dimensional Materials Beyond Graphene. *Acs Nano* **2013**, *7*, 2898.

(34)   McDonnell, S.; Addou, R.; Buie, C.; Wallace, R. M.; Hinkle, C. L. Defect-Dominated Doping and Contact Resistance in MoS2. *Acs Nano* **2014**, *8*, 2880.

(35)   Gong, C.; Colombo, L.; Wallace, R. M.; Cho, K. The Unusual Mechanism of Partial Fermi Level Pinning at Metal-MoS2 Interfaces. *Nano Lett* **2014**, *14*, 1714.

(36)   Ganatra, R.; Zhang, Q. Few-Layer MoS2: A Promising Layered Semiconductor. *Acs Nano* **2014**, *8*, 4074.

(37)   Radisavljevic, B.; Radenovic, A.; Brivio, J.; Giacometti, V.; Kis, A. Single-layer MoS2 transistors. *Nat Nanotechnol* **2011**, *6*, 147.

(38)   Lopez-Sanchez, O.; Lembke, D.; Kayci, M.; Radenovic, A.; Kis, A. Ultrasensitive photodetectors based on monolayer MoS2. *Nat Nanotechnol* **2013**, *8*, 497.

(39)   Baugher, B. W. H.; Churchill, H. O. H.; Yang, Y. F.; Jarillo-Herrero, P. Optoelectronic devices based on electrically tunable p-n diodes in a monolayer dichalcogenide. *Nat Nanotechnol* **2014**, *9*, 262.

(40)   Chen, W.; Santos, E. J. G.; Zhu, W. G.; Kaxiras, E.; Zhang, Z. Y. Tuning the Electronic and Chemical Properties of Monolayer MoS2 Adsorbed on Transition Metal Substrates. *Nano Lett* **2013**, *13*, 509.

(41)   Jaramillo, T. F.; Jorgensen, K. P.; Bonde, J.; Nielsen, J. H.; Horch, S.; Chorkendorff, I. Identification of active edge sites for electrochemical H-2 evolution from MoS2 nanocatalysts. *Science* **2007**, *317*, 100.

(42)   Huang, W.; Da, H. X.; Liang, G. C. Thermoelectric performance of MX2 (M = Mo, W; X = S, Se) monolayers. *J Appl Phys* **2013**, *113*, 104304.

(43)   Huang, W.; Luo, X.; Gan, C. K.; Quek, S. Y.; Liang, G. C. Theoretical study of thermoelectric properties of few-layer MoS2 and WSe2. *Physical Chemistry Chemical Physics* **2014**, *16*, 10866.

(44)   Lee, C.; Hong, J.; Whangbo, M. H.; Shim, J. H. Enhancing the Thermoelectric Properties of Layered Transition-Metal Dichalcogenides 2H-MQ(2) (M = Mo, W; Q = S, Se, Te) by Layer Mixing: Density Functional Investigation. *Chem Mater* **2013**, *25*, 3745.

(45)   Gu, X. K.; Yang, R. G. Phonon transport in single-layer transition metal dichalcogenides: A first-principles study. *Appl Phys Lett* **2014**, *105*, 131903.

(46)   Hicks, L. D.; Dresselhaus, M. S. Effect of Quantum-Well Structures on the Thermoelectric Figure of Merit. *Phys Rev B* **1993**, *47*, 12727.

(47)   Hicks, L. D.; Dresselhaus, M. S. Thermoelectric Figure of Merit of a One-Dimensional Conductor. *Phys Rev B* **1993**, *47*, 16631.

(48)   Mahan, G. D.; Sofo, J. O. The best thermoelectric. *P Natl Acad Sci USA* **1996**, *93*, 7436.

(49)   Hochbaum, A. I.; Chen, R. K.; Delgado, R. D.; Liang, W. J.; Garnett, E. C.; Najarian, M.; Majumdar, A.; Yang, P. D. Enhanced thermoelectric performance of rough silicon nanowires. *Nature* **2008**, *451*, 163.

(50)   Boukai, A. I.; Bunimovich, Y.; Tahir-Kheli, J.; Yu, J. K.; Goddard, W. A.; Heath, J. R. Silicon nanowires as efficient thermoelectric materials. *Nature* **2008**, *451*, 168.

(51)   Kam, K. K.; Parkinson, B. A. Detailed Photocurrent Spectroscopy of the Semiconducting Group-Vi Transition-Metal Dichalcogenides. *J Phys Chem-Us* **1982**, *86*, 463.

(52)   Mak, K. F.; Lee, C.; Hone, J.; Shan, J.; Heinz, T. F. Atomically Thin MoS2: A New Direct-Gap Semiconductor. *Phys Rev Lett* **2010**, *105*, 136805.

(53)   Roy, K.; Padmanabhan, M.; Goswami, S.; Sai, T. P.; Ramalingam, G.; Raghavan, S.; Ghosh, A. Graphene-MoS2 hybrid structures for multifunctional photoresponsive memory devices. *Nat Nanotechnol* **2013**, *8*, 826.

(54)   Schmidt, H.; Wang, S. F.; Chu, L. Q.; Toh, M.; Kumar, R.; Zhao, W. J.; Neto, A. H. C.; Martin, J.; Adam, S.; Ozyilmaz, B.; Eda, G. Transport Properties of Monolayer MoS2 Grown by Chemical Vapor Deposition. *Nano Lett* **2014**, *14*, 1909.

(55)   Yu, L. L.; Lee, Y. H.; Ling, X.; Santos, E. J. G.; Shin, Y. C.; Lin, Y. X.; Dubey, M.; Kaxiras, E.; Kong, J.; Wang, H.; Palacios, T. Graphene/MoS2 Hybrid Technology for Large-Scale Two-Dimensional Electronics. *Nano Lett* **2014**, *14*, 3055.

(56)   Graedel, T. E.; Harper, E. M.; Nassar, N. T.; Nuss, P.; Reck, B. K. Criticality of metals and metalloids. *P Natl Acad Sci USA* **2015**, *112*, 4257.

(57)   Wang, H. T.; Yuan, H. T.; Hong, S. S.; Li, Y. B.; Cui, Y. Physical and chemical tuning of two-dimensional transition metal dichalcogenides. *Chem Soc Rev* **2015**, *44*, 2664.

(58)   Liu, G. B.; Xiao, D.; Yao, Y. G.; Xu, X. D.; Yao, W. Electronic structures and theoretical modelling of two-dimensional group-VIB transition metal dichalcogenides. *Chem Soc Rev* **2015**, *44*, 2643.

(59)   Zhou, Y. G.; Su, Q. L.; Wang, Z. G.; Deng, H. Q.; Zu, X. T. Controlling magnetism of MoS2 sheets by embedding transition-metal atoms and applying strain. *Physical Chemistry Chemical Physics* **2013**, *15*, 18464.

(60)   Cheng, Y. C.; Zhu, Z. Y.; Mi, W. B.; Guo, Z. B.; Schwingenschlogl, U. Prediction of two-dimensional diluted magnetic semiconductors: Doped monolayer MoS2 systems. *Phys Rev B* **2013**, *87*, 100401.

(61)   Ramasubramaniam, A.; Naveh, D. Mn-doped monolayer MoS2: An atomically thin dilute magnetic semiconductor. *Phys Rev B* **2013**, *87*, 195201.

(62)   Saab, M.; Raybaud, P. Tuning the Magnetic Properties of MoS2 Single Nanolayers by 3d Metals Edge Doping. *Journal of Physical Chemistry C* **2016**, *120*, 10691.

(63)   Chen, Y. F.; Xi, J. Y.; Dumcenco, D. O.; Liu, Z.; Suenaga, K.; Wang, D.; Shuai, Z. G.; Huang, Y. S.; Xie, L. M. Tunable Band Gap Photoluminescence from Atomically Thin Transition-Metal Dichalcogenide Alloys. *Acs Nano* **2013**, *7*, 4610.

(64)   Suh, J.; Park, T. E.; Lin, D. Y.; Fu, D. Y.; Park, J.; Jung, H. J.; Chen, Y. B.; Ko, C.; Jang, C.; Sun, Y. H.; Sinclair, R.; Chang, J.; Tongay, S.; Wu, J. Q. Doping against the Native Propensity of MoS2: Degenerate Hole Doping by Cation Substitution. *Nano Lett* **2014**, *14*, 6976.

(65)   Hsu, W. K.; Zhu, Y. Q.; Yao, N.; Firth, S.; Clark, R. J. H.; Kroto, H. W.; Walton, D. R. M. Titanium-doped molybdenum disulfide nanostructures. *Advanced Functional Materials* **2001**, *11*, 69.

(66)   Deepak, F. L.; Cohen, H.; Cohen, S.; Feldman, Y.; Popovitz-Biro, R.; Azulay, D.; Millo, O.; Tenne, R. Fullerene-like (IF) NbxMo1-xS2 nanoparticles. *J Am Chem Soc* **2007**, *129*, 12549.

(67)   Sun, Q. C.; Yadgarov, L.; Rosentsveig, R.; Seifert, G.; Tenne, R.; Musfeldt, J. L. Observation of a Burstein-Moss Shift in Rhenium-Doped MoS2 Nanoparticles. *Acs Nano* **2013**, *7*, 3506.

(68)   Yadgarov, L.; Rosentsveig, R.; Leitus, G.; Albu-Yaron, A.; Moshkovich, A.; Perfilyev, V.; Vasic, R.; Frenkel, A. I.; Enyashin, A. N.; Seifert, G.; Rapoport, L.; Tenne, R. Controlled Doping of MS2 (M=W, Mo) Nanotubes and Fullerene-like Nanoparticles. *Angew Chem Int Edit* **2012**, *51*, 1148.

(69)   Huang, C. M.; Wu, S. F.; Sanchez, A. M.; Peters, J. J. P.; Beanland, R.; Ross, J. S.; Rivera, P.; Yao, W.; Cobden, D. H.; Xu, X. D. Lateral heterojunctions within monolayer MoSe2-WSe2 semiconductors. *Nature Materials* **2014**, *13*, 1096.

(70)   Chen, K.; Wan, X.; Wen, J. X.; Xie, W. G.; Kang, Z. W.; Zeng, X. L.; Chen, H. J.; Xu, J. B. Electronic Properties of MoS2-WS2 Heterostructures Synthesized with Two-Step Lateral Epitaxial Strategy. *Acs Nano* **2015**, *9*, 9868.

(71)   Zhang, X.; Qiao, X. F.; Shi, W.; Wu, J. B.; Jiang, D. S.; Tan, P. H. Phonon and Raman scattering of two-dimensional transition metal dichalcogenides from monolayer, multilayer to bulk material. *Chem Soc Rev* **2015**, *44*, 2757.

(72)   Zhang, X. Q.; Lin, C. H.; Tseng, Y. W.; Huang, K. H.; Lee, Y. H. Synthesis of Lateral Heterostructures of Semiconducting Atomic Layers. *Nano Lett* **2015**, *15*, 410.

(73)   Wang, Q. W.; Wu, P.; Cao, G. Y.; Huang, M. First-principles study of the structural and electronic properties of MoS2-WS2 and MoS2-MoTe2 monolayer heterostructures. *J Phys D Appl Phys* **2013**, *46*, 505308.

(74)   Kang, J.; Tongay, S.; Zhou, J.; Li, J. B.; Wu, J. Q. Band offsets and heterostructures of two-dimensional semiconductors. *Appl Phys Lett* **2013**, *102*, 012111.

(75)   Green, M. S. Markoff Random Processes and the Statistical Mechanics of Time-Dependent Phenomena .2. Irreversible Processes in Fluids. *Journal of Chemical Physics* **1954**, *22*, 398.

(76)   Kubo, R. Statistical-Mechanical Theory of Irreversible Processes .1. General Theory and Simple Applications to Magnetic and Conduction Problems. *J Phys Soc Jpn* **1957**, *12*, 570.

(77)   Che, J. W.; Cagin, T.; Deng, W. Q.; Goddard, W. A. Thermal conductivity of diamond and related materials from molecular dynamics simulations. *Journal of Chemical Physics* **2000**, *113*, 6888.

(78)   Volz, S. G.; Chen, G. Molecular-dynamics simulation of thermal conductivity of silicon crystals. *Phys Rev B* **2000**, *61*, 2651.

(79)   Yao, Z. H.; Wang, J. S.; Li, B. W.; Liu, G. R. Thermal conduction of carbon nanotubes using molecular dynamics. *Phys Rev B* **2005**, *71*, 085417.

(80)   Perdew, J. P. Density Functional Theory and the Band-Gap Problem. *Int J Quantum Chem* **1985**, 497.

(81)   Becke, A. D. A New Mixing of Hartree-Fock and Local Density-Functional Theories. *Journal of Chemical Physics* **1993**, *98*, 1372.

(82)   Perdew, J. P.; Emzerhof, M.; Burke, K. Rationale for mixing exact exchange with density functional approximations. *Journal of Chemical Physics* **1996**, *105*, 9982.

(83)   Adamo, C.; Barone, V. Toward reliable density functional methods without adjustable parameters: The PBE0 model. *Journal of Chemical Physics* **1999**, *110*, 6158.

(84)   Heyd, J.; Scuseria, G. E.; Ernzerhof, M. Hybrid functionals based on a screened Coulomb potential. *Journal of Chemical Physics* **2003**, *118*, 8207.

(85)   Aryasetiawan, F.; Gunnarsson, O. The GW method. *Rep Prog Phys* **1998**, *61*, 237.

(86)   Liechtenstein, A. I.; Anisimov, V. I.; Zaanen, J. Density-functional theory and strong interactions: Orbital ordering in Mott-Hubbard insulators. *Phys Rev B* **1995**, *52*, R5467.

(87)   Li, W.; Carrete, J.; Katcho, N. A.; Mingo, N. ShengBTE: A solver of the Boltzmann transport equation for phonons. *Computer Physics Communications* **2014**, *185*, 1747.

(88)   Parlinski, K.; Li, Z. Q.; Kawazoe, Y. First-principles determination of the soft mode in cubic ZrO2. *Phys Rev Lett* **1997**, *78*, 4063.

CHAPTER THREE: MODELING ELECTRICAL AND THERMAL PROPERTIES IN
THE SOLID STATE

The field of computational materials modeling is a fast growing area that offers a
means of prediction and understanding beyond that of conventional research. By applying
numerical models to emulate physical phenomena, we can analyze more wholly the
relationships between structure, properties, and performance. Through the utilization of
high-performance computing facilities, rigorous and complex calculations can be
conducted on numerous materials systems faster than experiments. This work
demonstrates how density functional theory (DFT), in conjunction with Boltzmann
transport theory and density functional perturbation theory (DFPT), can be implemented
to analyze structures, energetics, electrical, and thermal transport properties of
skutterudite and two dimensional transition metal dichalcogenides (2D TMDs).

The flowchart in Figure 3.1 is an overview of different computational methods
used in this dissertation. All structure, energetic, electronic, and force calculations
performed in this work begin with DFT and the total energy minimization calculation.
After optimizing the appropriate DFT parameters (see the Approximations subsection in
3.1 Density Functional Theory (DFT)), the energetic and structural ground state can be
determined. Section 3.2 Electrical Transport Properties explains how the band energies
can then be expanded to calculate semi-classic transport coefficients such as S, σ, and κ_e.
Next, section 3.3 Thermal Transport Properties explains how the second-order force
constants calculated with DFPT can be used to determine phonon dispersion and DoS

spectra. Finally, the incorporation of the recently developed atomistic Green's function (AGF) method, along with the second-order force constants, can be used to calculate transmission coefficients across a 2D TMD heterojunction as well as thermal boundary conductance.
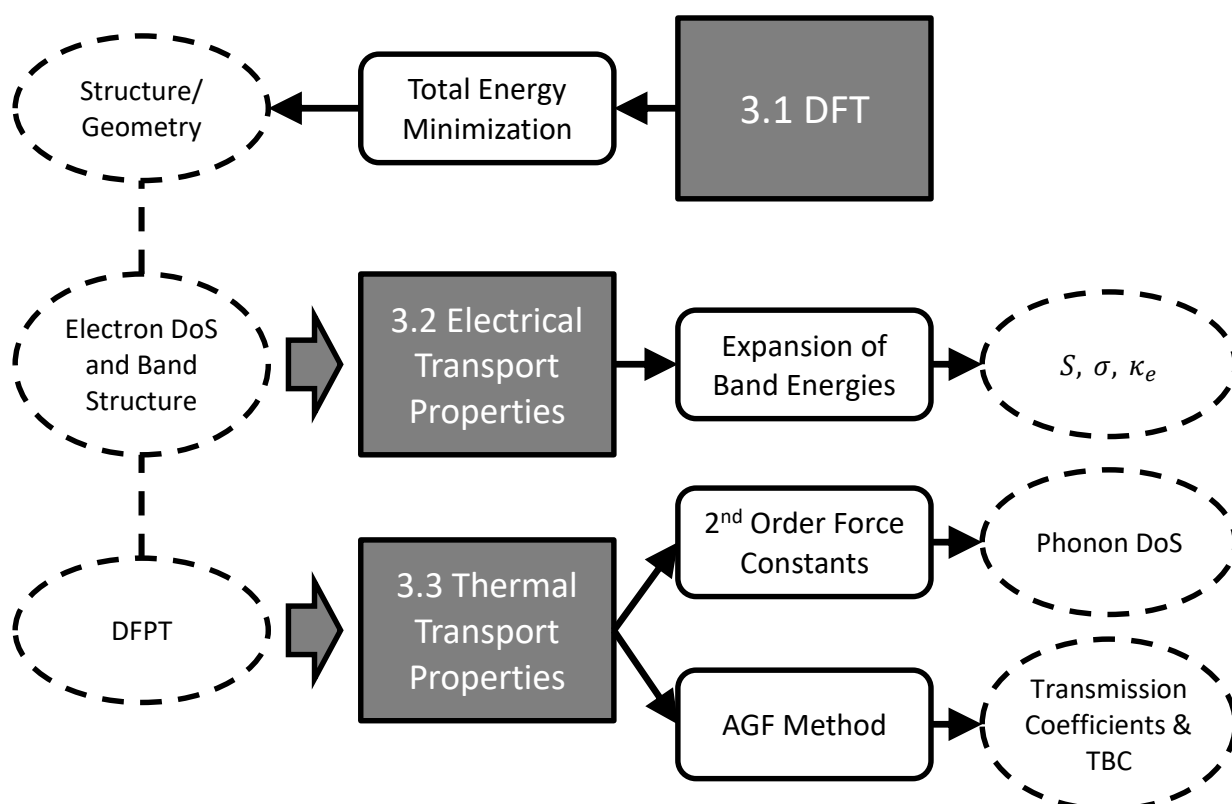
Figure 3.1.   Flowchart describing the computational approach used to calculate electrical and thermal transport properties in this dissertation. DFT is used to minimize the total energy of the system in order to determine the electronic ground state. This can then be used to calculate structural features, band energies, and DFPT force constants. The band energies can be expanded to calculate electrical transport coefficients such as *S*, σ, and κ_e. The second-order force constants can be used to calculate phonon DoS or combined with the AGF method to determine phonon transmission coefficients across a heterojunction.

3.1 Density Functional Theory (DFT)

The many-body problem describes the fact that wavefunctions needed to define a system having more than two electrons (up to infinity) range from extremely difficult to impossible to solve due to extensive particle interaction. DFT is an approach to handling

the many-body problem by approximating the energy of a system by means of the charge

density which is a function of the electronic wavefunctions. Despite a number of

approximations, DFT can reasonably estimate the geometry and structure of various

materials.

This approach revolves primarily around solving the Kohn-Sham (KS) equation,

which is an adaptation of the Schrödinger equation for non-interacting particles.

$$\hat{H}_{KS}\Psi(\boldsymbol{r}) = E(\boldsymbol{r})\Psi(\boldsymbol{r}) \tag{3.1}$$

The symbol Ψ is the electron wavefunction, E is the total energy of the system, and $\hat{H}_{KS}$

is the KS Hamiltonian operator defined by,

$$\hat{H}_{KS} = E_{kin}^{non} + U_{ext} + U_H + U_{xc} \tag{3.2}$$

Here, the energy terms are broken down into E_{kin}^{non},– the kinetic energy of the non-

interacting electron $(-\frac{1}{2}\nabla^2)$, U_{ext} – the external potential felt by the electron from the

nuclei, U_H – the Hartree potential which assumes the electrons are independent and

interact in an averaged way (alternatively known as the mean-field approximation), and

U_{xc} – the exchange correlation which approximates all interaction terms. This eigenvalue

problem is solved self-consistently where a trial charge density is used to calculate a total

energy for the system to compare with the starting value. The method is repeated until the

energy is consistent within a given range. By calculating interatomic forces and

iteratively translating atoms to minimize those forces, the ground state geometry can be

determined.[1]

<u>Approximations</u>

There are four primary approximations considered in this dissertation that directly

affect the calculations: supercell, exchange-correlation, pseudopotential theory, and the

self-consistent field (scf) approach. To minimize error in the calculations and validate the

models, each approximation was investigated via convergence tests. In general, this is

done by running calculations with various parameters and comparing results (*e.g.*, lattice

constants, bond lengths, cell volume, and electronic bandgaps). Each approximation

affects different aspects of the calculation so each is addressed differently.

The use of Bloch's theorem in DFT treats materials systems as periodic and

repeating. The supercell approximation is used to handle aperiodic configurations such as

dopants and surfaces. 2D systems in this dissertation are treated as single- or few-layer

atomic sheets separated by large (>20 Å) vacuum layers. The choice of vacuum thickness

came from convergence tests which showed negligible interaction between repeating

sheets with this thickness.

Electron-electron interactions remain one of the most difficult aspects of DFT

needed to accurately describe a system. Exchange-correlation is a term added to the $\hat{H}_{KS}$

operator that accounts for all electron interaction terms. The simplest approach to

calculating this is through the local density approximation (LDA)[2] which assumes the

exchange-correlation energy per electron at a given point is equal to the exchange-

correlation energy for a homogeneous electron gas of the same density. Alternately, the

generalized gradient approximation (GGA) accounts for semi-local information by

adding an additional term to account for the rate of change in exchange-correlation

energy at a given point. This is known to produce slightly more accurate structures than

LDA and is generally better suited for more materials systems.[1] There are many different

forms of GGA, but the method of Perdew, Burke, and Ernzerhof (PBE)[3] – which is

commonly used for its simplicity, accuracy, and independence from empirical input –

was chosen for this dissertation. Convergence tests confirmed that it is useful for determining skutterudite and 2D TMD structures.

The pseudopotential theory involves replacing the strong potential between electrons and ions with a much weaker *pseudopotential*, which are designed to maintain the features of the valence electrons while "freezing" and simplifying the core electrons. A graphical representation of the pseudopotential and pseudo wave function can be seen in Figure 3.2. A commonly used approach for generating pseudopotentials that is both efficient and accurate is called the projector-augmented wave (PAW) method,[4,5] which uses a radial grid projection from the atom center to map the core wave functions while mapping the valence wave functions with the plane-wave expansion.[1] The set of plane-waves used in DFT is determined through the optimization of a "cutoff energy" (E_{cut}) which incorporates all valence electrons with kinetic energies at or below E_{cut}. Electrons with kinetic energies greater than E_{cut} are assumed to be associated with the core and are therefore not considered. Convergence tests are used to determine this value. The PAW pseudopotential approach was determined to be the most accurate and useful method for this dissertation work.
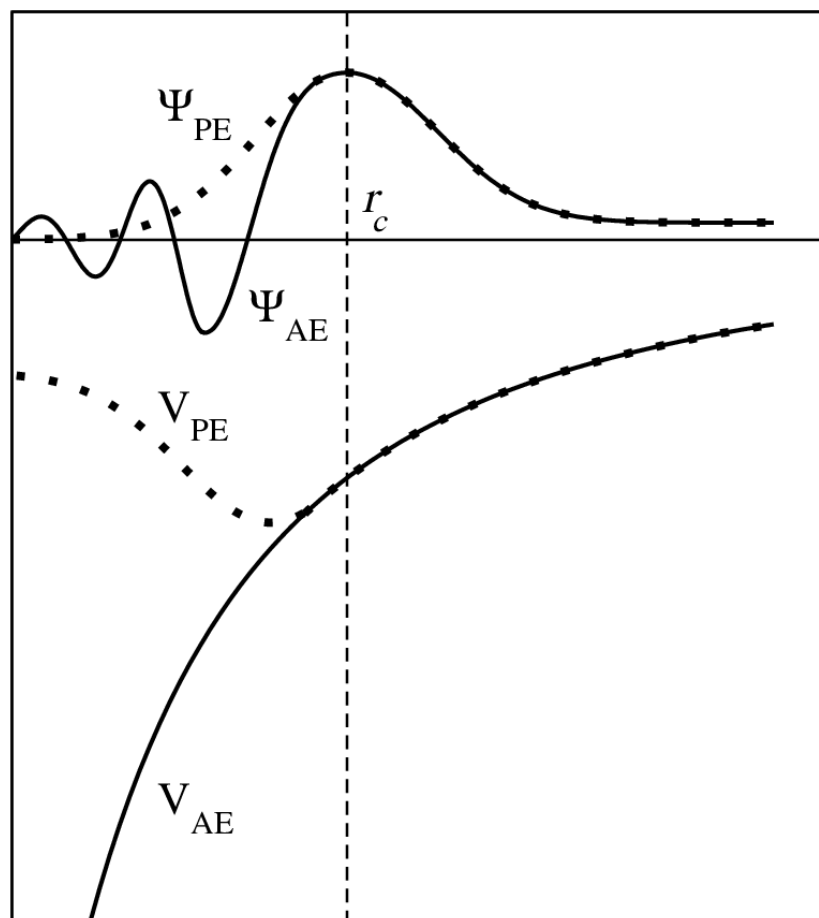
Figure 3.2. Schematic demonstrating the pseudo-electron (PE) (dotted lines) and all-electron (AE) (solid lines) wave function, Ψ, and potential, V. The PE and AE values must match at $r \geq r_c$ where r_c represents the core radius.

The scf approach describes the method used to solve the KS equation and determine the final ground state energy. The approach, outlined in Figure 3.3, begins with rough estimates for the KS wave functions (taken from the pseudopotentials of each element) and uses them to calculate electron densities, which are used to calculate $\hat{H}_{KS}$; and $\hat{H}_{KS}$ is then used to generate new electron densities. This method is iterated until the input and output orbitals converge and "self-consistency" is reached. There are a number of parameters that govern the scf calculation. These include matrix diagonalization schemes, charge density mixing, and energy convergence thresholds. Once the first scf step is completed, the forces are calculated and atomic positions are updated to minimize

the total energy of the system. Then, new scf steps are performed and the cycle is repeated until a predetermined force convergence threshold is reached and the effective ground state is determined (*i.e.*, the structure is "relaxed"). Convergence tests were conducted to determine necessary parameters involved for relaxing these structures.
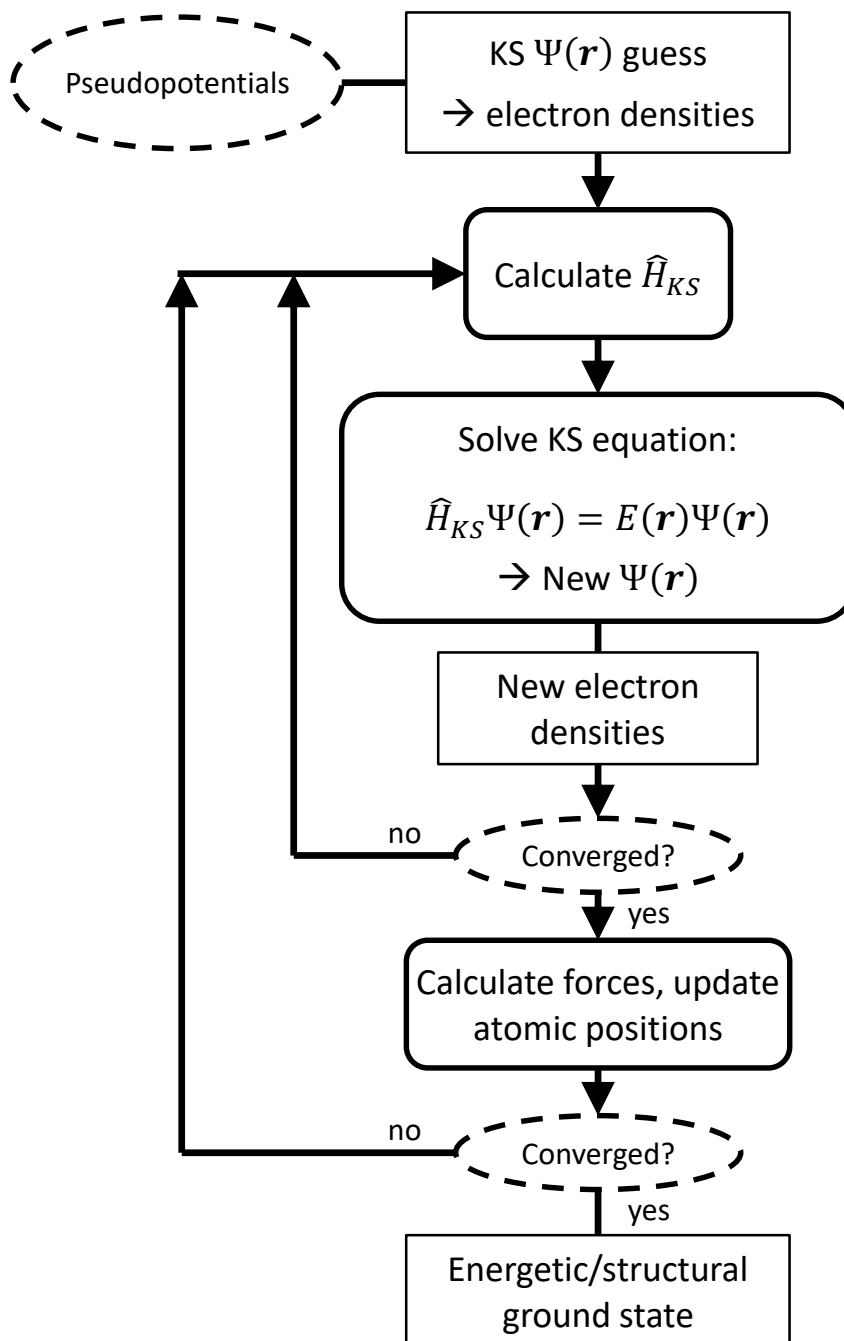
Figure 3.3. Flowchart describing the scf and structural relaxation method performed during a DFT calculation. A single scf step is completed when the first "convergence" step is reached. By calculating the forces after an scf step and adjusting the atomic positions, the forces can be minimized until a "relaxed" ground state configuration is determined.

3.2 Electrical Transport Properties

After the ground state is determined for a given system, the electronic density of states (DoS) and energy band diagrams can be calculated; however, a known shortcoming of DFT is its tendency to underestimate and even eliminate bandgaps. This effect is especially present with strong localized d- and f-orbitals. A method for correcting this involves the use of DFT+U which adds an on-site Coulomb potential term (U) and an on-site exchange term (J).[6] Though typically obtained semi-empirically, the application of these terms can greatly improve the accuracy of electronic structure calculations without increasing computational costs. As described in Figure 3.1, the optimized band energies can be used as input to Boltzmann transport property calculations.[7]

Expansion of Band Energies

The ground-state band energies of a material contain much information about various material properties. Madsen demonstrated that transport properties such as S, σ, and the Hall coefficient (R_H) can be calculated from the band energies.[7] Through the use of star functions, the band energies can be expanded in Fourier space according to

$$\tilde{\varepsilon}_i(\boldsymbol{k}) = \sum_{\boldsymbol{R}} c_{\boldsymbol{R},i} S_{\boldsymbol{R}}(\boldsymbol{k}) \tag{3.3}$$

$$S_{\boldsymbol{R}}(\boldsymbol{k}) = \frac{1}{n} \sum_{\{\Lambda\}} e^{i\boldsymbol{k}\cdot\Lambda\mathbf{R}} \tag{3.4}$$

where $\mathbf{R}$ is the direct lattice vector and $\{\Lambda\}$ are the n point group rotations.

The group velocity, v_α, and inverse mass tensor, $M_{\beta u}^{-1}$, can be calculated from the first and second derivative of the band energies, respectively:

$$v_\alpha(i, \mathbf{k}) = \frac{1}{\hbar} \frac{\partial \varepsilon_{i,\mathbf{k}}}{\partial k_\alpha} \tag{3.5}$$

$$M_{\beta u}^{-1}(i, \mathbf{k}) = \frac{1}{\hbar^2} \frac{\partial^2 \varepsilon_{i,\mathbf{k}}}{\partial k_\beta \partial k_u} \tag{3.6}$$

Here, $\hbar$ represents the reduced Planck's constant while the symbol $\varepsilon_{i,\mathbf{k}}$ represents the

energy of band i at a given $\mathbf{k}$-point. Then the conductivity tensors can be found using

$$\sigma_{\alpha\beta}(i, \mathbf{k}) = e^2 \tau_{i,\mathbf{k}} v_\alpha(i, \mathbf{k}) v_\beta(i, \mathbf{k}) \tag{3.7}$$

$$\sigma_{\alpha\beta\gamma}(i, \mathbf{k}) = e^3 \tau_{i,\mathbf{k}}^2 \epsilon_{\gamma u v} v_\alpha(i, \mathbf{k}) v_v(i, \mathbf{k}) M_{\beta u}^{-1} \tag{3.8}$$

where the latter tensor is written with respect to the Levi-Civita symbol, $\epsilon_{\gamma u v}$.[8,9] These

can be expressed as a function of band energy, ε

$$\sigma_{\alpha\beta}(\varepsilon) = \frac{1}{N} \sum_{i,\mathbf{k}} \sigma_{\alpha\beta}(i, \mathbf{k}) \frac{\delta(\varepsilon - \varepsilon_{i,\mathbf{k}})}{d\varepsilon} \tag{3.9}$$

$$\sigma_{\alpha\beta\gamma}(\varepsilon) = \frac{1}{N} \sum_{i,\mathbf{k}} \sigma_{\alpha\beta\gamma}(i, \mathbf{k}) \frac{\delta(\varepsilon - \varepsilon_{i,\mathbf{k}})}{d\varepsilon} \tag{3.10}$$

with N number of $\mathbf{k}$-points. The resulting transport tensors can be calculated as functions

of temperature and chemical potential

$$\nu_{\alpha\beta}(T; \mu) = \frac{1}{eT\Omega} \int \sigma_{\alpha\beta}(\varepsilon)(\varepsilon - \mu) \left[-\frac{\partial f_u(T;\varepsilon)}{\partial \varepsilon} \right] d\varepsilon \tag{3.11}$$

$$\sigma_{\alpha\beta}(T; \mu) = \frac{1}{\Omega} \int \sigma_{\alpha\beta}(\varepsilon) \left[-\frac{\partial f_u(T;\varepsilon)}{\partial \varepsilon} \right] d\varepsilon \tag{3.12}$$

$$\sigma_{\alpha\beta\gamma}(T; \mu) = \frac{1}{\Omega} \int \sigma_{\alpha\beta\gamma}(\varepsilon) \left[-\frac{\partial f_u(T;\varepsilon)}{\partial \varepsilon} \right] d\varepsilon \tag{3.13}$$

along with the Seebeck coefficient

$$S_{ij} = E_i (\nabla_j T)^{-1} = (\sigma^{-1})_{\alpha i} \nu_{\alpha j} \tag{3.14}$$

The electron relaxation time, $\tau_{i,\mathbf{k}}$, is an important metric for calculating the

transport properties as it describes the average time between scattering events. In

practice, this is a non-trivial variable to calculate. The total relaxation time, τ_t, can be found using Matthiesen's rule

$$\frac{1}{\tau_t} = \sum_j \frac{1}{\tau_j} \tag{3.15}$$

where τ_j represents individual relaxation times from each different scattering mechanism.[10] Rather than calculating this for each band and $\textbf{\textit{k}}$ direction, we will use a constant relaxation time in this work. This approximation is favorable because the relaxation time has been shown to be relatively independent of direction, even in strongly anisotropic systems.[11,12]

The electronic contribution to the thermal conductivity, κ_e, can also be written in terms of the conductivity distribution

$$\kappa_{e,\alpha\beta}(T;\mu) = \frac{1}{e^2 T \Omega} \int \sigma_{\alpha\beta}(\varepsilon)(\varepsilon - \mu)^2 \left[-\frac{\partial f_u(T;\varepsilon)}{\partial \varepsilon} \right] d\varepsilon \tag{3.16}$$

This term dominates the thermal conductivity for metals but is less impactful in semiconductors and insulators. For nonmetals, the thermal conductivity is dominated instead by the lattice thermal conductivity, κ_l, where

$$\kappa = \kappa_e + \kappa_l \tag{3.17}$$

To calculate κ_l, the phonon properties of the material must be investigated.

3.3 Thermal Transport Properties

In order to estimate the thermal transport properties of a material, it is necessary to analyze the phonon behavior. In general, the thermal conductivity is given in Equation 3.17 where κ_l is the contribution from the lattice waves (phonons). For semiconductors, this term is expected to dominate as the contribution from electrons, κ_e, would be negligible. There are a few different methods for modeling phonon behavior; however, the phenomenon of heat conduction is a problem of multiphysics and multilength scales.

Nevertheless, if one is drawing a comparison between similar systems, it is reasonable to identify trends via first-principles phonon property calculations. In this regard, DFT is often used as a calculator to estimate second- and third-order interatomic force constant matrices. These matrices are then used as input for phonon calculations which can be used to calculate phonon dispersion and DoS data (see Figure 3.1). Though third-order force constants are needed to account for Umklapp phonon scattering processes and determine κ_l, the second-order force constants can provide useful information about the phonon properties with only a fraction of the computational cost. For the screening purposes of this dissertation, only the second-order force constants are calculated to compare phonon property effects of dopants and heterostructures.

<u>Second-Order Force Constants</u>

This work employs the method of DFPT to calculate the second-order force constants of a system. In this approach, an external perturbation is used to displace the atoms in order to determine the Hessian matrix. By defining the potential, V, of the phonon system as a function of atomic positions, the force, F, and second-order force constant, $\Phi_{\alpha\beta}$, are given as

$$F_\alpha(jl) = -\frac{\partial V}{\partial r_\alpha(jl)} \tag{3.18}$$

$$\Phi_{\alpha\beta}(jl, j'l') = \frac{\partial^2 V}{\partial r_\alpha(jl) \partial r_\beta(j'l')} = -\frac{\partial F_\beta(j'l')}{\partial r_\alpha(jl)} \tag{3.19}$$

where the indices α and β are Cartesian, j and j' represent atoms in a unit cell, and l and l' represent the unit cell.[13]

Through the implementation of the Phonopy software package,[14] the force constants can be determined following the method of Parlinski, Li, and Kawazoe.[15] In this approach, Equation 3.19 is given as the matrices,

$$\mathbf{F} = -\mathbf{UP} \tag{3.20}$$

$$\mathbf{F} = \begin{pmatrix} F_x \\ F_y \\ F_z \end{pmatrix} \tag{3.21}$$

$$\mathbf{P} = \begin{pmatrix} \Phi_{xx} \\ \Phi_{xy} \\ \Phi_{xz} \\ \Phi_{yx} \\ \Phi_{yy} \\ \Phi_{yz} \\ \Phi_{zx} \\ \Phi_{zy} \\ \Phi_{zz} \end{pmatrix} \tag{3.22}$$

$$\mathbf{U} = \begin{pmatrix} \Delta r_x & 0 & 0 & \Delta r_y & 0 & 0 & \Delta r_z & 0 & 0 \\ 0 & \Delta r_x & 0 & 0 & \Delta r_y & 0 & 0 & \Delta r_z & 0 \\ 0 & 0 & \Delta r_x & 0 & 0 & \Delta r_y & 0 & 0 & \Delta r_z \end{pmatrix} \tag{3.23}$$

where the **U** matrix represents atomic displacements. Through the use of **A** (9x9 site-point symmetry matrices) terms, the system can be solved by pseudo inverse via the following equation

$$\begin{pmatrix} \mathbf{F}_1^{(1)} \\ \mathbf{F}_1^{(2)} \\ \vdots \\ \mathbf{F}_2^{(1)} \\ \mathbf{F}_2^{(2)} \\ \vdots \end{pmatrix} = - \begin{pmatrix} \mathbf{U}_1\mathbf{A}^{(1)} \\ \vdots \\ \mathbf{U}_1\mathbf{A}^{(2)} \\ \mathbf{U}_2\mathbf{A}^{(1)} \\ \mathbf{U}_2\mathbf{A}^{(2)} \\ \vdots \end{pmatrix} \mathbf{P} \tag{3.24}$$

where the superscript numbers indicate the index of site-symmetry operations.[13]

Atomistic Green's Function (AGF) Method

Thermal transport across a boundary, such as the boundary between two 2D TMDs in a lateral heterostructure, is limited by the Kapitza, or thermal resistance of the interface,[16] which determines the ratio of the boundary temperature difference to the interfacial heat flux. A higher thermal resistance corresponds to a greater temperature

difference at the interface for a given heat flux and can be useful for thermal insulation. This phenomenon has also received attention for potential thermoelectric applications.[17-20]

In semiconductors and insulators, the interfacial heat flux consists of phonons which are transmitted at the interface in a manner analogous to conventional acoustic and optical wave transmission. The probability of each phonon propagating across the interface, given by its transmission coefficient, depends on the phonon dispersion of the constituent materials and the atomistic structure of the interface and varies between 0 and 1 because of impedance to its transmission from the abrupt change in crystallographic structure at the interface. The interfacial heat flux, Q, in the *x*-direction can be intuitively expressed as the sum of the total phonon population weighted by their transmission coefficients as well as their frequencies and group velocities in the direction of the flux, *i.e.*, in a two-dimensional material,

$$Q = \frac{1}{4\pi^2 d} \int_{BZ} d^2k \sum_{n=1}^{9} \hbar \omega_n(k_x, k_y) N(\omega_n, T) t_n(k_x, k_y) v_n(k_x, k_y) \tag{3.25}$$

where the reciprocal (k_x, k_y) space integral is taken over the entire Brillouin zone, and d, $\hbar$, T, and n are the film thickness, reduced Planck constant, temperature, and phonon branch index, respectively. The variables ω_n, N, t_n, and v_n represent the phonon frequency, Bose-Einstein distribution function, transmission coefficient, and phonon group velocity in the direction of the flux, respectively. The expression in Equation 3.25 can be simplified to obtain the expression

$$Q(T) = \frac{1}{4\pi^2 d} \int_0^\infty d\omega \hbar \omega N(\omega, T) \int_{-\pi/a}^{+\pi/a} dk_y \Xi(k_y, \omega) \tag{3.26}$$

where $\Xi(k_y, \omega)$ is the Fourier (k_y) component of the overall transmission function given by

$$\Theta(\omega) = \frac{1}{2\pi} \int_{-\pi/a}^{+\pi/a} dk_y \Xi(k_y, \omega). \tag{3.27}$$

It is necessary to decompose the overall transmission function into its Fourier components because they can be computed piece-wise in a more computationally efficient fashion, especially if the interface has translational symmetry.

Although it is a straightforward exercise to calculate the phonon frequencies and group velocities, the computation of the transmission function $\Xi(k_y, \omega)$ is decidedly more involved and requires the application of a more sophisticated numerical technique such as the atomistic Green's function (AGF) method.[21] The AGF method, developed from the nonequilibrium Green's function (NEGF) theory for electrons, describes the lattice dynamics of a finite body, corresponding to the interface region and couple to two semi-infinite thermal reservoirs commonly referred to as *leads*, and determines how an incoming phonon propagates across the interface region from one lead to the other. Conceptually, the leads define the available bulk phonon channels while the lattice structure of the interface region determines the transition between each pair of channels (in-coming and out-going).

The AGF for the interface region $G_C(k_y, \omega)$ can be written as

$$G_C(k_y, \omega) = \lim_{\eta \to 0} \left[\omega^2 + i\eta - H_C(k_y) - \Sigma_L(k_y) - \Sigma_R(k_y) \right]^{-1} \tag{3.28}$$

where $H_C(k_y)$, $\Sigma_L(k_y)$, and $\Sigma_R(k_y)$ are the mass-normalized force constant, left-lead self-energy, and right-lead self-energy matrices for the Fourier component k_y, respectively. The self-energy matrix for the left lead is given by

$$\Sigma_L(k_y) = H_{CL} g_L(\omega) H_{CL}^\dagger \tag{3.29}$$

where H_{CL} is the mass-normalized force constant matrix representing the interaction between the left lead and the interface region, and $g_L(\omega)$ is the uncoupled surface Green's function for the left lead. The self-energy matrix for the right lead is similarly defined. The transmission function, $\Xi(k_y, \omega)$, which determines the total transmission for the given ω and k_y is given by

$$\Xi(k_y, \omega) = \text{trace}[\Gamma_L(k_y)G_C(k_y, \omega)\Gamma_R(k_y)G_C(k_y, \omega)^\dagger]. \qquad (3.30)$$

In Equations 3.28 and 3.29, the force constant matrices are calculated with DFT. A separate set of force-constant matrices is calculated for each lead and also for the interface region. At each frequency, the *total* transmission function in Equation 3.27 can be combined with the Landauer formula[22,23] to yield the heat current and thermal conductance of the interface.

Additional information on the distribution of the transmitted phonons can be obtained through the use of mode-matching[24,25] combined with the AGF method to extract the transmission coefficients of individual phonon modes and identify the constituent phonon modes in the interfacial heat flux.[26] This approach has already been used to analyze the lateral heterostructure of single-atomic layer graphene – hexagonal boron nitride (*h*-BN).[26,27] This dissertation similarly uses this newly developed approach to investigate the phonon transmission across the 2D MoS_2-WS_2 heterostructure interface and to obtain insights into the microscopic physical processes underlying heat transfer at the interface.

References

(1)   Lee, J. G. *Computational Materials Science*; CRC Press Taylor and Francis Group: Boca Raton, FL, 2012.

(2)   Kohn, W.; Sham, L. J. Self-Consistent Equations Including Exchange and Correlation Effects. *Phys Rev* **1965**, *140*, 1133.

(3)   Perdew, J. P.; Burke, K.; Ernzerhof, M. Generalized gradient approximation made simple. *Phys Rev Lett* **1996**, *77*, 3865.

(4)   Blöchl, P. E. Projector augmented-wave method. *Phys Rev B* **1994**, *50*, 17953.

(5)   Kresse, G.; Joubert, D. From ultrasoft pseudopotentials to the projector augmented-wave method. *Phys Rev B* **1999**, *59*, 1758.

(6)   Liechtenstein, A. I.; Anisimov, V. I.; Zaanen, J. Density-functional theory and strong interactions: Orbital ordering in Mott-Hubbard insulators. *Phys Rev B* **1995**, *52*, R5467.

(7)   Madsen, G. K. H.; Singh, D. J. BoltzTraP. A code for calculating band-structure dependent quantities. *Computer Physics Communications* **2006**, *175*, 67.

(8)   Hurd, C. M. *The Hall Effect in Metals and Alloys*; Plenum Press: New York, 1972.

(9)   Arfken, G. B.; Weber, H. J. *Mathematical Methods for Physicists*; Sixth ed.; Elsevier Academic Press: San Diego, 2005.

(10)   Chen, G. *Nanoscale Energy Transport and Conversion*; Oxford University Press: New York, 2005.

(11)   Schulz, W. W.; Allen, P. B.; Trivedi, N. Hall-Coefficient of Cubic Metals. *Phys Rev B* **1992**, *45*, 10886.

(12)   Allen, P. B.; Pickett, W. E.; Krakauer, H. Anisotropic Normal-State Transport-Properties Predicted and Analyzed for High-Tc Oxide Superconductors. *Phys Rev B* **1988**, *37*, 7482.

(13)   Togo, A.; Release 1.6.2 ed. https://atztogo.github.io/phonopy/, 2012.

(14)   Togo, A.; Tanaka, I. First principles phonon calculations in materials science. *Scripta Mater* **2015**, *108*, 1.

(15)   Parlinski, K.; Li, Z. Q.; Kawazoe, Y. First-principles determination of the soft mode in cubic ZrO2. *Phys Rev Lett* **1997**, *78*, 4063.

(16)   Swartz, E. T.; Pohl, R. O. Thermal-Boundary Resistance. *Reviews of Modern Physics* **1989**, *61*, 605.

(17)   Cahill, D. G.; Ford, W. K.; Goodson, K. E.; Mahan, G. D.; Majumdar, A.; Maris, H. J.; Merlin, R.; Sr, P. Nanoscale thermal transport. *J Appl Phys* **2003**, *93*, 793.

(18)   Pop, E. Energy Dissipation and Transport in Nanoscale Devices. *Nano Res* **2010**, *3*, 147.

(19)   Chen, P. X.; Katcho, N. A.; Feser, J. P.; Li, W.; Glaser, M.; Schmidt, O. G.; Cahill, D. G.; Mingo, N.; Rastelli, A. Role of Surface-Segregation-Driven Intermixing on the Thermal Transport through Planar Si/Ge Superlattices. *Phys Rev Lett* **2013**, *111*, 115901.

(20)   Cahill, D. G.; Braun, P. V.; Chen, G.; Clarke, D. R.; Fan, S. H.; Goodson, K. E.; Keblinski, P.; King, W. P.; Mahan, G. D.; Majumdar, A.; Maris, H. J.; Phillpot, S. R.; Pop, E.; Shi, L. Nanoscale thermal transport. II. 2003-2012. *Appl Phys Rev* **2014**, *1*.

(21)   Mingo, N.; Yang, L. Phonon transport in nanowires coated with an amorphous material: An atomistic Green's function approach. *Phys Rev B* **2003**, *68*, 245406.

(22)   Zhang, W.; Fisher, T. S.; Mingo, N. The atomistic Green's function method: An efficient simulation approach for nanoscale phonon transport. *Numer Heat Tr B-Fund* **2007**, *51*, 333.

(23)   Landauer, R. Conductance Determined by Transmission - Probes and Quantized Constriction Resistance. *J Phys-Condens Mat* **1989**, *1*, 8099.

(24)   Khomyakov, P. A.; Brocks, G.; Karpan, V.; Zwierzycki, M.; Kelly, P. J. Conductance calculations for quantum wires and interfaces: Mode matching and Green's functions. *Phys Rev B* **2005**, *72*, 035450.

(25)   Wang, J. S.; Wang, J.; Lu, J. T. Quantum thermal transport in nanostructures. *Eur Phys J B* **2008**, *62*, 381.

(26)   Ong, Z. Y.; Zhang, G. Efficient approach for modeling phonon transmission probability in nanoscale interfacial thermal transport. *Phys Rev B* **2015**, *91*, 174302.

(27)   Ong, Z. Y.; Zhang, G.; Zhang, Y. W. Controlling the thermal conductance of graphene/h-BN lateral interface with strain and structure engineering. *Phys Rev B* **2016**, *93*, 075406.

CHAPTER FOUR: IMPROVED THERMOELECTRIC PERFORMANCE OF

(Fe,Co)Sb3-TYPE SKUTTERUDITES FROM FIRST-PRINCIPLES*

This chapter is published by AIP Publishing in the *Journal of Applied Physics* and should

be referenced appropriately.

Reference:

I. Williamson, L. J.-Y. Her, X. Su, Y. Yan, W. Wong-Ng, L. Li, "Improved

thermoelectric performance of (Fe,Co)Sb$_3$-type skutterudites from first-principles."

Journal of Applied Physics. **119** 055101 (2016).

Reproduced from *Journal of Applied Physics*, **119** 055101 (2016), with the permission of

AIP Publishing.

*This chapter includes modifications from the originally published version.

Improved thermoelectric performance of (Fe,Co)Sb₃-type skutterudites from first-principles

Izaak Williamson[a]

Logan Ju-Yee Her[b]

Xianli Su[c]

Yonggao Yan[c]

Winnie Wong-Ng[d]

Lan Li[a,e]

[a]*Department of Materials Science and Engineering, Boise State University,*

Boise, ID 83725.

[b]*Department of Science, Math, and Engineering, Cosumnes River College,*

Sacramento, CA 95823.

[c]*State Key Laboratory of Advanced Technology for Materials Synthesis and Processing,*

Wuhan University of Technology,

Wuhan, Hubei 430070, China.

^dMaterials Measurement Science Division, National Institute of Standards and

Technology,

Gaithersburg, MD 20899.

^eCenter for Advanced Energy Studies,

Idaho Falls, ID 83401.

Abstract

Skutterudite materials have been considered as promising thermoelectric candidates due to intrinsically good electrical conductivity and tailorable thermal conductivity. Options for improving thermal-to-electrical conversion efficiency include identifying novel materials, adding filler atoms, and substitutional dopants. Incorporating filler or substitutional dopant atoms in the skutterudite compounds can enhance phonon scattering, resulting in reduction of thermal conductivity, as well as improving electrical conductivity. The structures, electronic properties, and thermal properties of double-filled $Ca_{0.5}Ce_{0.5}Fe_4Sb_{12}$ and $Co_4Sb_{12-2x}Te_xGe_x$ compounds ($x = 0$, 0.5, 1, 2, 3, and 6) have been studied using density functional theory (DFT) based calculations. Both Ca/Ce filler atoms in $FeSb_3$ and Te/Ge substitution in $CoSb_3$ cause a decrease in lattice constant for the compounds. As Te/Ge substitution concentration increases, lattice constant decreases and structural distortion of pnictogen rings in the compounds occurs. This indicates a break in cubic symmetry of the structure. The presence of fillers and substitutions causes an increase in electrical conductivity and a decrease in electronic bandgap. A transition from direct to indirect band-gap semiconducting behavior is found at $x = 3$. Phonon density of states for both compounds indicate phonon band broadening by the incorporation of fillers and substitutional atoms. The acoustic phonon modes are assumed to dominate thermal transport for both systems. For the $Co_4Sb_{12-2x}Te_xGe_x$ compounds, $x = 3$ exhibits the lowest phonon dispersion gradient and lattice thermal conductivity, agreeing well with experimental measurements. Our results present the improvement of thermoelectric properties of skutterudite compounds through fillers and substitutional doping.

4.1 Introduction

The combustion of fuel in automobiles is strikingly inefficient where approximately 75% of energy produced during this process is lost as waste heat. Thermoelectric materials can be used to recover some of this waste heat by converting it to useful electrical power for the vehicle. The performance of these materials is determined by a dimensionless figure of merit ZT (see Equation 2.1). Materials with higher ZT values (ZT >1) have greater thermoelectric performance. Such materials must exhibit a high power factor while having low thermal conductivity. In order to meet these criteria, it is important to identify novel materials or substitute existing materials with different species to optimize the ZT value.[1-11]

One class of materials that has potential for thermoelectric applications are skutterudite compounds. These are relatively low-cost and easy to process materials that intrinsically exhibit good electrical transport properties and tunable thermal transport properties with site substitutions.[2,5,9-16] Skutterudites have the space group $Im3$ and consist of cage-like structures with the general formula AB_3 where A is a transition metal and B is a pnictogen. Figure 2.1 shows the crystal structure of a filled skutterudite featuring M filler atoms and B rings within an A sublattice, where M = La, Te, Ge, Ba, In, or Yb; A = Fe, Ru, Co, Ni, or Os; B = Sb, P, or As. Skutterudite compounds generally have a ZT value around 1 and maintain large carrier concentrations and moderate Seebeck coefficients.[17,18] The incorporation of filler atoms reduces their thermal conductivity through the "rattling motion." Alkaline earths have previously been used as fillers[5] and Yang et $al.$[19] have shown that a double-filled skutterudite, having one alkaline earth and one lanthanide (Ba and Ce) filler, is even more effective at reducing the lattice

thermal conductivity than using two alkaline earths (Ba and Sr). The combination of Ca

and Ce used in this report mimics this approach but for elements with greater mass

difference (71% mass difference compared to just 2%). The structure of a skutterudite

also has large degrees of freedom for doping and alloying. This makes it attractive for

customization and design studies.

In addition to incorporating filler atoms, substituting B sites with different species

is another approach to improve the *ZT* value. Cobalt triantimonide ($CoSb_3$) is a

skutterudite of particular interest for power generation because it can operate at high

temperatures ($\approx$900 K). Substitutions that have been investigated for the $CoSb_3$ structure

include Cr,[20] Ni,[21] or Fe,[22] on the Co site, and Ge or Te on the Sb site. These substitutions

reveal significant changes in transport properties such as an increase in electrical

conductivity and a decrease in thermal conductivity; therefore, a fundamental

investigation of fillers and substitutions and their effects on the thermoelectric properties

of skutterudite compounds is important for materials development.

As a follow-up to our previous work,[22] this paper investigates the effect of Ca/Ce

filler atoms in $FeSb_3$ and Te/Ge substitutions on the Sb site in $CoSb_3$. The stoichiometry

of the Ca/Ce double-filled system follows the form $CaCeFe_8Sb_{24}$ but the proper ordering

of the Ca and Ce atoms follows that of Figure 4.1 which requires a supercell of

$Ca_4Ce_4Fe_{32}Sb_{96}$ to describe the system. In $Co_4Sb_{12-2x}Te_xGe_x$, six compositions are

considered where x = 0, 0.5, 1, 2, 3, and 6. This range of compositions offers a complete

look at the substitution up to a complete replacement of the Sb atoms ($Co_4Te_6Ge_6$). To

investigate the atomic structure features, we calculated the lattice constant, *a*, for the

$Ca_{0.5}Ce_{0.5}Fe_4Sb_{12}$ system and lattice constant, *a*, and cell angle, γ, as a function of *x* for

the $Co_4Sb_{12-2x}Te_xGe_x$ system. The atomic, electronic, and phonon dispersion effects were also investigated for each compound. This work helps identify the (Fe,Co)Sb$_3$-type compounds with a stable structure and optimized electrical and thermal conductivity properties, hence improved *ZT* values.
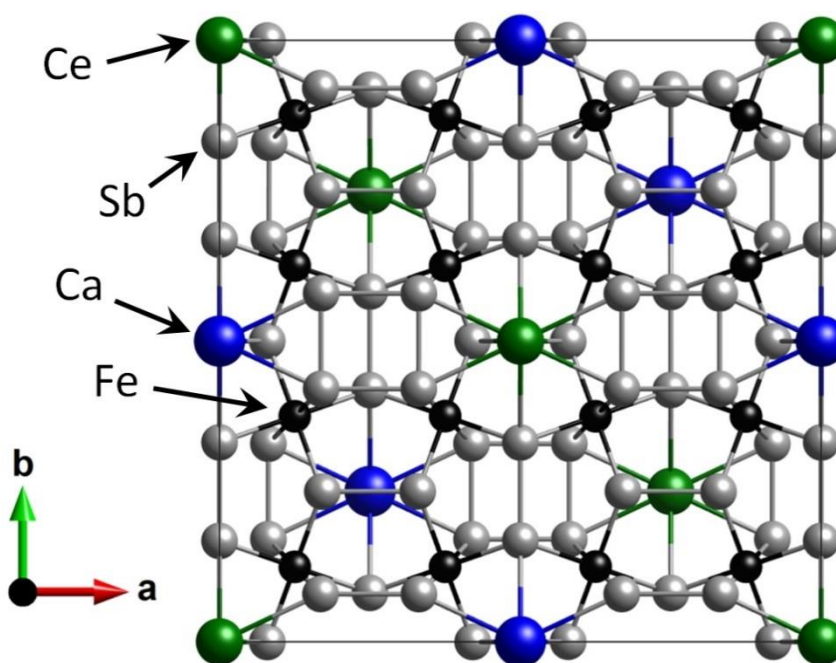
Figure 4.1. **Schematic of the Ca$_4$Ce$_4$Fe$_{32}$Sb$_{96}$ crystal structure where Ca (blue), Ce (green), Fe (black), and Sb (gray) atoms are represented by spheres. The preferred ordering of the filler atoms is to arrange all Ca atoms along (220) planes and all Ce atoms along (110) planes in this 4x4x2 supercell.**

4.2 Computational Methods

Crystal structure and electronic structure calculations were performed within the DFT through implementation of the VASP code.[23] The spin-dependent GGA functional was used with the Perdew-Burke-Ernzerhof (PBE) formalism.[24] Projector augmented wave (PAW) pseudopotentials were employed with a plane wave expansion cutoff of 500 eV and a 6x6x6 Γ-centered *k*-point mesh for Brillouin zone integration.[25,26] Fermi surface

broadening was accounted for by a Gaussian smearing of 0.05 eV for the $FeSb_3$ structures while 0.025 eV was used for the $CoSb_3$ structures. Atomic positions and lattice vectors were relaxed until the residual forces were reduced to less than 0.01 eV/Å. Electronic structure calculations, including DoS and band structure calculations, were carried out on the DFT-optimized structures. A larger *k*-point mesh of 12x12x12 was used for the Brillouin zone integration. These calculations were performed in order to investigate the effects of Ca/Ce fillers and Te/Ge-Sb substitution on the electrical conductivity of the systems. Strong correlation effects were also tested via the DFT+U scheme for the Fe atoms and Co atoms (on-site Coulomb potential $U_{Fe} = 4.5$ eV and $U_{Co} = 7.8$ eV; exchange potential $J_{Fe} = 0.89$ eV and $J_{Co} = 0.92$ eV).[27] This approach is often used to correct the bandgap which is underestimated with DFT alone.

To estimate the thermal properties of each system, DFPT was used to calculate the necessary force constants by means of the Parlinski-Li-Kawazoe method.[28] The phonon density of states and phonon dispersion relations were then generated using the PHONOPY software package.[29] Force constant calculations were performed using an energy cutoff of 400 eV and a *k*-point mesh of 1x1x1 for each structure. To account for long-range phonon interactions, a supercell convergence test was performed for each of the $Co_4Sb_{12-2x}Te_xGe_x$ structures.

The use of these methods and input parameters comes from optimization tests which balance system accuracy with computation costs. For most parameters, this point is reached when a further reduction in total system energy is negligible yet computation time is greatly increased. Once the DFT environment has been optimized, resulting lattice

constants and cell volume data were compared with experimental results to ensure accuracy in the models.

4.3 Results

<u>Structural Effects</u>

The FeSb$_3$ skutterudite has a cubic crystal structure with the *Im*3 space group and consists of Fe and Sb at A and B sites, respectively (Figure 2.1). It has a cage-like structure with two icosahedral voids filled with guest atoms M. Previous work indicated that Ca and Ce atoms as fillers with a 1:1 ratio form Ca$_{0.5}$Ce$_{0.5}$Fe$_4$Sb$_{12}$ and exhibit a higher *ZT* value than that of other (Ca$_x$Ce$_{1-x}$)Fe$_4$Sb$_{12}$ compounds where $x = 0$, 0.25, 0.75, and 1.[22] This is the consequence of large mass difference between Ca and Ce, generating a wider range of resonant rattling frequencies and leading to phonon scattering enhancement and thermal conductivity decrease.

This work further studies the Ca$_{0.5}$Ce$_{0.5}$Fe$_4$Sb$_{12}$ compound. DFT structural calculations indicate a decrease in lattice constant from 9.1805 Å for the unfilled compound to 9.1777 Å (~0.03%) for the double-filled compound, which agrees well with the experimental lattice constant of 9.149056 Å for Ca$_{0.5}$Ce$_{0.5}$Fe$_4$Sb$_{12}$. As shown in Figure 4.1, a large 136 atom 4x4x2 supercell (*i.e.*, Ca$_4$Ce$_4$Fe$_{32}$Sb$_{96}$) was used where the Ca and Ce were arranged with each occupying alternating (110) planes (defined using the 2x2x2 supercell). The structure has average Ca-Sb and Ce-Sb bond lengths of 3.353 Å and 3.361 Å, respectively; Sb-Ca-Sb bond angles of 52.00° and 66.85°; and Sb-Ce-Sb bond angles of 52.09° and 66.82°.

The effects of B-site substitution in skutterudites were also investigated using the CoSb$_3$ system where two Sb atoms are incrementally replaced with Te and Ge atoms,

resulting in the formula $Co_4Sb_{12-2x}Te_xGe_x$, where $x = 0, 0.5, 1, 2, 3,$ and 6. Our optimized

crystal structures and calculated lattice constants, a, were compared with experimental

values, determined by the Rietveld refinement technique and a Rietveld pattern

decomposition technique.[30,31] Table 4.1 shows the calculated and experimental lattice

parameters for $Co_4Sb_{12-2x}Te_xGe_x$ to illustrate the structural effects of B-site substitutions

Te/Ge. The lattice constant a appears to decrease almost linearly as x increases, with the

exception of $x = 2$. These results are expected, given that the covalent radius of Sb (1.40

Å) is larger than that of the substituents Te (1.36 Å) and Ge (1.21 Å).[32] Cell angle γ

slightly shrinks at $x = 0.5, 1,$ and 3, but it enlarges at $x = 6$. These changes indicate that

the symmetry of the $Co_4Sb_{12-2x}Te_xGe_x$ compound is no longer cubic with Te/Ge

substitution. Our DFT results agree well with experimental XRD structural analysis

results (< 1.0% error).

Table 4.1 **Calculated cell angle γ in degrees and lattice parameter a in units of Å for $Co_4Sb_{12-2x}Te_xGe_x$ ($x = 0, 0.5, 1, 2, 3,$ and 6). The experimentally determined lattice parameter a_{exp} and the percent error between calculated and experimental values is also given (subscript $_{exp}$ denotes experimental values).[31] The symbol θ represents the smallest distortion angle in the pnictogen rings. Superscript [a] denotes values taken for the structure with the highest dopant site order (configuration 3).**

x	γ (°)	a (Å)	a_{exp} (Å)	Error %	θ (°)
0	90.00	9.11086	9.03662	0.82	90.00
0.5	89.90	9.08122	9.01633	0.72	88.72
1	89.83	9.06154	8.99555	0.73	85.62
2	90.00	8.88705	8.94781	-0.68	86.40
3	89.96	8.96417	8.89584	0.77	80.87[a]
6	90.26	8.79712	--	--	81.84[a]

In order to better understand the atomic structures, we measured the distances between Co atoms and the rings consisting of Sb/Te/Ge. In experiments, the Co-Sb/Te/Ge distance decreases from 2.53 Å to 2.49 Å as x increases from 0 to 3. While the average Sb/Te/Ge-Sb/Te/Ge distances in the 4-member rings also decreases from 2.91 Å to 2.86 Å, they are longer than the typical Sb-Sb distance of 2.80 Å.[32] DFT calculations reveal that the average Co-Sb/Te/Ge bond distances decrease from 2.54 Å to 2.47 Å from $x = 0$ to 3 and even further decreased to 2.41 Å at $x = 6$, which is consistent with experimental results. From $x = 0.5$ to 2, the Co-Ge bond distance is the shortest compared to the Co-Sb and Co-Te bonds; however, in the $x = 3$ compound, the Co-Te bond distance decreases rapidly and becomes the shortest. Te/Ge substitution at $x = 3$ results in a unique structure. Due to different Co-Sb/Te/Ge bond distances and large Te/Ge substitution concentration, the 4-member rings consisting of Sb/Te/Ge are distorted, and turn into the parallelogram rings shown in Figure 4.2. The distortions depend on the concentration of Te/Ge substitution in the rings. Its angles range from 81° to 93°.
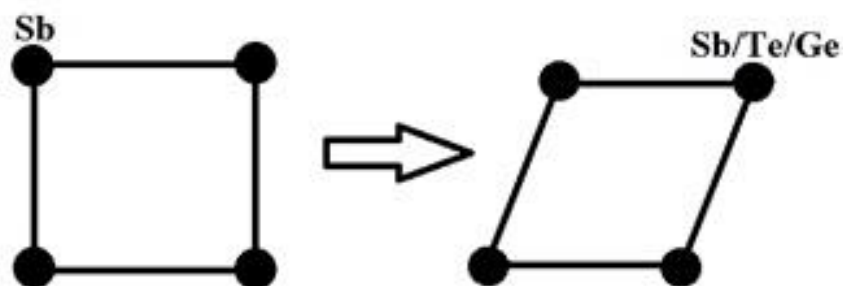
Figure 4.2.   Model depicting pnictogen rings within the filled skutterudite structure. Upon Te/Ge substitution, the ring distorts to an angle of down to 81° for $Co_4Sb_{12-2x}Te_xGe_x$ at $x = 3$.

Electrical Properties

The Ca and Ce filler atoms in $FeSb_3$ affect the electronic structure as well as the crystal structure. As shown in Figure 4.3, the electronic DoS for the Fe_8Sb_{24} structure

shows that the material is already electronically conductive because, at the Fermi level, there is low DoS for the spin-up (positive y-values) and relatively large DoS for the spin-down. The difference in spin-up and spin-down DoS is caused by the magnetism of Fe in the system. The Ca/Ce-filled structure, having the proper Ca-Ce ordering as shown in Figure 4.1, is also electronically conductive but with a more subtle difference between spin-up and spin-down DoS than the unfilled structure. Experimentally, it is shown that this particular Ca-Ce ordered structure is not necessarily the most electronically conductive type of Ca/Ce-filled $FeSb_3$ but is conductive enough to allow for high *ZT* values.[22] Indeed, in Figure 4.3 the presence of a zero-DoS point near the Fermi level could indicate potential for this material to exhibit semi-metallic behavior.
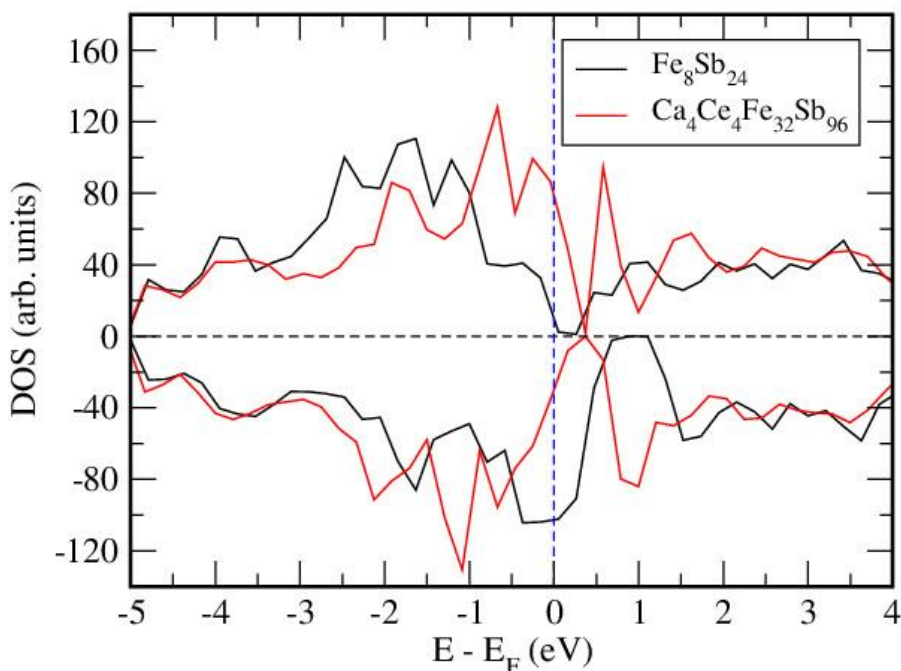
Figure 4.3.   Electronic density of states for the unfilled (black line) and CaCe-filled (red line) FeSb$_3$ structure. In order to account for the correct Ca-Ce ordering as shown in Figure 4.1, a large Ca$_4$Ce$_4$Fe$_{32}$Sb$_{96}$ supercell structure was used. For the sake of comparison, the DoS magnitude for the unfilled structure is increased by a factor of four. Dotted lines depict the zero values on both axes and the x-axis is shifted so the zero-point represents the Fermi level (depicted by the blue dotted line). The up- and down-spin DoS are given by positive and negative values, respectively. The difference

in shape between spin-up and spin-down is primarily caused by the magnetism of the Fe atoms in the system. The unfilled Fe_8Sb_{24} (black) results show a bandgap only for the positive DoS while neither the up- nor down-spin CaCe-filled (red) DoS has a significant bandgap.

Similarly, the electronic conductivity for the $CoSb_3$ structure is affected by the concentration of Te/Ge substitution. Through electronic structure calculations, we studied the Te/Ge substitution effect on the bandgap of each $Co_4Sb_{12-2x}Te_xGe_x$ compound ($x = 0$, 0.5, 1, 2, and 3), which allowed us to predict the electrical conductivity change. Comparison with experimental data[30] validated the computational prediction. Further studies of local density of states provided insight into Co-Te/Ge bonding.

Figure 4.4a shows DoS for $Co_4Sb_{12-2x}Te_xGe_x$. Fermi energy is shifted to 0 eV. At $x = 0$, the compound is semiconducting with a bandgap of ~0.16 eV. As x increases to 0.5, the bandgap decreases. Interestingly, when Te/Ge concentration continues increasing, the bandgap first opens wider but then completely closes at $x = 3$. Such bandgap changes reveal the effect of Te/Ge substitution on the electrical conductivity of the compound. The compound at $x = 0$ is expected to have the smallest electrical conductivity while the highest electrical conductivity occurs at $x = 3$ due to the absence of a bandgap. From $x = 0.5$ to 1, the electrical conductivity should slightly decrease due to the wider bandgap. These computational predictions are consistent with experimental measurements which show that increasing Te concentration in Ge-doped $CoSb_3$ increases the electrical conductivity.[33,34]
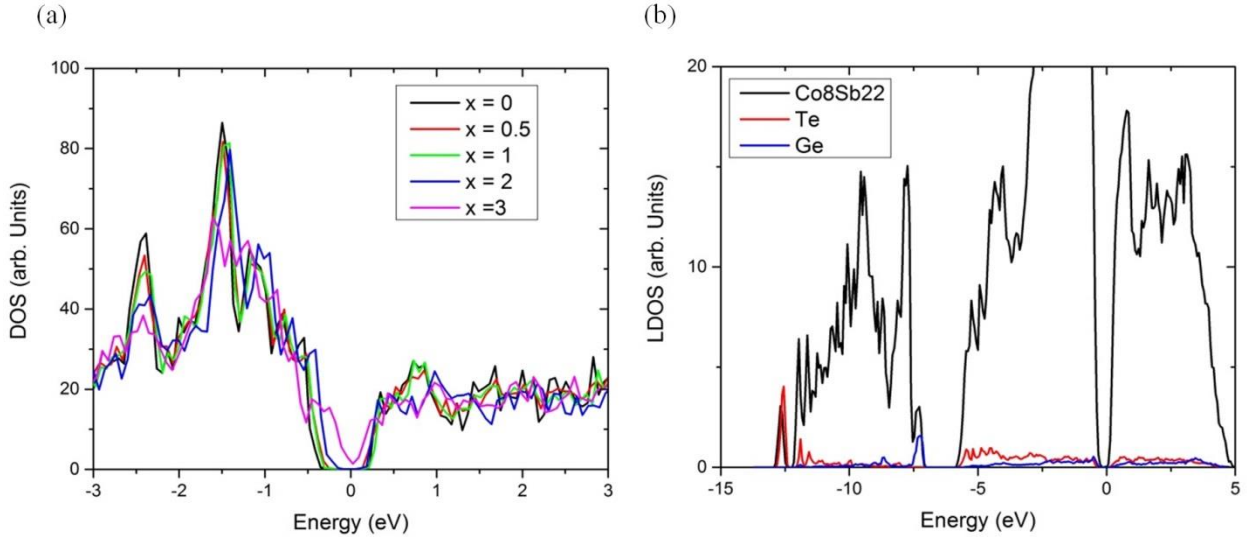
Figure 4.4. **Electronic density of states for $Co_4Sb_{12-2x}Te_xGe_x$, Fermi energy = 0 eV: (a) Total DoS for $x = 0, 0.5, 1, 2,$ and 3; and (b) local DoS (LDoS) for Co_8Sb_{22} (black), Te (red), and Ge (blue) in $Co_8Sb_{22}TeGe$ (*i.e.*, $Co_4Sb_{11}Te_{0.5}Ge_{0.5}$ with $x = 0.5$). DoS results in (a) indicate that the bandgap decreases with increasing x. Part (b) shows an interaction between the local Te and Ge densities indicating orbital hybridization.**

We further studied the local DoS (LDoS), which projected the density on each metal site. Through this approach, the density of states can be split into contributions from each individual atom. When these corresponding plots overlap, it suggests that each atom is contributing to the density of states at that given energy level, implying orbital hybridization. Figure 4.4b illustrates the orbital hybridization through the energy bands of -13 eV to 5 eV between Co and Te/Ge substitution at $x = 0.5$. It indicates the covalent characteristics of Co-Te/Ge bonds due to the overlap of orbital energies. As the Te/Ge concentration increases, the average Co-Te/Ge bond distance decreases because of the stronger covalent nature of the bond.

Further analysis of band alignment facilitates the engineering of the skutterudite compounds for specific thermoelectric applications. The band structures of $Co_4Sb_{12-2x}Te_xGe_x$ for $x = 0, 0.5,$ and 3 were calculated along lines connecting high symmetry points in the Brillouin zone as shown in Figure 4.5. The perfect $CoSb_3$ ($x = 0$) is a direct

bandgap semiconductor with a calculated gap of 0.16 eV. The valence band maximum

(VBM) and conduction band minimum (CBM) are both located at the Γ point. There also

exists an indirect gap at some lower-symmetry point having a local maximum between M

and Γ that is separated from the CBM by 0.50 eV. As Te/Ge substitutions are introduced

($x = 0.5$), the material remains a direct bandgap semiconductor but with a narrower size

of 0.13 eV. This is caused by the decrease in the CBM at the Γ point from 0.084 eV to

0.066 eV. Also, the local maximum at the M point increases (from -0.536 eV to -0.355

eV), giving rise to a shorter indirect gap of 0.42 eV that now exists from M → Γ high-

symmetry points. This implies that with adjusting x values, the compound could shift

from a direct to an indirect bandgap semiconductor, creating more potential applications

for the compounds. To confirm our prediction, we observed $x = 3$ (Figure 4.5c) which

shows the smaller bandgap of 0.11 eV, suggesting a high electrical conductivity. Both the

VBM peak and CBM trough at the Γ point split, forming an indirect gap.
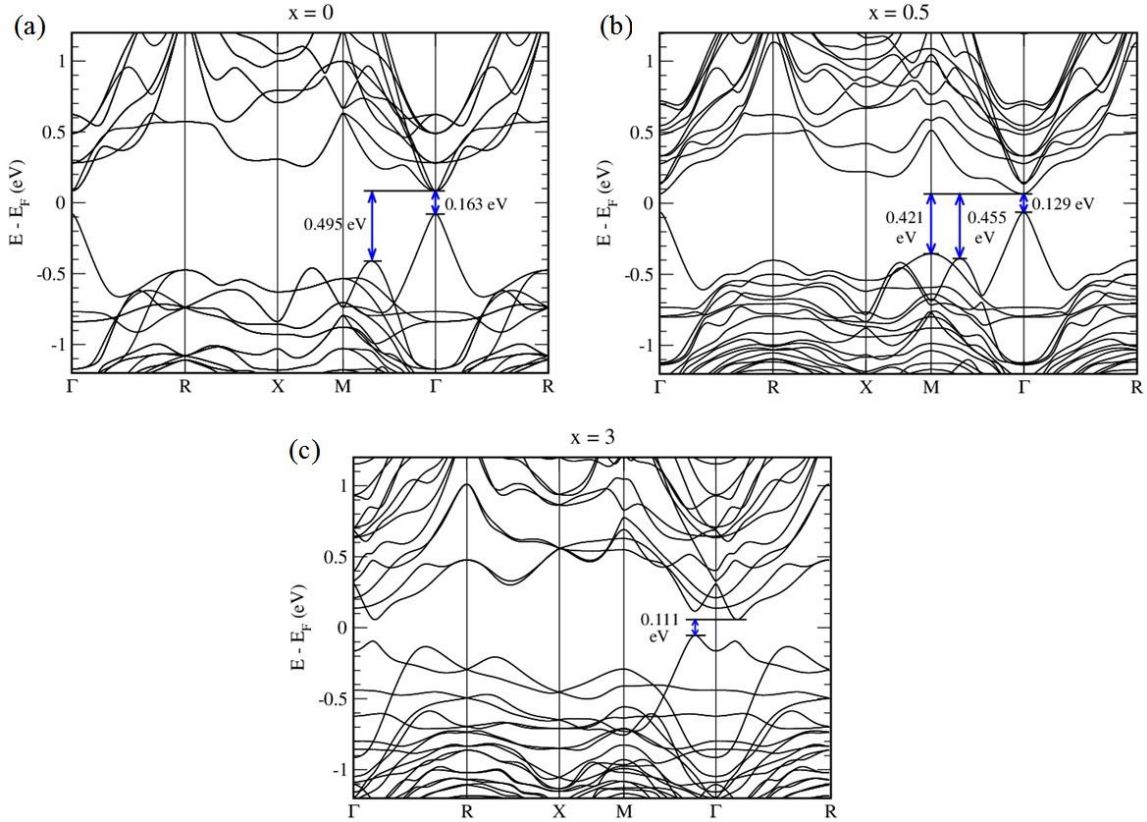
Figure 4.5. Electronic band structure diagrams of Co$_4$Sb$_{12-2x}$Te$_x$Ge$_x$ for (a) $x = 0$, (b) $x = 0.5$, and (c) $x = 3$. Blue arrows indicate the changes in the direct and indirect bandgaps. As substitution increases, the bandgap decreases from (a) 0.16 eV to (b) 0.13 eV, and eventually to (c) 0.11 eV for the highest-doped structure investigated ($x = 3$). Also note the transition from direct to indirect bandgap semiconducting behavior in (c).

The electronic structure results indicate a strong Te/Ge substitution dependence in Co$_4$Sb$_{12-2x}$Te$_x$Ge$_x$, motivating us to investigate further increasing x to the full substitution of Sb with Te/Ge ($x = 6$ or Co$_4$Te$_6$Ge$_6$). Figure 4.6 shows electronic DoS for $x = 6$ (full substitution) in comparison with that for $x = 3$ (half substitution) and different atomic arrangements for Sb, Te, and Ge. In Figure 4.6b, the black line depicts the electronic DoS for $x = 6$, where there is no bandgap and the local minimum in DoS at the Fermi level also has a higher value than that of $x = 3$ (see Figure 4.6a). This suggests a generally increasing conductivity with increasing x. Interestingly, we found that atomic arrangements for Sb, Te, and Ge in the pnictogen rings affect the bandgap size. As seen

in Figure 4.6c, configuration 1 involves the least amount of "order" where the Sb, Te, and Ge atoms are randomly arranged throughout the Sb sites. This is the configuration used for all substituted structures in Figure 4.4a. Ordering refers to having some pnictogen rings composed of entirely Sb and/or having some only 2Te/2Ge rings arranged such that the Te and Ge atoms are at alternating sites around the ring. Configuration 2 is an example of this for the $x = 3$ system. Finally, configuration 3 involves no randomly ordered rings, demonstrating that all Sb atoms are only sharing Sb rings at $x = 3$ and all Te and Ge atoms are only sharing 2Te/2Ge rings arranged as explained above. As a result, pnictogen ring "ordering" increases from configuration 1 to configuration 3. We found that increasing the ring ordering opens up a bandgap and further increases the gap to as much as 0.32 eV and 0.33 eV for $x = 3$ and $x = 6$, respectively (see Figure 4.6a and Figure 4.6b). Our computational results emphasize the importance for understanding the atomic structure of these materials and the atomic structure-electrical property relationships.
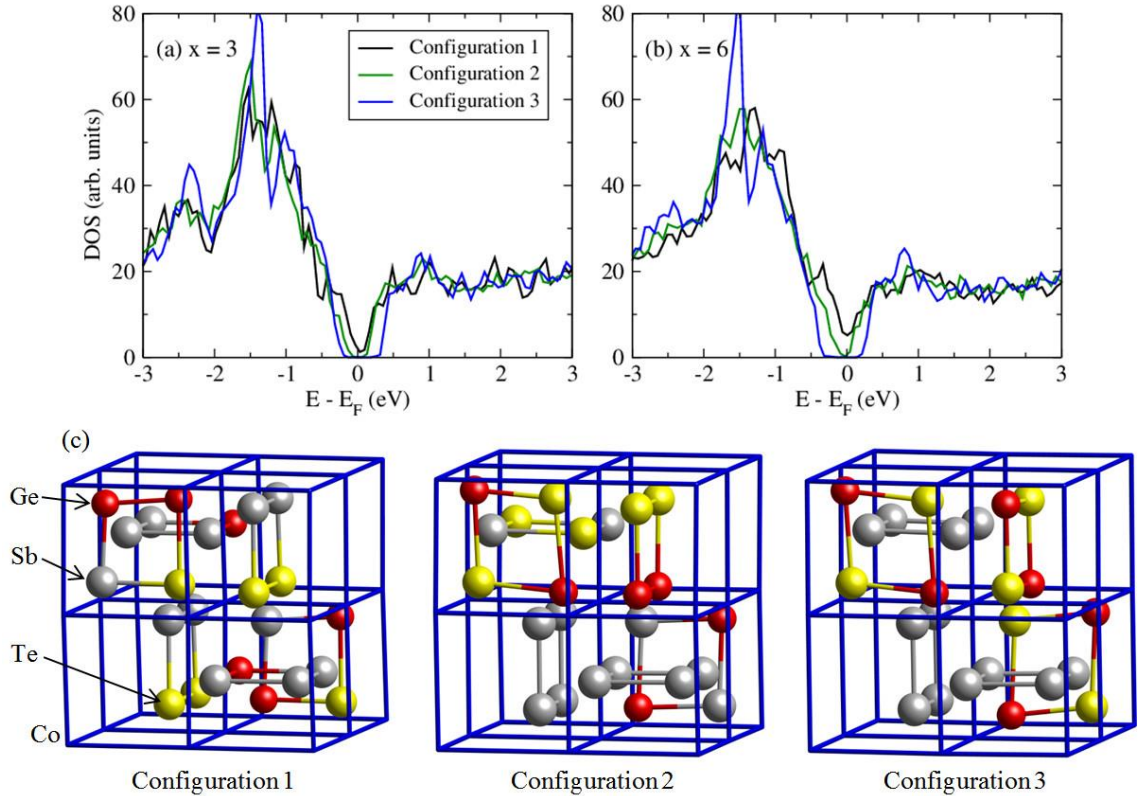
Figure 4.6. Density of states plots for $Co_4Sb_{12-2x}Te_xGe_x$ where (a) $x = 3$ and (b) $x = 6$. Fermi energy is zero. The black, green, and blue plots depict the randomly ordered (configuration 1), the partially ordered (configuration 2), and fully ordered (configuration 3) pnictogen ring configurations. The pnictogen ring ordering increasingly opens up the bandgap. An example of each pnictogen ring configuration (depicted using the $x = 3$ structure) is shown in part (c) where the blue line shows Co-Co bonds and the gray, yellow, and red spheres depict Sb, Te, and Ge atoms, respectively.

Phonon Properties

The scattering of phonon modes in a material hinders thermal transport, which results in reduced lattice thermal conductivity κ_l. There are a variety of methods for increasing phonon scattering, including nanostructuring, alloying, introducing more disorder or interfaces, and changing the structure or composition.[35] By analyzing the phonon dispersion relations of a material, one can estimate the effects of fillers or substitutions on the resulting phonon properties. For example, the phonon group velocity

$v_{k\lambda}$ can be estimated by observing the slopes or gradients of the phonon dispersion data

through the equation

$$v_{k\lambda} = \frac{\partial \omega}{\partial k}, \tag{4.1}$$

where ω is the phonon frequency and k is the wave vector. The phonon group velocity is

then related to the lattice thermal conductivity through the following equation:

$$\kappa_l = \frac{1}{3VN_k}\sum_{k\lambda} c_{k\lambda} v_{k\lambda}^2 \tau_{k\lambda}, \tag{4.2}$$

where V is the volume of the unit cell, N_k is the number of k-points, c is the heat capacity,

and τ is the phonon relaxation time for the given phonon branch, λ.[36,37] From this, the

lattice thermal conductivity can be estimated qualitatively by analyzing the slope of the

phonon dispersion results. Figure 4.7 shows phonon DoS data for the large 136-atom

$Ca_4Ce_4Fe_{32}Sb_{96}$ compound compared to that of Fe_8Sb_{24}. Phonon dispersion data were also

calculated but due to the large number of modes (136 x 3 = 408 modes) for the CaCe-

filled system, the results were more clearly displayed via the phonon DoS instead. We

found that the incorporation of Ca and Ce filler atoms broadens the phonon bands,

implying an increase in phonon scattering typically observed in filled skutterudite

systems. The optical modes are also significantly flatter than the acoustic modes,

suggesting that the lattice thermal conductivity for this material is dominated by the

acoustic modes.
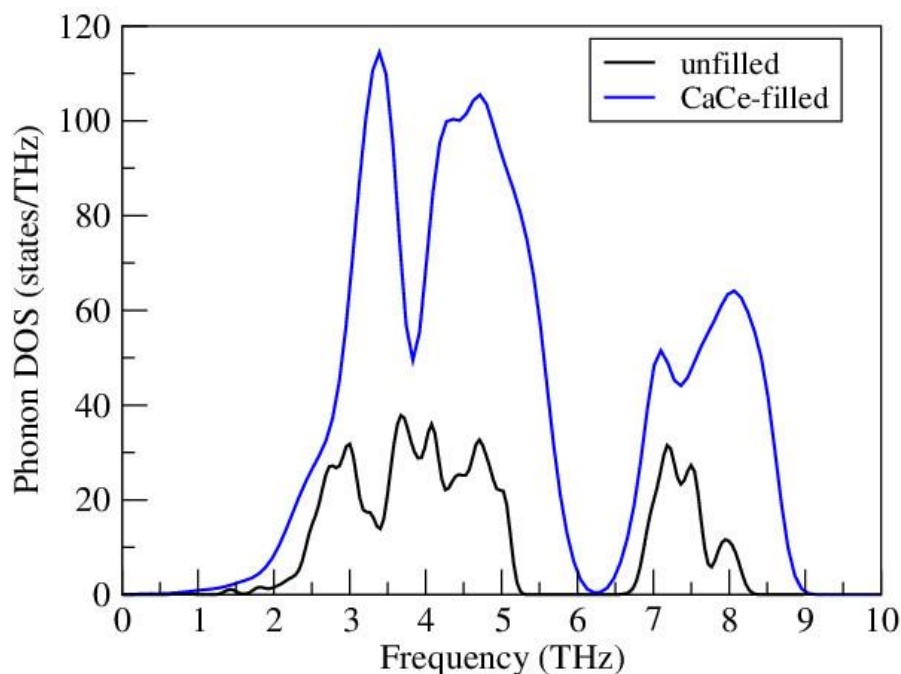
Figure 4.7.   **Phonon density of states for unfilled Fe$_8$Sb$_{24}$ (black) and CaCe-filled Ca$_4$Ce$_4$Fe$_{32}$Sb$_{96}$ (blue). To account for the proper Ca/Ce filler atom ordering which provides the most stable structure (and most promising thermoelectric performance) of the Ca$_{0.5}$Ce$_{0.5}$Fe$_4$Sb$_{12}$ system, the larger 136-atom supercell was used for the "CaCe-filled" structure.**

Similarly, the effects of substitution on lattice thermal conductivity were also estimated by analyzing the phonon properties. Figure 4.8a shows the phonon dispersion relation for the Co$_4$Sb$_{12-2x}$Te$_x$Ge$_x$ compound at $x = 0$. Figure 4.8b compares the acoustic modes for the Co$_4$Sb$_{12-2x}$Te$_x$Ge$_x$ compounds at $x = 0$, 3, and 6, where the x-axes for each data set is normalized to the values of the compound at $x = 6$ (for the purpose of comparison). The compound at $x = 3$ has the lowest phonon dispersion gradient which could indicate that it has the lowest lattice thermal conductivity. Figure 4.8c compares the phonon density of states for the three compounds. It shows a broadening of the phonon bands, particularly for the higher-frequency band, for the compounds with Te and Ge substitutions at $x = 3$ and 6. Ge substitutions contribute to the higher frequency modes since Ge has a lower atomic weight than Sb. In contrast, the modes at the lower

frequencies are associated with the heavier Te substitutions. $x = 0$ exhibits a sizable gap between the higher-frequency band and the lower band. As substitution increases, this gap decreases and is eventually eliminated at $x = 6$. This spreading of optical modes indicates a reduction in lattice thermal conductivity. For either $x = 3$ or $x = 6$, the optical modes are significantly flatter than the acoustic modes, suggesting that the lattice thermal conduction is likely dominated by the acoustic modes in these compounds.
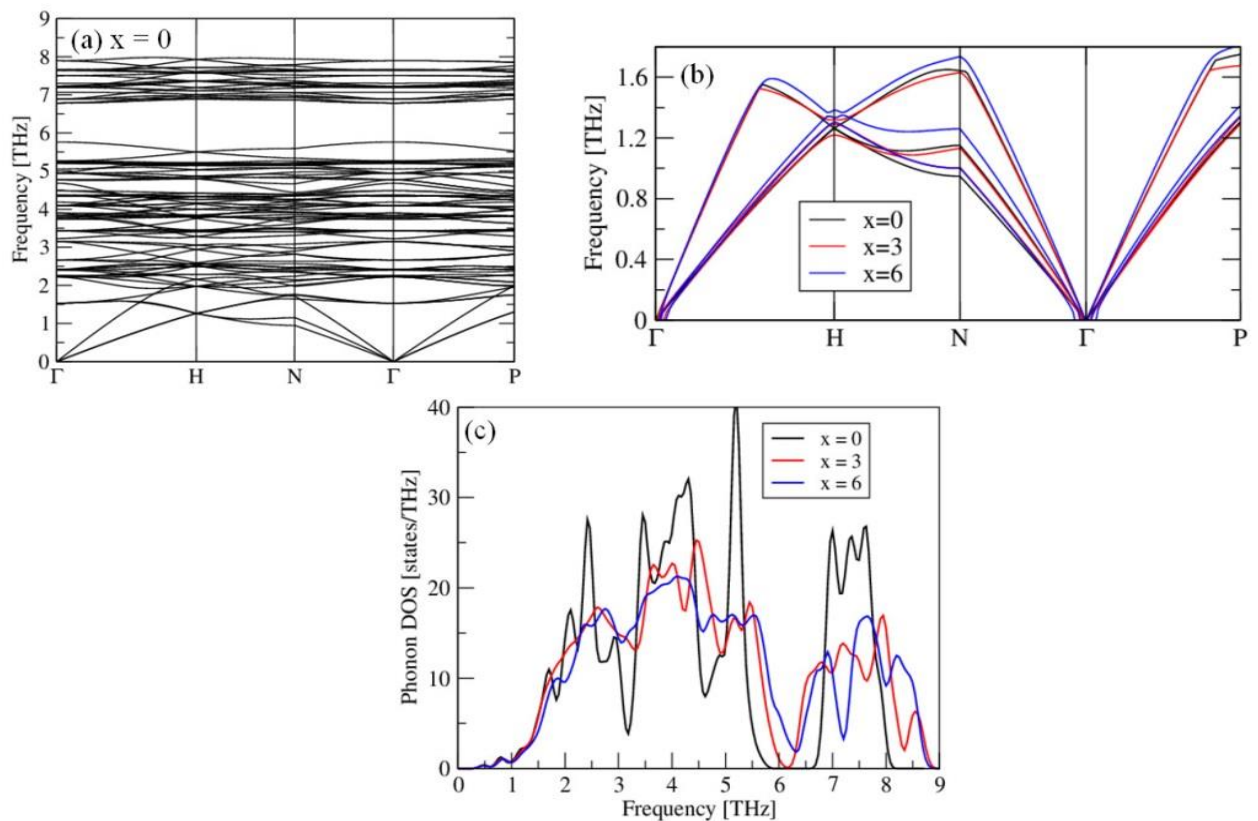
Figure 4.8.   Phonon property calculations. (a) Phonon dispersion relation for Co4Sb12-2xTexGex at $x = 0$. Similar plots were made for $x = 3$ and $x = 6$ but for brevity, only their acoustic modes (along with those of $x = 0$) are given in (b), and (c) total phonon density of states for each compound, projected across the full range of mode frequencies.

4.4 Conclusion

We have investigated the crystal structures, electrical properties, and thermal properties of filled $Ca_{0.5}Ce_{0.5}Fe_4Sb_{12}$ and substituted $Co_4Sb_{12-2x}Te_xGe_x$ compounds ($x = 0$,

0.5, 1, 2, 3, and 6) using a DFT-based approach. The stable Ca/Ce ordering required the use of a large $Ca_4Ce_4Fe_{32}Sb_{96}$ supercell with each filler atom occupying alternating (110) planes. For the $Co_4Sb_{12-2x}Te_xGe_x$ compounds, structural distortion occurs with Te/Ge substitution. At $x = 3$ (*i.e.*, 1:1 Sb:Te/Ge ratio), four-member pnictogen square rings have the largest distortion and become parallelograms with an angle of 81°. Electronic structure calculations indicate that the Ca/Ce double-filled $FeSb_3$ is conductive with no bandgap. The bandgap of $Co_4Sb_{12-2x}Te_xGe_x$ varies with Te/Ge substitution concentration leading to a reduction in bandgap and therefore an increase of electrical conductivity. The covalent characteristics of Co-Te/Ge bonds account for orbital hybridizations between Co and Te/Ge. Band structures exhibit the change of band alignments near the Fermi energy as x increases. At $x = 3$, the compound transfers from a direct to indirect band-gap semiconductor. We also found a strong correlation between the ordering/configuration of pnictogen rings and the electronic bandgap for these compounds. We predicted the thermal conductivity change through the analysis of phonon DoS and phonon dispersion relations for the compounds. The phonon bands are broadened with the incorporation of either fillers or substitutions. Lattice thermal conductivity change is controlled by the acoustic phonon modes in both cases. For the $Co_4Sb_{12-2x}Te_xGe_x$ compounds, phonon scattering and acoustic mode gradient change are evident as substitution increases. The compound at $x = 3$ is expected to have the lowest lattice thermal conductivity. Our work predicts improved thermoelectric properties via filler and substitutional doping. More work will be conducted to confirm the predictions through further *ZT* calculations and measurements.

The overall approach for analyzing these skutterudite systems and investigating their filler and substitution effects can be used to facilitate research on 2D TMD systems in the following chapters. Similar DFT calculations were performed to relax and analyze the structure of 2D TMD materials. Both the methodology for calculating electron and phonon dispersion spectra and the analysis of electrical and phonon properties were applied to our 2D TMD research. The supercell approach for investigating dopants was also used to build metal-site substituted MX_2 structures for Chapter Six and lateral heterostructures for Chapter Seven.

Acknowledgements

References

(1)   Bjerg, L.; Madsen, G. K. H.; Iversen, B. B. Enhanced Thermoelectric Properties in Zinc Antimonides. *Chem Mater* **2011**, *23*, 3907.

(2)   Tan, G. J.; Wang, S. Y.; Li, H.; Yan, Y. G.; Tang, X. F. Enhanced thermoelectric performance in zinc substituted p-type filled skutterudites $CeFe_{4-x}Zn_xSb_{12}$. *Journal of Solid State Chemistry* **2012**, *187*, 316.

(3)   Chrissafis, K.; Bikiaris, D. Can nanoparticles really enhance thermal stability of polymers? Part I: An overview on thermal decomposition of addition polymers. *Thermochimica Acta* **2011**, *523*, 1.

(4)   Dragoman, D.; Dragoman, M. Giant thermoelectric effect in graphene. *Appl Phys Lett* **2007**, *91*, 203116.

(5)   Dyck, J. S.; Chen, W. D.; Uher, C.; Chen, L.; Tang, X. F.; Hirai, T. Thermoelectric properties of the n-type filled skutterudite Ba0.3Co4Sb12 doped with Ni. *J Appl Phys* **2002**, *91*, 3698.

(6)   Freeman, D. D.; Choi, K.; Yu, C. N-Type Thermoelectric Performance of Functionalized Carbon Nanotube-Filled Polymer Composites. *Plos One* **2012**, *7*, e47822.

(7)   Zhao, Y.; Tang, G. S.; Yu, Z. Z.; Qi, J. S. The effect of graphite oxide on the thermoelectric properties of polyaniline. *Carbon* **2012**, *50*, 3064.

(8)   Lan, Y.; Minnich, A. J.; Chen, G.; Ren, Z. Enhancement of Thermoelectric Figure-of-Merit by a Bulk Nanostructuring Approach. *Advanced Functional Materials* **2010**, *20*, 357.

(9)   Wong-Ng, W.; Kaduk, J. A.; Tan, G.; Yan, Y.; Tang, X. X-ray powder reference patterns of the Fe(Sb2+xTe1-x) skutterudites for thermoelectric applications. *Powder Diffraction* **2014**, *29*, 260.

(10)   Tan, G. J.; Liu, W.; Chi, H.; Su, X. L.; Wang, S. Y.; Yan, Y. G.; Tang, X. F.; Wong-Ng, W.; Uher, C. Realization of high thermoelectric performance in p-

type unfilled ternary skutterudites FeSb2+xTe1-x via band structure modification and significant point defect scattering. *Acta Materialia* **2013**, *61*, 7693.

(11)   Yan, Y. G.; Wong-Ng, W.; Kaduk, J. A.; Tan, G. J.; Xie, W. J.; Tang, X. F. Correlation of thermoelectric and microstructural properties of p-type CeFe4Sb12 melt-spun ribbons using a rapid screening method. *Appl Phys Lett* **2011**, *98*.

(12)   He, T.; Chen, J. Z.; Rosenfeld, H. D.; Subramanian, M. A. Thermoelectric properties of indium-filled skutterudites. *Chem Mater* **2006**, *18*, 759.

(13)   Huang, B.; Kaviany, M. Filler-reduced phonon conductivity of thermoelectric skutterudites: Ab initio calculations and molecular dynamics simulations. *Acta Materialia* **2010**, *58*, 4516.

(14)   Hara, R.; Inoue, S.; Kaibe, H. T.; Sano, S. Aging effects of large-size n-type CoSb3 prepared by spark plasma sintering. *Journal of Alloys and Compounds* **2003**, *349*, 297.

(15)   Kim, H.; Kaviany, M.; Thomas, J. C.; Van der Ven, A.; Uher, C.; Huang, B. L. Structural Order-Disorder Transitions and Phonon Conductivity of Partially Filled Skutterudites. *Phys Rev Lett* **2010**, *105*, 265901.

(16)   Luo, P. F.; Tang, X. F.; Xiong, C.; Zhang, Q. J. Effect of multiwalled carbon nanotubes on the thermoelectric properties of p-type Ba0.3FeCo3Sb12 compounds. *Acta Phys Sin-Ch Ed* **2005**, *54*, 2403.

(17)   Morelli, D. T.; Caillat, T.; Fleurial, J. P.; Borshchevsky, A.; Vandersande, J.; Chen, B.; Uher, C. Low-Temperature Transport-Properties of P-Type Cosb3. *Phys Rev B* **1995**, *51*, 9622.

(18)   Caillat, T.; Borshchevsky, A.; Fleurial, J. P. Properties of single crystalline semiconducting CoSb3. *J Appl Phys* **1996**, *80*, 4442.

(19)   Yang, J.; Zhang, W.; Bai, S. Q.; Mei, Z.; Chen, L. D. Dual-frequency resonant phonon scattering in BaxRyCo4Sb12 (R=La, Ce, and Sr). *Appl Phys Lett* **2007**, *90*, 192111.

(20)   Yang, J.; Endres, M. G.; Meisner, G. P. Valence of Cr in skutterudites: Electrical transport and magnetic properties of Cr-doped CoSb3. *Phys Rev B* **2002**, *66*.

(21)   Yang, J.; Morelli, D. T.; Meisner, G. P.; Chen, W.; Dyck, J. S.; Uher, C. Influence of electron-phonon interaction on the lattice thermal conductivity of Co1-xNixSb3. *Phys Rev B* **2002**, *65*.

(22)   Yan, Y. G.; Wong-Ng, W.; Li, L.; Levin, I.; Kaduk, J. A.; Suchomel, M. R.; Sun, X.; Tan, G. J.; Tang, X. F. Structures and thermoelectric properties of double-filled (CaxCe1-x)Fe4Sb12 skutterudites. *Journal of Solid State Chemistry* **2014**, *218*.

(23)   Kresse, G.; Furthmuller, J. Efficient iterative schemes for ab initio total-energy calculations using a plane-wave basis set. *Phys Rev B* **1996**, *54*, 11169.

(24)   Perdew, J. P.; Burke, K.; Ernzerhof, M. Generalized gradient approximation made simple. *Phys Rev Lett* **1996**, *77*, 3865.

(25)   Blöchl, P. E. Projector augmented-wave method. *Phys Rev B* **1994**, *50*, 17953.

(26)   Kresse, G.; Joubert, D. From ultrasoft pseudopotentials to the projector augmented-wave method. *Phys Rev B* **1999**, *59*, 1758.

(27)   Liechtenstein, A. I.; Anisimov, V. I.; Zaanen, J. Density-functional theory and strong interactions: Orbital ordering in Mott-Hubbard insulators. *Phys Rev B* **1995**, *52*, R5467.

(28)   Parlinski, K.; Li, Z. Q.; Kawazoe, Y. First-principles determination of the soft mode in cubic ZrO2. *Phys Rev Lett* **1997**, *78*, 4063.

(29)   Togo, A.; Oba, F.; Tanaka, I. First-principles calculations of the ferroelastic transition between rutile-type and CaCl(2)-type SiO(2) at high pressures. *Phys Rev B* **2008**, *78*, 134106.

(30)   Su, X.; Yan, Y.; Wong-Ng, W.; Williamson, I.; Her, L. J.-Y.; Kaduk, J. A.; Li, L. *Powder Diffraction* **2015**, *in preparation*.

(31)   Rietveld, H. M. A Profile Refinement Method for Nuclear and Magnetic Structures. *J Appl Crystallogr* **1969**, *2*, 65.

(32)   Pyykko, P.; Atsumi, M. Molecular Single-Bond Covalent Radii for Elements 1-118. *Chemistry: A European Journal* **2009**, *15*, 186.

(33)   Su, X. L.; Li, H.; Guo, Q. S.; Tang, X. F.; Zhang, Q. J.; Uher, C. Structure and Thermoelectric Properties of Te- and Ge-Doped Skutterudites CoSb2.875-xGe0.125Tex. *Journal of Electronic Materials* **2011**, *40*, 1286.

(34)   Su, X. L.; Li, H.; Wang, G. Y.; Chi, H.; Zhou, X. Y.; Tang, X. F.; Zhang, Q. J.; Uher, C. Structure and Transport Properties of Double-Doped CoSb2.75Ge0.25-xTex (x=0.125-0.20) with in Situ Nanostructure. *Chem Mater* **2011**, *23*, 2948.

(35)   Snyder, G. J.; Toberer, E. S. Complex thermoelectric materials. *Nature Materials* **2008**, *7*, 105.

(36)   Luo, T. F.; Garg, J.; Shiomi, J.; Esfarjani, K.; Chen, G. Gallium arsenide thermal conductivity and optical phonon relaxation times from first-principles calculations. *Europhysics Letters* **2013**, *101*, 16001.

(37)   Chung, J. D.; McGaughey, A. J. H.; Kaviany, M. Role of phonon dispersion in lattice thermal conductivity modeling. *Journal of Heat Transfer: Transactions of the ASME* **2004**, *126*, 376.

CHAPTER FIVE: HIGH-THROUGHPUT COMPUTATIONAL SCREENING OF
ELECTRICAL AND PHONON PROPERTIES OF TWO-DIMENSIONAL
TRANSITION METAL DICHALCOGENIDES*

*This chapter includes modifications from the originally published version and is adapted
from:

I. Williamson, A. Correa Hernandez, W. Wong-Ng, L. Li, "High-throughput
computational screening of electrical and phonon properties of two-dimensional
transition metal dichalcogenides." *JOM*, **68**(10) 2666 (2016). doi:10.1007/s11837-016-
2068-x.

High-throughput computational screening of electrical and phonon properties of two-dimensional transition metal dichalcogenides

Izaak Williamson[a]

Andres Correa Hernandez[a]

Winnie Wong-Ng[b]

Lan Li[a,c]

Published in:

JOM

October 2016

[a]*Micron School of Materials Science and Engineering, Boise State University,*

Boise, ID 83725.

[b]*Materials Measurement Science Division, National Institute of Standards and*

Technology,

Gaithersburg, MD 20899.

[c]*Center for Advanced Energy Studies,*

Idaho Falls, ID 83401.

Abstract

Two-dimensional transition metal dichalcogenides (2D TMDs) are of broadening research interest due to their novel physical, electrical, and thermoelectric properties. Having the chemical formula MX_2, where M is a transition metal and X is a chalcogen, such materials present many possible combinations to consider for materials-by-design exploration. By identifying novel compositions and utilizing the lower dimensionality, which allows for improved thermoelectric performance (*e.g.*, increased Seebeck coefficients without sacrificing electron concentration), MX_2 materials are potential candidates for electronic and energy applications; however, to develop these materials for wide-scale use, it is crucial to comprehensively understand the compositional affects. This work investigates the structure, electronic, and phonon properties of 18 different MX_2 material compositions as a benchmark to explore the impact of various elements. There is significant correlation between properties of constituent transition metals (atomic mass and radius) and the structure/properties of the corresponding 2D TMDs. As the mass of M increases, the *n*-type power factor and phonon frequency gap increases. Similarly, increases in the radius of M lead to increased layer thickness and Seebeck coefficient, *S*. Our results identify key factors to optimize MX_2 compositions for desired performance.

5.1 Introduction

TMDs, having the chemical formula MX_2 (M = transition metal, X = chalcogen, *e.g.*, S, Se, Te), have received attention over the years for having interesting magnetic[1,2] and photoelectric[3] properties. Bulk three-dimensional transition metal dichalcogenides (3D TMDs) can exist as layered structures wherein each layer consists of a transition

metal (M) sheet sandwiched between two chalcogen (X) sheets. These layers exist in one of two structure types: 2H-type having D_{6h} point group symmetry and 1T-type having D_{3d} point-group symmetry. Strong covalent bonding exists within the MX_2 layers (along the a and b axes) while much weaker van der Waals (vdW) interactions exist between the layers (along the c axis). This allows individual MX_2 layers to be separated via mechanical exfoliation.[4] The separated 2D TMD materials have recently attracted much interest for a variety of applications including electronics,[5-9] optoelectronics,[10-13] catalysis,[14,15] and thermoelectrics.[16-19] Thermoelectrics convert waste heat into electric power, governed by figure of merit, ZT (see Equation 2.1). Common thermoelectric materials include clathrates,[20] half-Heusler alloys,[21] and skutterudites.[22-25] Reduced dimensionality offers the potential for smaller device features and has been shown to greatly reduce short-channel effects, increase the on–off ratio, and reduce switching voltage in field-effect transistors (FET).[7,10] In addition, the quantum confinement effect and sharp features in the electronic DoS are beneficial for greatly improving thermoelectric properties, such as increasing S in 2D TMDs compared to that of the bulk structures.[26-28] It is also predicted that the lower dimensionality increases diffusive boundary scattering, effectively reducing the thermal conductivity, κ. Lowering the dimensionality of Si, for example, has shown strong reductions in thermal conductivity and implications for enhanced thermoelectric performance.[29,30] Each of these factors contributes to the strong motivation for further understanding the behavior of 2D TMDs.

With a large number of potential 2D TMD compounds, it is important to identify key structure–property–performance relationships in order to screen preferred materials. A few studies have been performed to analyze the stability and electronic structure of 2D

TMDs and TMOs (transition metal dioxides) using DFT.[5,6] These offer a general analysis of trends across a broad range of compositions and identify most structures to be semiconducting with small indirect bandgaps. Rasmussen *et al.*[6] found that only CrX_2, MoX_2, and WX_2 systems exhibit direct bandgaps. From these works, it is useful to identify more favorable 2D TMD compositions in terms of stability, electrical properties, and optical properties; however, none have been directed at what compositions are possible. Graedel *et al.*[31] developed a method for quantifying the environmental implications, supply risk, and vulnerability to supply restrictions for 62 transition metals and metalloids. These ''criticality scores'' can be used to identify preferred materials and narrow the focus for screening potential compositions in order to develop high-performance, cost-effective, and environmentally friendly materials.

In this work, we used existing stability reference data in conjunction with criticality scores to identify transition metals and resulting 2D TMD compounds to represent a narrowed scope of feasible options for MX_2 materials screening purposes. A list of six transition metals was selected to offer a range of common oxidation states, atomic masses, and atomic radii. Combined with three chalcogens—S, Se, and Te—this amounted to 18 total compounds. The geometries, electrical properties, and phonon properties of these compounds were investigated through first-principles calculation and analyzed with respect to physical properties of the transition metals. This unique approach offers a means of identifying general trends in constituent elements in order to predict structure–properties–performance relationships in resulting 2D TMDs.

5.2 Computational Methods

Structural and electronic structure calculations were conducted using the PAW method[32,33] within the framework of DFT via the VASP code.[34] The PBE[35] formalism was employed within the spin-dependent GGA. A plane-wave expansion cutoff of 500 eV was used along with an automatic Γ-centered 12x12x1 k-point mesh Brillouin zone integration for the initial geometry optimizations. A Gaussian smearing of 0.025 eV was used to account for Fermi surface broadening while atomic positions and basis vectors were relaxed to within 0.01 eV/Å. To avoid image interaction, MX_2 sheets were separated by a distance >20 Å. After geometry optimizations, the electronic structure calculations were performed with an increased k-point mesh of 24x24x1 while strong correlation effects were accounted for using the DFT+U scheme for all transition metals. The on-site Coulomb potentials of U = 4.38, 8.0, 3.0, 8.0, 6.0, and 8.0 eV were used for Mo, Ni, Sc, Ti, V, and W, respectively.[36] The on-site exchange potential, J = 1.0 eV, was used for all metals.

Force constants used to estimate phonon properties were calculated using DFPT following the method of Parlinski-Li-Kawazoe.[37] To calculate the real-space force constants, long-range effects were accounted for by using a converged supercell size of 3x3x2 and a corresponding k-point mesh of 4x4x2. The resulting force constants were used to generate phonon DoS and partial phonon DoS.[38]

In bulk TMD structures, it is necessary to employ vdW corrections to account for the inter-sheet interactions as they are determined to be largely controlled by vdW forces. Indeed, our own comparison of bulk MoS_2 (using the Grimme DFT-D2 method[39] and a 12x12x4 k-point mesh) with that of reported experimental values[40] revealed that

accounting for vdW forces increases the accuracy by about 24.5 % and 11.9 % for sheet separation distance and cell volume, respectively; however, since the bonding within the 2D TMD sheets is primarily strongly covalent, it may not be necessary to include such corrections for calculations involving the isolated sheets. We tested for 2D MoS_2 and found that incorporating vdW corrections gave the same lattice constant and layer thickness values (to within 0.3 % error) yet produced an *indirect* bandgap of 1.65 eV. Since 2D MoS_2 is known to be a *direct* bandgap semiconductor,[41] it would seem that DFT-D2-based vdW corrections actually have a negative impact on 2D TMD systems. Due to the minimal difference in geometry and potential error in the electronic structure calculations, we did not employ vdW in this work.

Similar to the skutterudite modeling approach, each of the DFT parameters in this chapter were optimized through convergence tests. These tests are meant to provide the most accurate ground state that can be reasonably obtained while investigating eighteen different compounds. Our calculated lattice constants, bond lengths and angles, and electronic bandgaps were compared with literature values where available[5,6] to validate our results.

5.3 Results

<u>Structure Screening</u>

The unique physical, electrical, and thermal properties of 2D TMDs are of great research interest for a wide range of applications. However, there are many possible MX_2 combinations to consider. Work by Graedel *et al.* highlights the "criticality scores" for transition metals, allowing for the comparison of three important factors to consider for materials design: environmental implications, supply risk, and vulnerability to supply

restrictions.[31] By comparing this list with the stability results from Ataca et al.[5] and

Rasmussen et al.,[6] we have narrowed the list of favorable transition metals to six: Mo, Ni,

Sc, Ti, V, and W. These metals offer a broad range of atomic masses (44.96–183.85 u),[42]

atomic radii (0.62–0.885 Å),[43] and most common oxidation state (+2 to +6). The

comparison of the calculated properties with regard to these factors offers an effective

approach towards identifying key relationships between constituent elements and desired

structural, electrical, and thermal properties.

Table 5.1 **Oxidation state, atomic mass (u), and atomic radius (Å) for each transition metal. The 2D TMDs (MX$_2$), consisting of a transition metal (*M*) and chalcogen (*X*), have either 2H- or 1T-type structures. Lattice parameter *a* (Å), layer thickness *t* (Å), and electronic bandgap *E$_g$* (eV) of the corresponding TMD are also given. [a]Reference.[41] [b]Reference.[42] Values taken from list of crystal radii with +4 charge and six-fold coordination. [c]Value for +3 charge. [d]*E$_F$* sits on mid-gap state.**

M	Oxidation state	Atomic mass[a] (u)	Atomic radius[b] (Å)	*X*	Type	*a* (Å)	*t* (Å)	*E$_g$* (eV)
Mo	+6	95.94	0.79	S	2H	3.182	3.128	1.69
				Se	2H	3.319	3.338	1.46
				Te	2H	3.549	3.611	1.10
Ni	+2	58.69	0.62	S	1T	3.351	2.336	0.01
				Se	1T	3.545	2.479	–
				Te	2H	3.720	2.927	–
Sc	+3	44.956	0.885[c]	S	2H	3.777	2.708	1.72[d]
				Se	2H	3.512	3.635	–
				Te	2H	3.728	4.009	–
Ti	+4	47.88	0.745	S	1T	3.398	2.854	1.18
				Se	2H	3.485	3.239	0.92
				Te	2H	3.736	3.571	0.30
V	+5	50.942	0.72	S	1T	3.174	2.938	–
				Se	2H	3.335	3.197	0.72
				Te	2H	3.596	3.502	0.02
W	+6	183.85	0.80	S	2H	3.181	3.139	1.85
				Se	2H	3.317	3.355	1.58
				Te	2H	3.552	3.623	1.07

The complete list of eighteen 2D TMDs used in this study is given in Table 5.1. The most common oxidation state, atomic mass, and atomic radius are listed for each transition metal (M). The resultant TMD forms either a 2H- or 1T-type phase. The TMD lattice parameter, a, is typically similar to the layer thicknesses except in the case of ScS_2 and the NiX_2 system (with layer thicknesses about 1 Å smaller than a). Also, both the lattice parameter and layer thickness increase with the atomic number of X. The range of values for both the lattice parameter and layer thickness noticeably decreases with increasing oxidation state of the transition metal. Similarly, this range also decreases with increasing atomic mass of the transition metal down to within < 0.5 Å for both the MoX_2 and WX_2 systems ($m_{Mo} = 95.94$ u, $m_W = 183.85$ u). Figure 5.1 shows how the lattice parameter and layer thickness of the resulting 2D TMD are influenced by the atomic mass and atomic radius of the constituent transition metal. Interestingly, the layer thickness increases with atomic radius of the transition metal while the lattice parameter remains constant. The results reveal some materials design principles that lattice mismatch – causing a large instability in the formation of heterostructures – is minimal or negligible, even though 2D TMDs have large layer thickness differences.
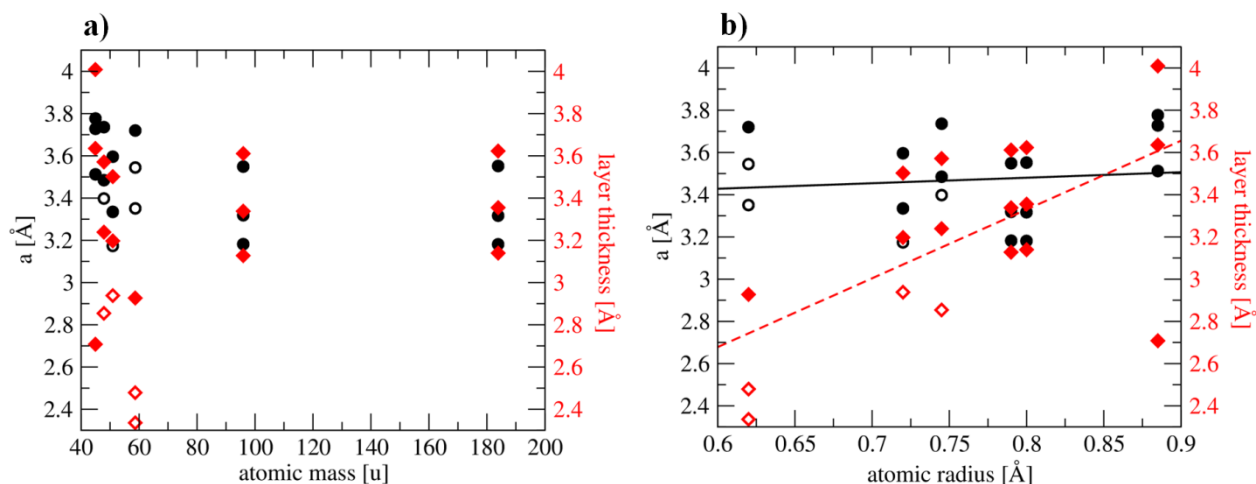
Figure 5.1. **Effects of (a) atomic mass and (b) atomic radius of the transition metal on the lattice constant, *a*, and layer thickness of the resulting 2D TMD structure. Circles and diamonds refer to lattice constant and layer thickness values, respectively. Open and filled data points refer to 1T- and 2H-type MX_2 structures, respectively. Solid and dashed linear trend lines have been added to plot (b) to guide the eye for lattice constant and layer thickness data, respectively.**

Electrical Property Screening

Electronic structure calculations were performed for the 2D TMDs and

determined that many of the systems exhibit semiconducting behavior. The MoX_2, TiX_2,

and WX_2 systems all have nonzero bandgaps with Fermi levels just above their respective

VBM. The magnitude for each bandgap decreases with the increasing atomic number of

X. Specifically, the MoX_2 and WX_2 systems have bandgaps similar to each other, and

they are the only systems with direct bandgaps. These results are consistent with the

findings of Rasmussen *et al.*[6] In contrast, the NiX_2, ScX_2, and VX_2 systems all exhibit *p*-

type semiconducting behavior with Fermi levels below the VBM. The only member of

the VX_2 system with a mid-gap Fermi level is VSe_2 – a semiconductor with an indirect

bandgap of 0.72 eV. Generally speaking, the compounds exhibiting the largest bandgaps

are the ones that involve mid-level transition metal radii. The most conductive

compounds have either very large (Sc) or very small (Ni) atomic radii, implying a Gaussian distribution of bandgaps across the range of atomic radii.

To further investigate electrical properties, the power factor $S^2\sigma$ (a crucial metric for the performance of thermoelectric materials, see Equation 2.1) and S were also calculated for each TMD. The BTE was solved in order to calculate semi-classic transport coefficients.[44] The S data is shown in Figure 5.2 as a function of carrier concentration. Each calculation was evaluated for the temperature of 300 K. Consistent with the bandgaps, the MoX_2, TiX_2, and WX_2 systems show the largest-magnitude S values (nearly 1000 µV/K for the given carrier concentration range) while the other systems produced much smaller values (< 50 µV/K). Also, the MoX_2 and WX_2 systems yield similar plots for all cases except the n-type S calculation for the MTe_2 structures (see Figure 5.2f). The $TiTe_2$ results show a noticeable peak in the S of about 450–500 µV/K for both p- and n-type calculations. It suggests a bipolar conduction for carrier concentrations below 10^{11} carriers/cm^2 and an optimum S value for this system. This bipolar effect could cause degradation in the thermoelectric performance.
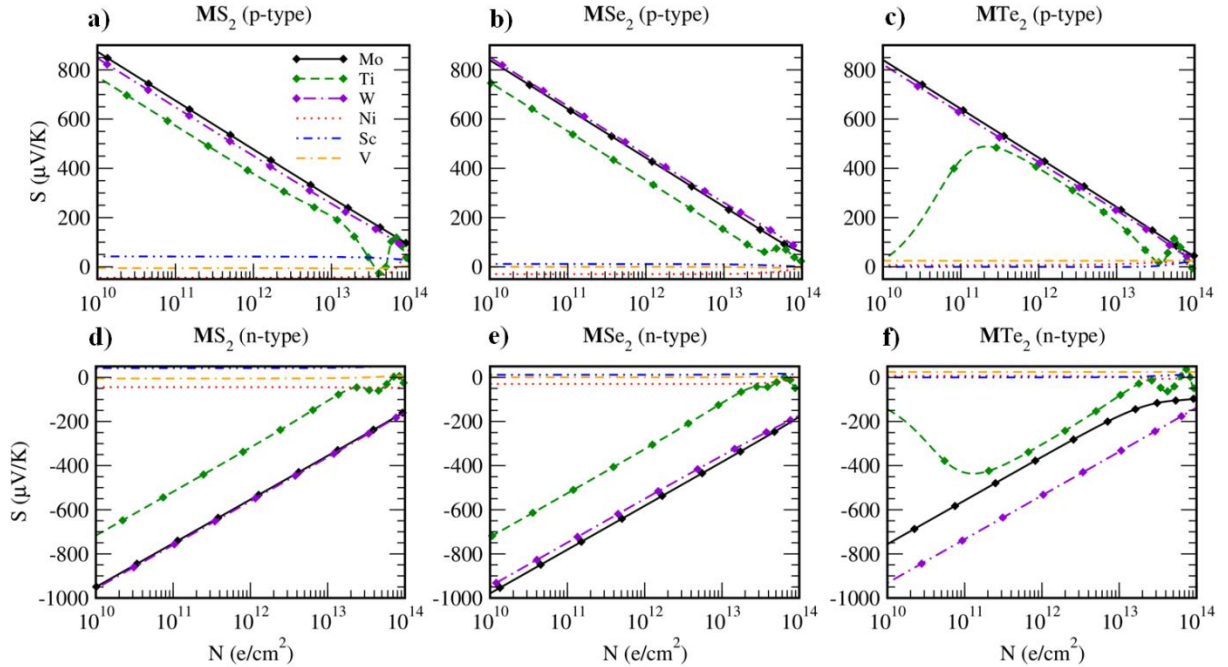
Figure 5.2. **Seebeck coefficient, *S* (µV/K), calculated as a function of carrier concentration *N* (e/cm²) for 2D TMDs. Plots (a)-(c) show the *p*-type *S* values while plots (d)-(f) depict *n*-type values. The first (a, d), second (b, e), and third (c, f) columns compare the MS₂, MSe₂, and MTe₂ systems, respectively. The MoX₂, TiX₂, and WX₂ systems all exhibit semiconducting behavior and are distinguished by lines with diamonds (Mo diamonds-solid line, Ti diamonds-dashed line, and W diamonds-dot-dashed line). The more-conductive NiX₂, ScX₂, and VX₂ systems all exhibit low *S* values and are depicted using lines (Ni dotted line, Sc dot-dot-dashed line, and V dash-dash-dotted line). All calculations were performed at the temperature of 300 K.**

The *S* values were combined with electrical conductivity (σ/τ) calculations, and using the constant relaxation time approximation,[45,46] the $S^2\sigma$ values were calculated. The choice of relaxation time (τ) comes from the work of Kaasbjerg *et al.*[47] who used DFT to calculate the effective electron mass ($m^* = 0.48\, m_e$) and electron mobility in single layer MoS$_2$. At 300 K, and for carrier densities between 10^{11} and 10^{13} cm^{-2}, they calculated an electron mobility of about µ = 400 cm²V⁻¹s⁻¹. Using the equation $\mu = \frac{q}{m^*}\tau$, where *q* is the electronic charge, the average relaxation time equates to about $\tau \approx 10^{-13}$ s. This value was used for each system and the resulting first-peak maximum $S^2\sigma$ values are given in Table 5.2. The *n*-type results indicate a correlation between the magnitude of the

$S^2\sigma$ and the mass of the constituent transition metal. The heaviest metals, W and Mo,

produce the largest $S^2\sigma$ of $7.90*10^{-3}$ and $5.82*10^{-3}$ W/m/K^2, respectively, while the

lightest metal, Sc, has the smallest $S^2\sigma$ (0.78 to 1.39)$*10^{-3}$ W/m/K^2. The type of

chalcogen does not have a large impact on the $S^2\sigma$ of the resultant TMD. For example,

the TiX$_2$ system has a range of only $0.04*10^{-3}$ W/m/K^2. This could be useful for design

purposes, where necessary restrictions on the use of chalcogen would likely not affect the

overall performance of the material. The p-type $S^2\sigma$ results, however, are not as

consistent. Many of the systems exhibit large dependence on the type of chalcogen used.

For example, the NiX$_2$ system has a range of values exceeding $7.83*10^{-3}$ W/m/K^2.

Table 5.2 **Power factor ($S^2\sigma$) values for the 18 2D TMDs. Values are reported as 10^3 times larger than actual for the purpose of clarity in the table. Each value, when multiplied by 10^{-3}, yields units of W/m/K^2. These are calculated at 300 K for both n- and p-type.**

			$S^2\sigma*10^{-3}$ (W/m/K^2)	
M	X	Type	n–type	p–type
Mo	S	2H	5.82	5.09
	Se	2H	5.49	3.70
	Te	2H	5.26	3.26
Ni	S	1T	3.36	8.62
	Se	1T	2.97	0.79
	Te	2H	0.45	3.03
Sc	S	2H	1.16	0.75
	Se	2H	1.39	0.96
	Te	2H	0.78	2.81
Ti	S	1T	2.07	9.32
	Se	2H	2.11	3.16
	Te	2H	2.10	6.05
V	S	1T	1.29	0.86
	Se	2H	5.18	1.68
	Te	2H	4.25	0.79

W	S	2H	7.39	5.14
	Se	2H	7.90	5.05
	Te	2H	6.10	4.21

Phonon Property Screening

A thorough understanding of heat transfer is important for device design. In particular, 2D TMDs have attracted much interest in this regard for the unique transport of thermal energy at the low dimension. Developing high-performance thermoelectric materials, for example, requires a large ZT which is dependent upon having low thermal conductivity. Thermal conductivity calculations involve a detailed investigation of the Boltzmann transport equation, namely second- and third-order solutions to account for both normal and Umklapp phonon modes. Here, we focus primarily on phonon DoS calculations as a means of qualitatively comparing phonon properties for 2D TMDs in order to identify trends. Figure 5.3 shows the projected phonon DoS calculation results for the MS_2 system. The total phonon DoS is shown with a solid black line in each case while contributions from the transition metal and sulfur atoms are represented by dot-dashed red and dashed black lines, respectively. Figure 5.3a-f lists each MS_2 in order of increasing atomic mass of the constituent transition metal. As the mass difference between transition metal and sulfur atoms (32.066 u) increases, the frequency gap between the acoustic and optical phonon bands generally increases, suggesting that, although mass difference can be beneficial for increased phonon scattering (and therefore decreased thermal conductivity), there might be an optimum mass difference before the different modes no longer scatter one another. If the mass difference is too large, the impurity (or defect) scattering term decreases. The WS_2 results, for example, have the largest mass difference (151.784 u) and consequently show the least amount of overlap

between M and S modes. Such features imply minimal phonon scattering and thus a larger thermal conductivity, κ. It has been evidenced by Gu *et al.* that WS_2 does indeed have a larger κ than that of MoS_2.[19] In addition, their results reveal a monotonically increasing lattice thermal conductivity with increasing acoustic-optical frequency bandgap. Sc, Ti, and V sulfides have negligibly small frequency gaps while Ni, Mo, and W sulfides have substantial gaps. In this regard, Sc, Ti, and V sulfides should exhibit the lowest lattice thermal conductivity.
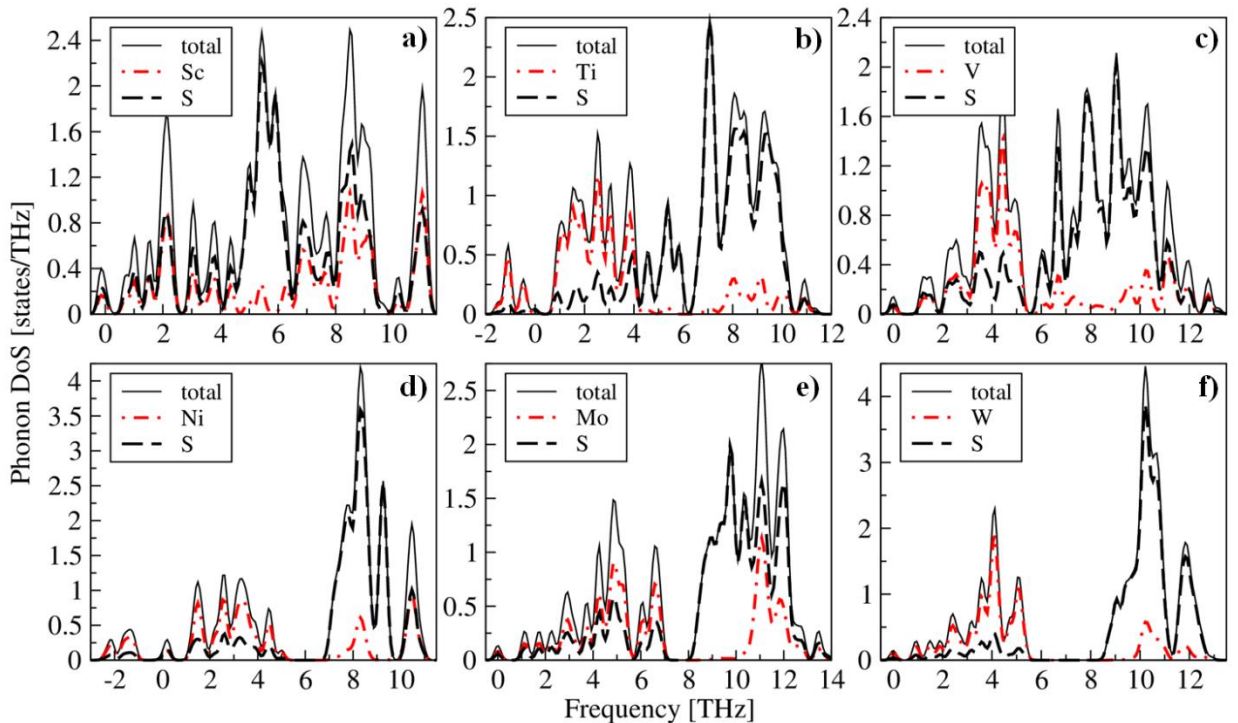
Figure 5.3. **Projected phonon DoS for each member of the MS_2 system. Each plot depicts the total phonon DoS with a solid line, the contribution from the transition metal with a dot-dashed line, and the contribution from the S atoms with a dashed line. Plots (a)-(f) are shown in order of increasing atomic mass of the transition metal as follows (a) ScS_2, (b) TiS_2, (c) VS_2, (d) NiS_2, (e) MoS_2, and (f) WS_2.**

5.4 Conclusion

A list of eighteen 2D TMD compounds, having the chemical formula MX_2 (M = Mo, Ni, Sc, Ti, V, and W; X = S, Se, Te), were chosen based on their potential stability

and on the criticality scores of the constituent transition metals. First-principles geometry, electrical property, and phonon property calculations were performed. Results were compared with features of the transition metals in order to identify predictive property trends. The atomic radius of the transition metal correlates with the 2D TMD properties. While the layer thickness of the compounds increases linearly with the transition metal radius, the lattice parameter remains constant. The electronic bandgaps of TMDs follow a Gaussian-like distribution across the range of transition metal radii wherein the smallest and largest constituent metals yield negligibly small bandgaps. In contrast, the mid-sized metals yield bandgaps of greater than 1 eV. MoX_2, TiX_2, and WX_2 compounds have the largest S. $TiTe_2$ compound exhibits bipolar conduction behavior with a noticeable S peak of about 450 to 500 μV/K for both p- and n-type calculations. The atomic mass of constituent metals also affects the compound properties. The heaviest metals, W and Mo, produce the largest n-type $S^2\sigma$. Mass difference between transition metal and sulfur atom enlarges the frequency gap between acoustic and optical phonon bands, indicating decreased phonon scattering. The Sc, Ti, and V sulfides have the smallest mass differences and the largest interaction between the metal and sulfur contributions to phonon DoS, so they should exhibit a lower lattice thermal conductivity than the other MX_2 compounds. Our work provides a new approach to draw correlations between physical properties of constituent transition metals and resultant 2D TMDs.

Expanding on the methodology from the skutterudite work in Chapter Four, this chapter explored the calculation of semi-classic transport coefficients as another metric for investigating electrical properties. The method of calculating $S^2\sigma$ and S was employed in Chapters Six to further study dopant effects.

Acknowledgements

References

(1)   Ogawa, S. Magnetic-Properties of 3d Transition-Metal Dichalcogenides with the Pyrite Structure. *J Appl Phys* **1979**, *50*, 2308.

(2)   Shishidou, T.; Freeman, A. J.; Asahi, R. Effect of GGA on the half-metallicity of the itinerant ferromagnet CoS2. *Phys Rev B* **2001**, *64*, 180401.

(3)   Tributsch, H. Solar Energy-Assisted Electrochemical Splitting of Water. *Z Naturforsch A* **1977**, *32*, 972.

(4)   Coleman, J. N.; Lotya, M.; O'Neill, A.; Bergin, S. D.; King, P. J.; Khan, U.; Young, K.; Gaucher, A.; De, S.; Smith, R. J.; Shvets, I. V.; Arora, S. K.; Stanton, G.; Kim, H. Y.; Lee, K.; Kim, G. T.; Duesberg, G. S.; Hallam, T.; Boland, J. J.; Wang, J. J.; Donegan, J. F.; Grunlan, J. C.; Moriarty, G.; Shmeliov, A.; Nicholls, R. J.; Perkins, J. M.; Grieveson, E. M.; Theuwissen, K.; McComb, D. W.; Nellist, P. D.; Nicolosi, V. Two-Dimensional Nanosheets Produced by Liquid Exfoliation of Layered Materials. *Science* **2011**, *331*, 568.

(5)   Ataca, C.; Sahin, H.; Ciraci, S. Stable, Single-Layer MX2 Transition-Metal Oxides and Dichalcogenides in a Honeycomb-Like Structure. *Journal of Physical Chemistry C* **2012**, *116*, 8983.

(6)   Rasmussen, F. A.; Thygesen, K. S. Computational 2D Materials Database: Electronic Structure of Transition-Metal Dichalcogenides and Oxides. *Journal of Physical Chemistry C* **2015**, *119*, 13169.

(7)   Butler, S. Z.; Hollen, S. M.; Cao, L. Y.; Cui, Y.; Gupta, J. A.; Gutierrez, H. R.; Heinz, T. F.; Hong, S. S.; Huang, J. X.; Ismach, A. F.; Johnston-Halperin, E.; Kuno, M.; Plashnitsa, V. V.; Robinson, R. D.; Ruoff, R. S.; Salahuddin, S.; Shan, J.; Shi, L.; Spencer, M. G.; Terrones, M.; Windl, W.; Goldberger, J. E. Progress, Challenges, and Opportunities in Two-Dimensional Materials Beyond Graphene. *Acs Nano* **2013**, *7*, 2898.

(8)   McDonnell, S.; Addou, R.; Buie, C.; Wallace, R. M.; Hinkle, C. L. Defect-Dominated Doping and Contact Resistance in MoS2. *Acs Nano* **2014**, *8*, 2880.

(9)   Gong, C.; Colombo, L.; Wallace, R. M.; Cho, K. The Unusual Mechanism of Partial Fermi Level Pinning at Metal-MoS2 Interfaces. *Nano Lett* **2014**, *14*, 1714.

(10)   Ganatra, R.; Zhang, Q. Few-Layer MoS2: A Promising Layered Semiconductor. *Acs Nano* **2014**, *8*, 4074.

(11)   Radisavljevic, B.; Radenovic, A.; Brivio, J.; Giacometti, V.; Kis, A. Single-layer MoS2 transistors. *Nat Nanotechnol* **2011**, *6*, 147.

(12)   Lopez-Sanchez, O.; Lembke, D.; Kayci, M.; Radenovic, A.; Kis, A. Ultrasensitive photodetectors based on monolayer MoS2. *Nat Nanotechnol* **2013**, *8*, 497.

(13)   Baugher, B. W. H.; Churchill, H. O. H.; Yang, Y. F.; Jarillo-Herrero, P. Optoelectronic devices based on electrically tunable p-n diodes in a monolayer dichalcogenide. *Nat Nanotechnol* **2014**, *9*, 262.

(14)   Chen, W.; Santos, E. J. G.; Zhu, W. G.; Kaxiras, E.; Zhang, Z. Y. Tuning the Electronic and Chemical Properties of Monolayer MoS2 Adsorbed on Transition Metal Substrates. *Nano Lett* **2013**, *13*, 509.

(15)   Jaramillo, T. F.; Jorgensen, K. P.; Bonde, J.; Nielsen, J. H.; Horch, S.; Chorkendorff, I. Identification of active edge sites for electrochemical H-2 evolution from MoS2 nanocatalysts. *Science* **2007**, *317*, 100.

(16)   Huang, W.; Da, H. X.; Liang, G. C. Thermoelectric performance of MX2 (M = Mo, W; X = S, Se) monolayers. *J Appl Phys* **2013**, *113*, 104304.

(17)   Huang, W.; Luo, X.; Gan, C. K.; Quek, S. Y.; Liang, G. C. Theoretical study of thermoelectric properties of few-layer MoS2 and WSe2. *Physical Chemistry Chemical Physics* **2014**, *16*, 10866.

(18)   Lee, C.; Hong, J.; Whangbo, M. H.; Shim, J. H. Enhancing the Thermoelectric Properties of Layered Transition-Metal Dichalcogenides 2H-MQ(2) (M = Mo, W; Q = S, Se, Te) by Layer Mixing: Density Functional Investigation. *Chem Mater* **2013**, *25*, 3745.

(19)   Gu, X. K.; Yang, R. G. Phonon transport in single-layer transition metal dichalcogenides: A first-principles study. *Appl Phys Lett* **2014**, *105*, 131903.

(20)   Nolas, G. S.; Slack, G. A. Thermoelectric clathrates. *Am Sci* **2001**, *89*, 136.

(21)   Zou, M. M.; Li, J. F.; Kita, T. Thermoelectric properties of fine-grained FeVSb half-Heusler alloys tuned to p-type by substituting vanadium with titanium. *Journal of Solid State Chemistry* **2013**, *198*, 125.

(22)   Dyck, J. S.; Chen, W. D.; Uher, C.; Chen, L.; Tang, X. F.; Hirai, T. Thermoelectric properties of the n-type filled skutterudite Ba0.3Co4Sb12 doped with Ni. *J Appl Phys* **2002**, *91*, 3698.

(23)   Yang, J.; Zhang, W.; Bai, S. Q.; Mei, Z.; Chen, L. D. Dual-frequency resonant phonon scattering in BaxRyCo4Sb12 (R=La, Ce, and Sr). *Appl Phys Lett* **2007**, *90*, 192111.

(24)   Williamson, I.; Her, L. J. Y.; Su, X. L.; Yan, Y. G.; Wong-Ng, W.; Li, L. Improved thermoelectric performance of (Fe,Co)Sb-3-type skutterudites from first-principles. *J Appl Phys* **2016**, *119*, 055101.

(25)   Tan, G. J.; Wang, S. Y.; Li, H.; Yan, Y. G.; Tang, X. F. Enhanced thermoelectric performance in zinc substituted p-type filled skutterudites CeFe4-xZnxSb12. *Journal of Solid State Chemistry* **2012**, *187*, 316.

(26)   Hicks, L. D.; Dresselhaus, M. S. Effect of Quantum-Well Structures on the Thermoelectric Figure of Merit. *Phys Rev B* **1993**, *47*, 12727.

(27)   Hicks, L. D.; Dresselhaus, M. S. Thermoelectric Figure of Merit of a One-Dimensional Conductor. *Phys Rev B* **1993**, *47*, 16631.

(28)   Mahan, G. D.; Sofo, J. O. The best thermoelectric. *P Natl Acad Sci USA* **1996**, *93*, 7436.

(29)   Hochbaum, A. I.; Chen, R. K.; Delgado, R. D.; Liang, W. J.; Garnett, E. C.; Najarian, M.; Majumdar, A.; Yang, P. D. Enhanced thermoelectric performance of rough silicon nanowires. *Nature* **2008**, *451*, 163.

(30)   Boukai, A. I.; Bunimovich, Y.; Tahir-Kheli, J.; Yu, J. K.; Goddard, W. A.; Heath, J. R. Silicon nanowires as efficient thermoelectric materials. *Nature* **2008**, *451*, 168.

(31)   Graedel, T. E.; Harper, E. M.; Nassar, N. T.; Nuss, P.; Reck, B. K. Criticality of metals and metalloids. *P Natl Acad Sci USA* **2015**, *112*, 4257.

(32)   Blöchl, P. E. Projector augmented-wave method. *Phys Rev B* **1994**, *50*, 17953.

(33)   Kresse, G.; Joubert, D. From ultrasoft pseudopotentials to the projector augmented-wave method. *Phys Rev B* **1999**, *59*, 1758.

(34)   Kresse, G.; Furthmuller, J. Efficient iterative schemes for ab initio total-energy calculations using a plane-wave basis set. *Phys Rev B* **1996**, *54*, 11169.

(35)   Perdew, J. P.; Burke, K.; Ernzerhof, M. Generalized gradient approximation made simple. *Phys Rev Lett* **1996**, *77*, 3865.

(36)   Liechtenstein, A. I.; Anisimov, V. I.; Zaanen, J. Density-functional theory and strong interactions: Orbital ordering in Mott-Hubbard insulators. *Phys Rev B* **1995**, *52*, R5467.

(37)   Parlinski, K.; Li, Z. Q.; Kawazoe, Y. First-principles determination of the soft mode in cubic ZrO2. *Phys Rev Lett* **1997**, *78*, 4063.

(38)   Togo, A.; Oba, F.; Tanaka, I. First-principles calculations of the ferroelastic transition between rutile-type and CaCl(2)-type SiO(2) at high pressures. *Phys Rev B* **2008**, *78*, 134106.

(39)   Grimme, S. Semiempirical GGA-type density functional constructed with a long-range dispersion correction. *J Comput Chem* **2006**, *27*, 1787.

(40)   Boker, T.; Severin, R.; Muller, A.; Janowitz, C.; Manzke, R.; Voss, D.; Kruger, P.; Mazur, A.; Pollmann, J. Band structure of MoS2, MoSe2, and alpha-MoTe2: Angle-resolved photoelectron spectroscopy and ab initio calculations. *Phys Rev B* **2001**, *64*, 235305.

(41)   Mak, K. F.; Lee, C.; Hone, J.; Shan, J.; Heinz, T. F. Atomically Thin MoS2: A New Direct-Gap Semiconductor. *Phys Rev Lett* **2010**, *105*, 136805.

(42)   Sansonetti, J. E.; Martin, W. C.; July 1, 2009 ed.; National Institute of Standards and Technology: http://www.nist.gov/pml/data/handbook/, 2014.

(43)   Shannon, R. D. Revised Effective Ionic-Radii and Systematic Studies of Interatomic Distances in Halides and Chalcogenides. *Acta Crystallogr A* **1976**, *32*, 751.

(44)   Madsen, G. K. H.; Singh, D. J. BoltzTraP. A code for calculating band-structure dependent quantities. *Computer Physics Communications* **2006**, *175*, 67.

(45)   Wang, Y.; Chen, X.; Cui, T.; Niu, Y. L.; Wang, Y. C.; Wang, M.; Ma, Y. M.; Zou, G. T. Enhanced thermoelectric performance of PbTe within the orthorhombic Pnma phase. *Phys Rev B: Condens. Matter Mater. Phys.* **2007**, *76*, 155127.

(46)   Wang, C.; Wang, Y. X.; Zhang, G. B.; Peng, C. X. Electronic Structure and Thermoelectric Properties of ZnO Single-Walled Nanotubes and Nanowires. *Journal of Physical Chemistry C* **2013**, *117*, 21037.

(47)   Kaasbjerg, K.; Thygesen, K. S.; Jacobsen, K. W. Phonon-limited mobility in n-type single-layer MoS2 from first principles. *Phys Rev B* **2012**, *85*, 115317.

CHAPTER SIX: IMPROVEMENT OF 2D TMD MATERIALS THROUGH METAL-

SITE SUBSTITUTIONAL DOPANTS*

This chapter is comprised of two works: the first is published by Elsevier in the *Chemical Physics Letters* and the second is submitted for publication in the *Journal of Applied Physics*. These works should be referenced appropriately.

References:

I. Williamson, S. Li, A. Correa Hernandez, M. Lawson, Y. Chen, L. Li, "Structural, electrical, phonon, and optical properties of Ti- and V-doped two-dimensional MoS_2." *Chemical Physics Letters*. **674** 157 (2017).

Reproduced by permission of Elsevier and hosted on Science Direct at <http://www.sciencedirect.com/science/article/pii/S0009261417301707>.

I. Williamson, N. Wilson, M. Lawson, S. Li, Y. Chen, L. Li, "Computational screening of metal-site dopants in two-dimensional MX_2 (M = Mo, W; X = S, Se, Te)." *Journal of Applied Physics*. submitted (2017).

*This chapter includes modifications from the originally published versions. Optical properties calculations that were included in both works (contributed by Shasha Li and Dr. Yue Chen at The University of Hong Kong) have been omitted from this dissertation.

Structural, electrical, phonon, and optical properties of Ti- and V-doped two-dimensional MoS₂

Izaak Williamson[a]

Shasha Li[b]

Andres Correa Hernandez[a]

Matthew Lawson[a]

Yue Chen[b]

Lan Li[a,c]

[a]Micron School of Materials Science and Engineering, Boise State University,

Boise, ID 83725.

[b]Department of Mechanical Engineering, The University of Hong Kong, Pokfulam Road,

Hong Kong SAR, China.

[c]Center for Advanced Energy Studies,

Idaho Falls, ID 83401.

Computational screening of metal-site dopants in two-dimensional MX₂ (M = Mo, W; X = S, Se, Te)

Izaak Williamson[a]

Nate Wilson[b]

Matthew Lawson[a]

Shasha Li[c]

Yue Chen[c]

Lan Li[a,d]

[a]*Micron School of Materials Science and Engineering, Boise State University,*

Boise, ID 83725.

[b]*Department of Chemical Engineering and Materials Science, University of Minnesota,*

Minneapolis, MN 55455.

[c]*Department of Mechanical Engineering, The University of Hong Kong,*

Hong Kong SAR, China.

[d]*Center for Advanced Energy Studies,*

Idaho Falls, ID 83401.

Abstract

2D TMDs, having the chemical formula MX_2 (M = transition metal, X = chalcogen), have received a lot of attention recently for their unique properties and potential for materials-by-design applications. Having notable electrical, magnetic, optical, and thermoelectric properties, 2D TMDs can be further tuned through the implementation of substitutional dopants. This work utilizes first-principles DFT calculations to explore the effects of metal-site dopant concentration and type on structural, energetic, electrical, transport, and phonon properties. These effects decrease with concentration until they converge at a dopant concentration of 2.083 at.%, where the dopants are effectively isolated. Electronic bandgap calculations reveal W-doped MoX_2 and Mo-doped WX_2 to be among the only observed semiconductors while Boltzmann transport properties confirm that these six structures have the largest power factors. This work offers an extensive investigation of metal-site dopants and how their concentration and type impact 2D TMD materials, identifying factors for tailoring their performance.

6.1 Introduction

There are a variety of potential uses for transition metal dichalcogenides (TMDs) stemming from their unique and tunable properties. Recently, these materials have attracted much interest due to novel magnetic,[1,2] electrical,[3-7] thermoelectric,[8-11] and optical[7,12-14] properties. The structure of a TMD is a large contributor to the material's versatility and wide range of interesting properties. The chemical formula is MX_2 where M is a transition metal and X is a chalcogen. The structure is composed of offset stacked layers where each layer is made up of M atoms sandwiched between two X sheets. For the 2H-type MX_2 system, it is arranged such that D_{6h} point group symmetry exists about

the M atoms. The layers are held together through strong covalent bonds while the forces between the layers are much weaker van der Waals interactions, much like that of graphite and graphene. Through mechanical exfoliation,[15] the layers can be separated into few-layer or single-layer structures. These nanostructures offer even more interesting opportunities for materials-by-design exploration.

A large advantage for two-dimensional (2D) MX_2 structures comes from the reduced dimensionality which can extend the limitations of bulk TMD properties. In field-effect transistors (FETs), for example, the smaller device features have greatly reduced short-channel effects, reduced switching voltage, and increased the on-off ratio.[5,12] Another example of significant changes in the electronic structure comes in the case of MoS_2 which undergoes a transition from having an indirect bandgap of 1.2 eV in bulk[16] to a direct bandgap of 1.8 eV in 2D.[17] This effect is useful for electronic and optoelectronic applications.[18] Under the photoexcitation condition, the direct bandgap semiconductor would have a high absorption coefficient and efficient electron–hole pair generation, suggesting promising application as photonic and optoelectronic devices. For example, photoluminescence has been found to increase with decreasing thickness of MoS_2,[19] and the luminescence quantum efficiency of a freestanding monolayer is four orders of magnitude stronger than in its bulk counterpart.[17] The 2D MoS_2 was also reported as ultrasensitive phototransistors because of the improved device mobility and on current.[13] Furthermore, the photoresponsivity of 2D MoS_2 phototransistors was found to exceed that of a graphene-based device.[20] Additionally, the quantum confinement effect at lower dimensionalities enhances thermoelectric properties by increasing the Seebeck coefficient, S, (the measure of a material's voltage response to temperature

change) where the thermoelectric performance is determined using the figure of merit, *ZT* (see Equation 2.1).[21-23]. Another factor that contributes to thermoelectric enhancement in 2D materials is the increase in power factor, $S^2\sigma$, due to the change in shape of the density of modes (DoM).[24,25] Through increased diffusive boundary scattering, it is expected that the thermal conductivity could decrease, further enhancing thermoelectric properties.[26,27] Such a large potential for properties and transport behavior emphasizes the need to fully understand 2D MX_2 materials.

A number of screening methods have been implemented through first-principles density functional theory (DFT) calculations in order to identify more favorable MX_2 compositions and potentially highlight a narrower list of promising candidates. The works of Ataca *et al.*[3] and Rasmussen *et al.*[4] have explored various compositions, focusing on stability, electrical, and optical properties. Our previous work[28] combined these findings with transition metal "criticality scores"[29] in order to highlight the environmental impact and materials availability as well as the more stable and promising compositions. Our narrowed list of eighteen 2D MX_2 structures (M = Mo, Ni, Sc, Ti, V, and W; X = S, Se, and Te) was then investigated for structural, electrical, and phonon property effects. This identified trends in the structure-property relationship which can lead to the identification of novel compositions and facilitate materials design.

Further property improvements and tuning can be achieved through the use of metal-site substitutional dopants which yield interesting changes in the intrinsic properties of 2D TMDs. These dopants can cause enhancements such as inducing magnetism[30-33] and tuning of the electrical conductivity.[33] They also offer the ability to modify the bandgap and photoluminescence[34] and control whether it is a *p*- or *n*-type

semiconductor.[35] Previous work has shown that these dopants are stable in 2D TMDs and that they are a substitutional dopant rather than an interstitial impurity.[36-39] This type of defect tends to be more stable because the dopant inherits the strong covalent bonds within the TMD sheet.

In this work, we investigate the effect of dopant concentration and type in 2D TMD materials. We investigated substitutional Ti dopants on Mo sites in 2D MoS_2 at concentrations of 0.926, 1.333, 2.083, 3.704, and 8.333 at.% Ti (or 2.78, 4.0, 6.25, 11.11, and 25.0 Mo-site % Ti) to determine its effect on various properties. Next, six different transition metals (M' = Mo, Ni, Sc, Ti, V, and W) were incorporated at the metal-site in MoX_2 and WX_2 (X = S, Se, or Te), according to the chemical formula $M'M_{15}X_{32}$. These six were chosen based on the screening criteria of previous work.[28] The structural, energetic, electrical, transport, and phonon properties were analyzed with respect to the physical features of the dopant atoms (*e.g.*, atomic radius, preferred oxidation state) to better understand the doping effects of these 2D TMD structures. This approach offers a means of extensively analyzing the effects of dopant concentration and type in MoX_2 and WX_2 to identify key factors in improving novel 2D TMD materials.

6.2 Computational Methods

All calculations were performed within DFT implemented via the VASP code.[40] The PBE formalism was employed with spin-polarized GGA.[41] PAW pseudopotentials were used to expand the plane-wave basis set to a cutoff energy of 500 eV.[42,43] For the Brillouin zone integration, a Γ-centered 12x12x1 mesh was used for the 2x2x1 supercell (corresponding to 8.333 at.% Ti). All other structures used *k*-point meshes proportional to this depending on their supercell size (rounded to the nearest integer). Fermi surface

broadening was handled using a Gaussian smearing of 0.05 eV. Geometries were relaxed until residual forces were reduced to 0.01 eV/Å. To minimize interlayer interaction, MX_2 single-layer sheets in the neighboring cells were separated by a distance of at least 20 Å.

Electronic structure calculations were performed with denser k-point meshes (doubled in x and y directions with respect to the geometry optimization calculations). For the systems with dopant concentrations of 2.083 at.% ($M'Mo_{15}S_{32}$), a denser 24x24x1 k-point mesh was used. The DFT+U scheme[44] was also implemented to account for strong correlation effects of the transition metals. Convergence-tested values for the on-site Coulomb potentials of U = 4.38, 8.0, 3.0, 8.0, 6.0, and 8.0 eV were used for Mo, Ni, Sc, Ti, V, and W, respectively while an on-site exchange potential of J = 1.0 eV was used for all metals. The resulting band energies were used to calculate semi-classic transport coefficients using the BoltzTraP software package.[45]

Phonon structure calculations were performed following the method of Parlinski-Li-Kawazoe where second-order force constants were determined using DFPT.[46,47] Convergence tests indicated that long-range phonon effects were adequately accounted for by means of the following supercells: 3x3x1, 3x3x1, 2x2x1, and 2x2x1 for the dopant concentrations of 0, 8.333, 3.704, and 2.083 at.%, respectively. The 1.333 and 0.926 at.% systems were found to be sufficiently large to contain long-range effects without the need of further supercell sizes. The k-point meshes were likewise adjusted based on supercell sizes for the systems.

Error mitigation was handled for the DFT input parameters through convergence tests similar to those performed in Sections 4.2 and 5.2. The supercell sizes were chosen to represent various dopant concentrations and their affects are discussed in the following

section. Unlike Sections 4.2 and 5.2, the work of metal-site substitution is relatively new

and there were no literature values to compare with at the time the work was conducted.

The structures in this chapter initially came from the pure 2D TMD screening work in

Chapter Five. The error handling in Section 5.2 helped minimize errors in this chapter.

6.3 Results

<u>Structure</u>

<u>Dopant Concentration</u>

In order to determine the substitution concentration effect, we incorporated Ti

substitution with 8.333 at.% Ti (*i.e.*, $Ti_1Mo_3S_8$), 3.704 at.% Ti ($Ti_1Mo_8S_{18}$), 2.083 at.% Ti

($Ti_1Mo_{15}S_{32}$), 1.333 at.% Ti ($Ti_1Mo_{24}S_{50}$), and 0.926 at.% Ti ($Ti_1Mo_{35}S_{72}$). The presence

of Ti dopants in 2D MoS_2 causes minimal structure distortion. An example of the doped

2D TMD structure is depicted in Figure 6.1.
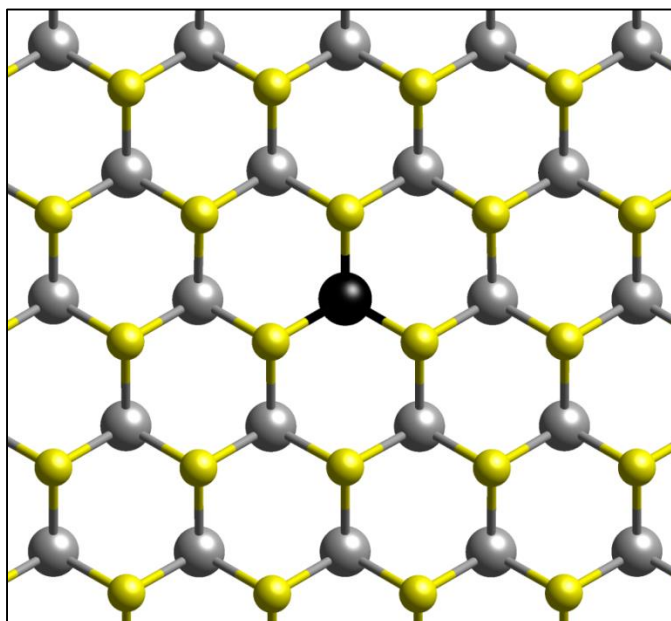
Figure 6.1.   Top-down view of M'-doped MX_2 where the M' dopant atom is depicted with a black sphere, the M atoms are gray spheres, and the X chalcogens are yellow spheres.

The value a_{uc} (shown in Table 6.1) represents the average lattice parameter with respect to the unit cell of pure 2D MoS_2 and increases with Ti concentration. This minor expansion suggests the presence of small compressive forces around the Ti dopant. To further investigate this distortion, the M-S and S-S bond lengths were also measured, given as d_{M-S} and d_{S-S}, respectively (see Figure 6.2). Note that the S-S distance value is equivalent to the sheet thickness. The superscript $^{M'}$ indicates values taken near the dopant atom, while the superscript ^{Mo} indicates those taken about the Mo atoms farthest from the dopant. For each bond distance calculated, there is less than 1% difference between any of the doped structures. The S-M-S bond angle is given as θ and its values differ by no more than 2%. As Ti concentration decreases, each of the ^{Mo} values approach that of the pure MoS_2. For instance, the d_{S-S}^{Mo} and θ^{Mo} values for the high concentration system (8.333 at.% Ti) are much smaller than pure MoS_2 values but increase with decreasing concentration until convergence is reached by 2.083 at.% Ti. Likewise, the d_{Mo-S}^{Mo} value for the high concentration system is larger than pure MoS_2 and decreases with concentration until converging at 2.083 at.% Ti. This means that for this concentration, the area between neighboring dopants is sufficiently large for the surrounding MoS_2 structure to mimic the undoped structure, effectively isolating the dopants from each other. Also, the a_{uc} and d_{Mo-S}^{Mo} values increase with Ti concentration while the d_{S-S}^{Mo} and θ^{Mo} values decrease. The expansion in the x- and y-directions and compression in the z-direction indicate anisotropic strain. This could be a result of the difference in oxidation state between the Mo and Ti metals.

Table 6.1. **Geometric structure results for pure and M'-doped (M' = Ti) 2D MoS₂. The average lattice parameter with respect to the original unit cell, a_{uc}, the M-S and S-S bond distances, d_{M-S} and d_{S-S}, S-M-S bond angles, θ, and binding energies, E_b, are given. All distances are given in angstroms (Å) and all angles are given in degrees (°). Superscripts $^{M'}$ and ^{Mo} indicate values taken at the dopant site and at the Mo site farthest from the defect, respectively.**

	at.% M'	a_{uc}	$d_{M'-S}^{M'}$	d_{Mo-S}^{Mo}	$d_{S-S}^{M'}$	d_{S-S}^{Mo}	$\theta^{M'}$	θ^{Mo}	E_b (eV)
pure MoS₂	0	3.182	--	2.413	--	3.128	--	80.81	--
Ti-doped	0.926	3.191	2.428	2.414	3.056	3.128	78.00	80.79	-7.45
	1.333	3.196	2.428	2.413	3.055	3.129	77.98	80.84	-7.45
	2.083	3.203	2.428	2.413	3.056	3.127	78.00	80.80	-7.44
	3.704	3.216	2.429	2.414	3.057	3.103	77.99	79.97	-7.31
	8.333	3.236	2.420	2.429	3.060	3.098	78.43	79.25	-6.94
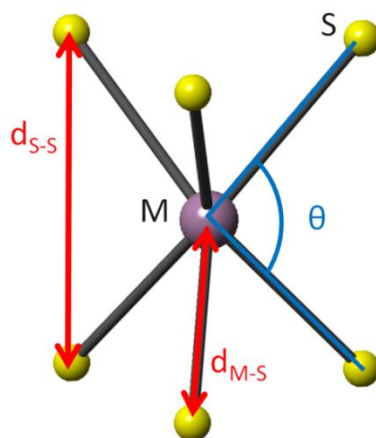
Figure 6.2. **Schematic of an MS₂ octahedron where the violet and yellow spheres represent M and S atoms, respectively. In this work, the M atom depicts either the dopant, M' (Ti or V), or the constituent, Mo. The bond lengths are represented by red arrows where d_{S-S} and d_{M-S} depict the distance between two S atoms and between the M and S atoms, respectively. The S-M-S bond angle is represented by the blue lines and the symbol θ.**

In order to compare defect stability and confirm the structure convergence for the Ti-doped system, the binding energy (E_b) was calculated according to the following equation:

$$E_b = E_{tot}^{doped} - E_{no\ M'}^{undoped} - E_{M'} \tag{6.1}$$

Here, the symbol E_{tot}^{doped} represents the total energy of the doped system, $E_{no\ M'}^{undoped}$ represents the energy of the undoped system where the dopant atom, M′, was removed, and $E_{M'}$ is the chemical potential of the dopant taken from its unary bulk structure. Our approach is similar to that of Zhou *et al.*,[30] except they also account for the strain energy associated with the dopant-MoS$_2$ bonds. Our $E_{no\ M'}^{undoped}$ term is not relaxed, so the resulting E_b only accounts for the energy associated with the M′–S bond. Furthermore, our $E_{M'}$ term is taken from the bulk M′ system rather than isolated M′. These results are given in Table 6.1. The system with the highest E_b (*i.e.*, the least negative value) is the least stable, occurring at the highest dopant concentration, 8.333 at.% Ti (E_b = -6.94 eV). As Ti concentration decreases, the E_b decreases until it converges at 2.083 at.% Ti (-7.44 eV), consistent with the structural convergence.

Dopant Type

To explore a wide range of dopant effects on 2D MoX$_2$ and 2D WX$_2$ systems, six different transition-metal-site dopants were considered: Mo, Ni, Sc, Ti, V, and W. The chemical formula for these compounds is M'M$_{15}$X$_{32}$ (M = Mo or W; X = S, Se, or Te). DFT-based structural relaxation calculations were employed to obtain ground state configurations for each doped system. Structural property results are given in Table 6.2. In most cases, the structural distortion is minimal for 2.083 at.% dopant on 2D MoX$_2$ and 2D WX$_2$. For both structures, the Ni and Sc dopants cause the largest distortions (as

much as 10.66% and 12.78% reductions in monolayer thickness (X-X bond lengths) for

Ni in $MoTe_2$ and WTe_2, respectively). These two dopants have the lowest oxidation states

of any metals investigated (+2 for Ni and +3 for Sc) and have respectively, the smallest

and largest atomic radii. The tellurides consistently exhibit larger distortions than the

other dichalcogenides. These distortions are most noticeable in the layer thickness,

corresponding to X-X bond length (d_{X-X}), and X-M-X bond angle (θ). The least distorted

structures are W-doped MoX_2 and Mo-doped WX_2. This is consistent with the fact that

Mo and W have similar atomic radii (0.79 Å and 0.80 Å, respectively) and tend to have

similar oxidation states (+6). Overall, the lattice constant, a_{uc}, experiences the least

distortion of all measured geometries ($\leq |1.00\%|$ change). This implies that differences in

layer thickness, rather than lattice mismatch, would be the primary cause for any

potential dopant instability.

Table 6.2.   **Structure properties of metal-site doped MX_2 (having the formula $M'M_{15}X_{32}$ where M' = dopant atom Mo, Ni, Sc, Ti, V, or W; M = Mo or W; and X = S, Se, or Te) compared to the undoped values. The average lattice parameter per unit cell (4x4 unit cells per structure), a_{uc}, M'-X bond length, X-X bond length, and X-M-X bond angle are given in units of either angstroms (Å) or degrees (°). The percent difference from the corresponding undoped value is listed as Δ%.**

MX_2 matrix	M' dopant	a_{uc} (avg./unitcell)		d_{M-X}		d_{X-X}		θ	
		Å	Δ%	Å	Δ%	Å	Δ%	°	Δ%
MoS_2	undoped	3.182	--	2.413	--	3.128	--	80.81	--
	Ni	3.189	0.23%	2.417	0.16%	3.078	-1.60%	79.10	-2.11%
	Sc	3.213	0.97%	2.526	4.70%	3.115	-0.40%	76.13	-5.79%
	Ti	3.203	0.66%	2.428	0.63%	3.056	-2.30%	77.99	-3.48%
	V	3.188	0.17%	2.362	-2.11%	3.043	-2.71%	80.21	-0.74%
	W	3.182	0.00%	2.409	-0.14%	3.128	0.00%	80.94	0.17%

MoSe$_2$	undoped	3.319	--	2.541	--	3.338	--	82.12	--
	Ni	3.327	0.25%	2.480	-2.41%	3.190	-4.45%	80.05	-2.52%
	Sc	3.341	0.68%	2.649	4.25%	3.375	1.11%	79.15	-3.62%
	Ti	3.329	0.33%	2.557	0.61%	3.301	-1.11%	80.42	-2.07%
	V	3.316	-0.08%	2.492	-1.93%	3.278	-1.79%	82.27	0.18%
	W	3.318	-0.01%	2.541	0.01%	3.341	0.07%	82.19	0.08%
MoTe$_2$	undoped	3.549	--	2.731	--	3.611	--	82.76	--
	Ni	3.564	0.40%	2.595	-4.99%	3.226	-10.66%	76.87	-7.12%
	Sc	3.570	0.59%	2.853	4.46%	3.653	1.17%	79.63	-3.79%
	Ti	3.556	0.18%	2.757	0.94%	3.599	-0.34%	81.49	-1.53%
	V	3.549	-0.02%	2.693	-1.41%	3.547	-1.78%	82.39	-0.45%
	W	3.550	0.01%	2.734	0.12%	3.614	0.08%	82.72	-0.05%
WS$_2$	undoped	3.181	--	2.416	--	3.139	--	81.03	--
	Mo	3.182	0.02%	2.420	0.14%	3.138	-0.06%	80.84	-0.24%
	Ni	3.191	0.30%	2.419	0.13%	3.075	-2.06%	78.92	-2.61%
	Sc	3.213	1.00%	2.525	4.49%	3.114	-0.81%	76.16	-6.02%
	Ti	3.202	0.64%	2.432	0.65%	3.066	-2.35%	78.15	-3.56%
	V	3.186	0.15%	2.369	-1.94%	3.058	-2.60%	80.37	-0.82%
WSe$_2$	undoped	3.317	--	2.546	--	3.355	--	82.43	--
	Mo	3.316	-0.01%	2.545	-0.02%	3.351	-0.13%	82.33	-0.13%
	Ni	3.326	0.27%	2.528	-0.68%	3.258	-2.89%	80.22	-2.69%
	Sc	3.348	0.94%	2.649	4.04%	3.326	-0.85%	77.80	-5.62%
	Ti	3.329	0.36%	2.559	0.51%	3.304	-1.50%	80.44	-2.42%
	V	3.315	-0.07%	2.497	-1.93%	3.290	-1.93%	82.43	0.00%

	undoped	3.552	--	2.736	--	3.623	--	82.91	--
	Mo	3.552	0.00%	2.732	-0.13%	3.618	-0.13%	82.91	0.01%
	Ni	3.566	0.39%	2.592	-5.26%	3.160	-12.78%	75.10	-9.42%
WTe$_2$	Sc	3.578	0.74%	2.848	4.08%	3.608	-0.41%	78.61	-5.18%
	Ti	3.561	0.25%	2.755	0.69%	3.567	-1.53%	80.69	-2.67%
	V	3.551	-0.01%	2.693	-1.58%	3.541	-2.24%	82.23	-0.82%

The resulting E_b values for each of the doped 2D MoX$_2$ and 2D WX$_2$ systems, given in Figure 6.3, are depicted graphically versus the dopant atom. The dopant atoms are listed in order of increasing atomic radius. Here we can see that the Ni dopant has the least negative binding energy among all systems (ranging from -1.60 eV in WTe$_2$ to -2.50 eV in MoS$_2$), indicating that it is the least stable dopant observed. This could be due to a number of factors including: Ni is the only magnetic dopant investigated, it has the lowest average oxidation state (+2), and it has the smallest atomic radius (0.62 Å). Alternatively, the Sc and Ti dopants consistently exhibit among the most negative binding energies, suggesting good stability in each system. These values range from -4.58 eV (Sc) and -4.37 eV (Ti) in both telluride systems to -6.98 eV (Sc) and -7.44 eV (Ti) in MoS$_2$. This is in contrast to the fact that the Sc-doped systems have among the largest distortions, suggesting that atomic radius of the dopants plays a larger role in its stability than the oxidation state. All dopants in MoS$_2$, except Ni, have large negative binding energies (around -7 eV) suggesting high stability. However, the dopants show noticeably decreasing stability with increasing chalcogen atomic number. Also, the difference in binding energy between the MoX$_2$ and WX$_2$ systems is less than 1 eV. The largest difference is 0.86 eV, occurring between the V-doped MSe$_2$ systems.
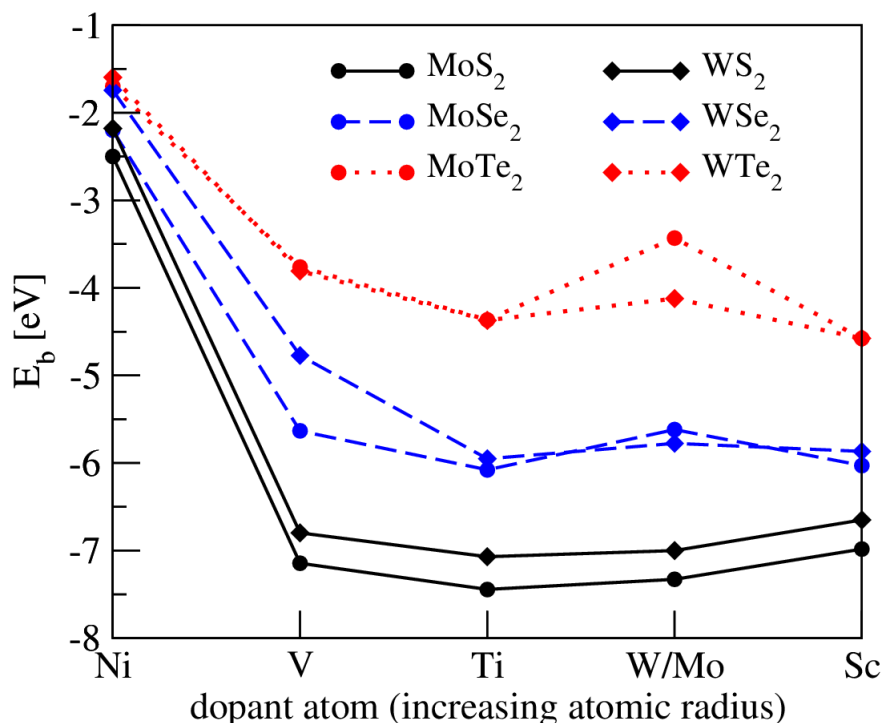
Figure 6.3.   Dopant atom binding energy (E_b) for each system listed in order of increasing dopant atomic radius. Solid black, dashed blue, and dotted red lines represent MS$_2$, MSe$_2$, and MTe$_2$ systems, respectively. Circle-lines depict MoX$_2$ structures while diamond-lines depict WX$_2$ structures. More-negative E_b values (greater absolute values) correspond to greater stability.

Electrical Properties

The incorporation of Ti dopants has a significant impact on the electrical properties of 2D MoS$_2$. Figure 6.4 depicts the electronic density of states (DoS) for pure MoS$_2$ (black line), plotted against the DoS for Ti-doped MoS$_2$ (colored lines). In each case, Ti dopants decrease the conduction band minimum (CBM) – although not by much for the case with largest Ti concentration – and introduces a mid-gap peak just above the Fermi level (E_F) making the system behave as a p-type semiconductor. The DoS plots also converge as Ti concentration decreases. Each of the three relatively low concentrations (0.926, 1.333, and 2.083 at.% Ti) have very similar results, implying that dopant concentrations at or below 2.083 at.% Ti exhibit similar electronic behavior. This result is consistent with what we found in the structural results. The lowest concentration

of Ti (0.926 at.% Ti) has a negligible DoS at E_F, yet as Ti concentration increases, this

value increases until 3.704 at.% Ti when the mid-gap peak has essentially blended into

the valence band. These results could suggest an increase in electrical conductivity for the

Ti-doped system when compared to the pure. The system with the highest Ti

concentration (8.333 at.% Ti) deviates the most from the pure 2D MoS$_2$ data and has a

valence band maximum (VBM) that extends well beyond E_F. With such a high

concentration, the dopant-dopant separation is only about 6.47 Å and the Ti is more of a

constituent atom than a dopant.
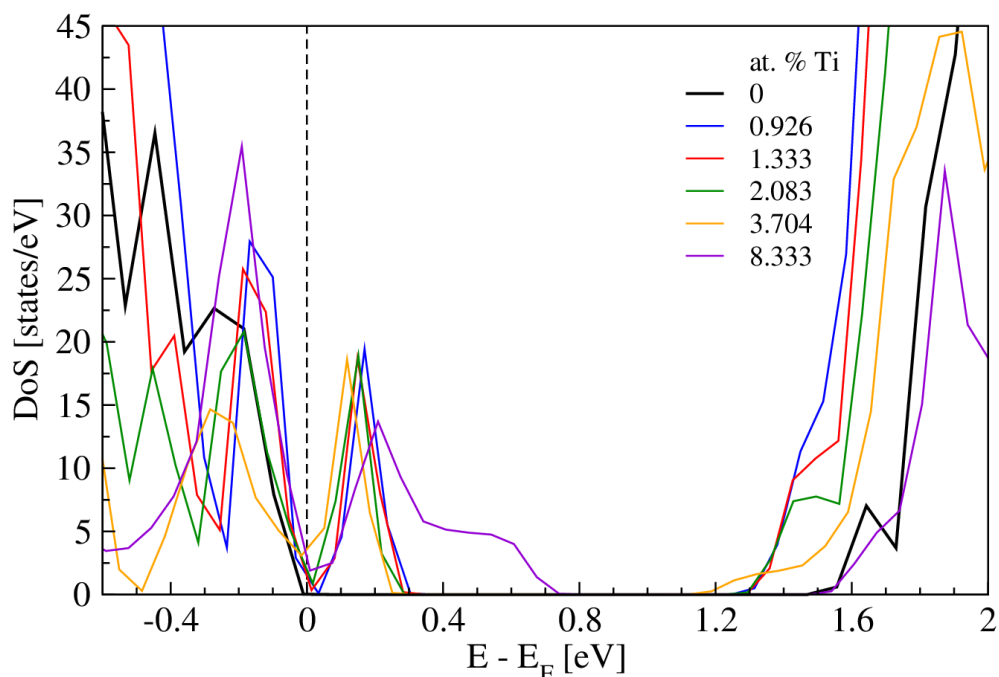
Figure 6.4. **Electronic DoS for 2D MoS₂ having increasing atomic percentage concentrations of Ti dopants. These concentrations include 0.926 (blue), 1.333 (red), 2.083 (green), 3.704 (orange), and 8.333 (violet) at.% Ti. The pure MoS₂ data is shown for comparison and depicted with a black line. All data is shifted to align each plot's respective Fermi levels (E_F's) to $x = 0$ (represented by the vertical dashed black line). Inset focuses on the area immediately surrounding E_F.**

Similarly, the electronic structure for the V doped system was calculated for comparison. Figure 6.5 depicts the local density of states (LDoS) for the individual atomic species' contribution to the DoS. These were plotted against the DoS for pure MoS_2 (black) for comparison. Both dopants have similar effects on the DoS such as a slight reduction in the CBM position and the addition of a mid-gap peak near the VBM. The V-doped system has more DoS near E_F, but the mid-gap peak is less substantial than that of the Ti-doped system. The LDoS results show that while this peak is primarily contributed by the dopant atom for both systems, there are still significant contributions from the Mo and S atoms. This implies a change in electronic structure for the overall system. These results indicate a p-type semiconducting behavior for both dopant types but the effect will likely be more prominent for Ti.
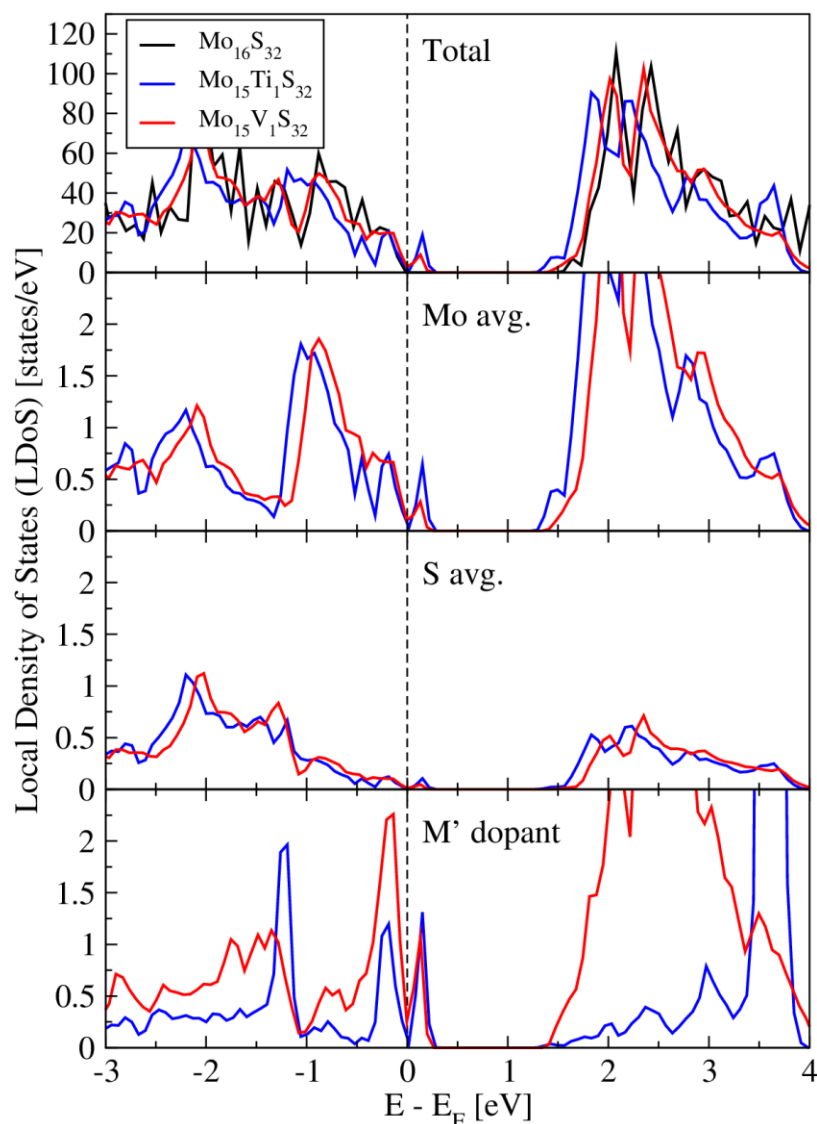
Figure 6.5. LDoS calculated as a function of electron energy (shifted to $E_F = 0$ eV) for the $Mo_{15}M'_1S_{32}$ system (2.083 at.% M' where M' = Ti or V). The black line represents pure MoS_2 while the blue and red lines depict Ti-doped and V-doped MoS_2 systems, respectively. The top plot has the total DoS for each system while the bottom three show local contributions per atom (avg.) from each of the Mo, S, and M' atoms, respectively. The vertical dashed black line indicates E_F.

The electronic structures were calculated for each doped system and compared

with that of the undoped systems. All undoped 2D MX_2 systems were found to be direct

bandgap semiconductors with gaps of 1.69, 1.84, 1.09, 1.84, 1.57, and 1.07 eV for MoS_2,

$MoSe_2$, $MoTe_2$, WS_2, WSe_2, and WTe_2, respectively. In Figure 6.6, the electronic density

of states (DoS) is plotted for each dopant in each system while the undoped DoS data is

included for comparison. For both MoX_2 and WX_2 systems, the bandgaps generally decrease with increasing chalcogen atomic number. In all cases, the presence of the transition metal dopant reduces the effective bandgaps by some amount. For some doped MoS_2 and all doped $MoSe_2$, there is a reduction in the conduction band minimum (CBM) whereas the dopants in WS_2 and WSe_2 have CBMs at or above that of the undoped structures (see Figure 6.6a - Figure 6.6d). Both telluride structures have a wide range of CBM values (see Figure 6.6e and Figure 6.6f). Most dopants also introduce mid-gap states which would increase electrical conductivity. In each system, these states are most prevalent near the top of the valence band, suggesting p-type semiconducting behavior. The Ni- and Sc-doped systems have the most mid-gap states while the Ti- and V-doped systems typically only show small mid-gap peaks. All Mo- and W-doped systems exhibit direct bandgap semiconducting behavior. In fact, with the exception of Sc-doped $MoSe_2$ (which has a small gap of about 0.14 eV), these were the only doped systems found to be semiconducting.
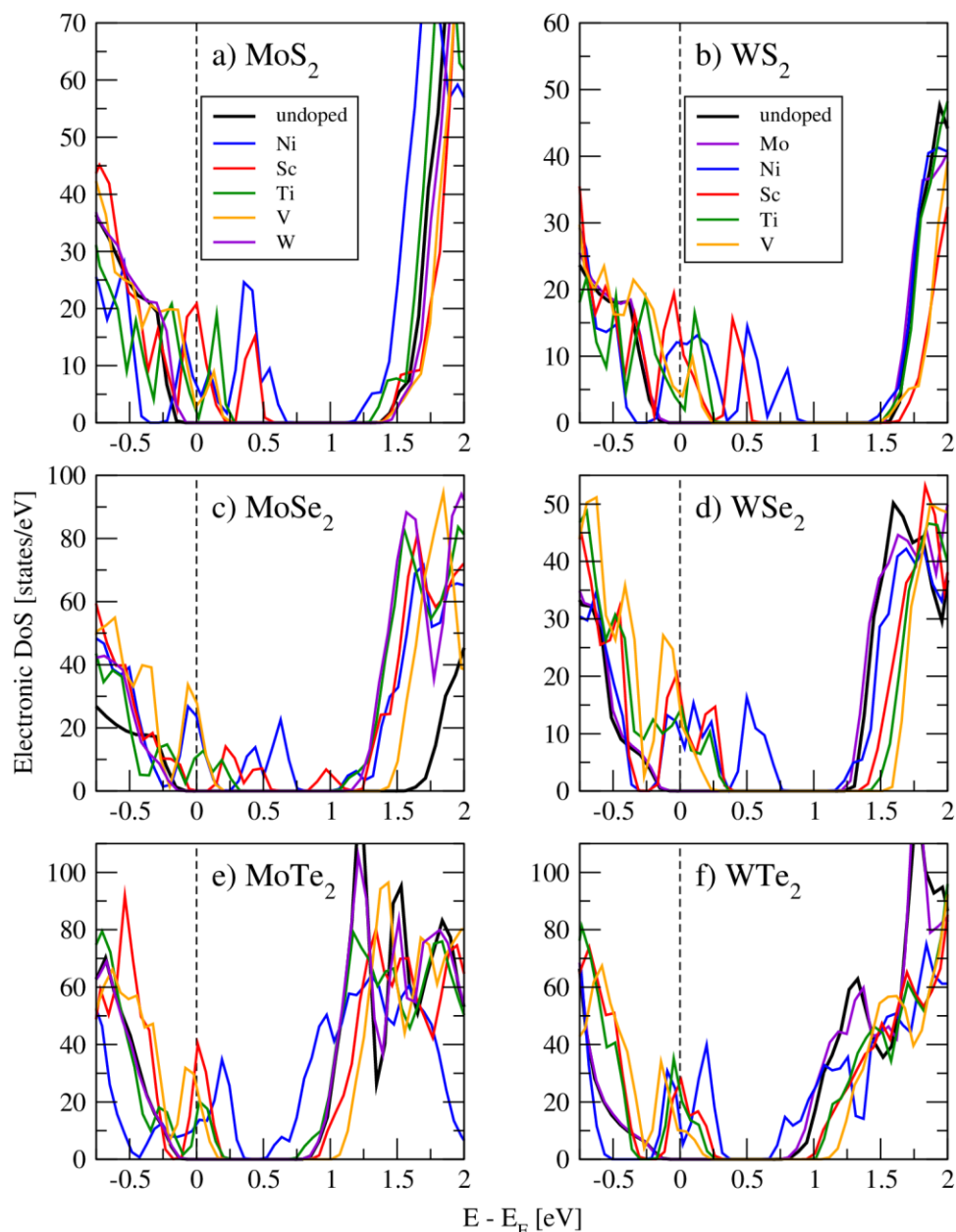
Figure 6.6. **Electronic DoS for each doped system. Column 1 (a, c, and e) contains the MoX$_2$ data while column 2 (b, d, and f) contains the WX$_2$ data. The rows depict sulfide (a and b), selenide (c and d), and telluride (e and f) systems, respectively. Undoped, Ni-, Sc-, Ti-, and V-doped systems are represented by black, blue, red, green, and orange lines, respectively. Both the W-doped systems in column 1 (a, c, and e) and the Mo-doped systems in column 2 (b, d, and f) are shown as violet lines.**

<u>Electrical Transport Properties</u>

The semi-classic transport properties were calculated by solving the Boltzmann

transport equation.[45] The resulting *p*-type *S*, electrical conductivity, σ, and power factor

$S^2\sigma$ are plotted in Figure 6.7. With the electronic density of states suggesting *p*-type

behavior, we focused these calculations on *p*-type properties as holes are likely the

majority carrier for these doped materials. For the sake of brevity, we focused on the only

doped systems to have a sizeable bandgap with no mid-gap peaks which are W-doped

MoX_2 and the Mo-doped WX_2. The difference in *S* between Mo (Figure 6.7a) and W

(Figure 6.7b) systems is small, thus they have comparable $S^2\sigma$ values (Figure 6.7e and

Figure 6.7f). The largest difference between these two systems comes from their σ values

which were found to be larger for Mo-doped WX_2 (Figure 6.7d) than for W-doped MoX_2

(Figure 6.7c). In all cases, $S^2\sigma$ is significantly reduced upon doping. This is largely due

to *S* which is reduced by as much as 15% for the MoX_2 system (Figure 6.7a) and 24% for

the WX_2 system (Figure 6.7b). In the case of the sulfides, the σ is also reduced which

leads to further reductions in *S*. For the selenides and tellurides, however, the σ of the

doped systems increases (by as much as 60% for the Mo-doped WSe_2 compound at

carrier concentration, $N = 10^{14}$ holes/cm^2) which offsets the reduction in *S*. Therefore, the

selenides and tellurides experience less of a reduction in $S^2\sigma$ upon doping than the

sulfides for these systems. The systems that experience the least reduction are W-doped

$MoSe_2$ and $MoTe_2$ which have $S^2\sigma$ values only 13% and 10% lower than undoped,

respectively.
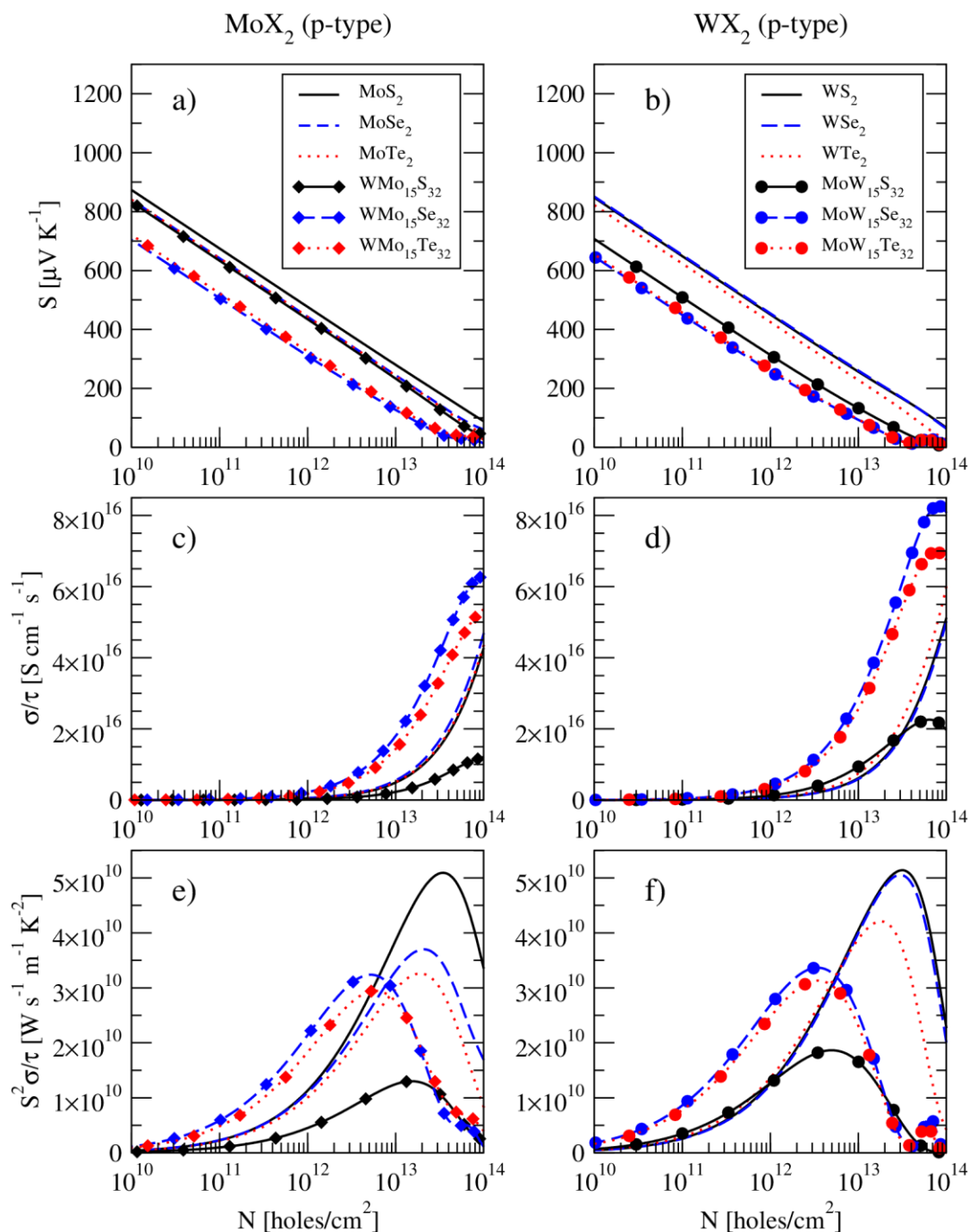
Figure 6.7. Boltzmann transport properties calculated as a function of carrier concentration, N, for W-doped MoX$_2$ (plots a, c, and e) and Mo-doped WX$_2$ (plots b, d, and f). The Seebeck coefficient, S, electrical conductivity, σ/τ, and power factor, $S^2\sigma/\tau$, are shown in rows (a-b), (c-d), and (e-f), respectively. Sulfide, selenide, and telluride systems are represented by solid black, dashed blue, and dotted red plots, respectively, while diamond-line plots and circle-line plots depict W- and Mo-doped systems, respectively.

Phonon Properties

      In semiconductors, heat conduction is typically dominated by phonon transport.

Therefore, it is necessary to investigate the effects of dopants on the phonon properties of

2D MoS_2. The phonon DoS was calculated for each of the Ti-substituted 2D MoS_2

systems and plotted in Figure 6.8. Like the geometric and electronic structure results, the

general shape, peak positions, and frequency gaps for the three lowest Ti concentrations

are similar. Each of these has a mid-gap peak, effectively reducing the gap between

acoustic and optical bands. The phonon DoS for the relatively high concentrations of Ti

(3.704 and 8.333 at.% Ti) start to deviate from that of the other systems. The reason for

that is the significant structural distortion where the dopants are not adequately isolated.

Similar to the electronic DoS results, the system with 8.333 at.% Ti deviates the most and

even has a larger frequency gap than the pure MoS_2.
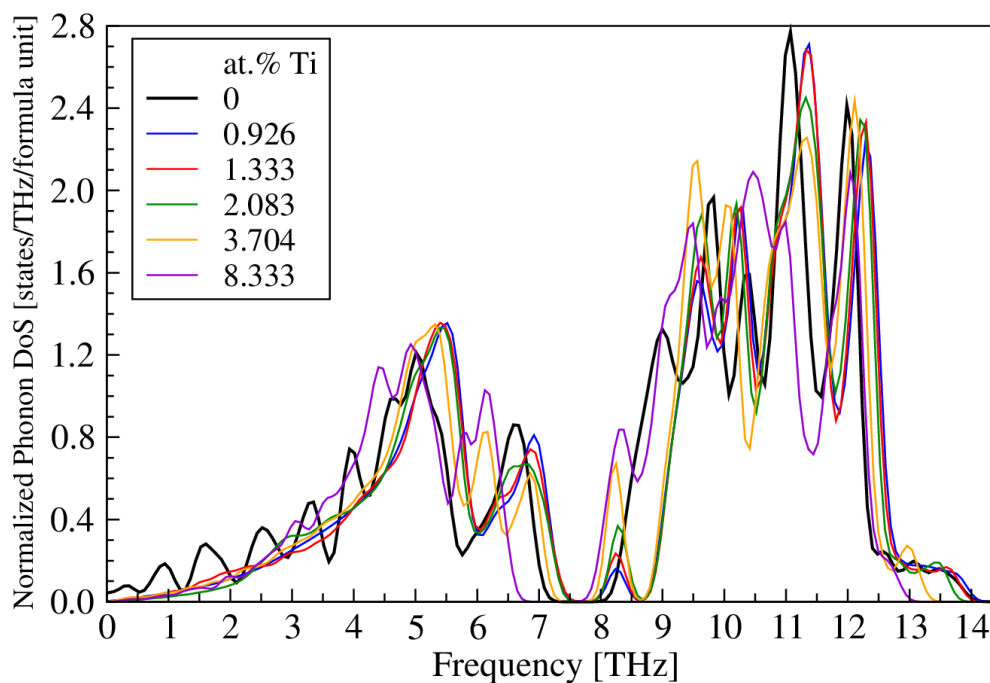
Figure 6.8.   **Phonon DoS calculated for various concentrations of Ti dopants in 2D MoS_2. Data is shown normalized per formula unit. The black line represents pure**

MoS$_2$ with 0 at.% Ti while the colored lines represent 0.926 (blue), 1.333 (red), 2.083 (green), 3.704 (orange), and 8.333 (violet) at.% Ti.

To compare the phonon properties of doped and undoped MoS$_2$, the corresponding phonon spectra are qualitatively analyzed. This approach allows the effects of these dopants to be screened without necessitating rigorous Boltzmann transport equation (BTE) calculations. The results in Figure 6.8 show three primary alterations to the MoS$_2$ phonon DoS upon Ti-doping: smoother features in the acoustic region, a reduced frequency gap, and a reduction in optical phonon mode frequency. For all concentrations of Ti, the acoustic region of the phonon DoS is smoother than that of the pure MoS$_2$ which has several peaks and deep valley-shaped curves. These peaks broaden and fill in valleys upon Ti-doping. In the work of Zhang *et al.*, they suggested that phonon mode broadening indicated a reduction in phonon lifetimes and subsequently shorter mean free paths for modes in this region.[48] The mid-gap peak causes the gap between acoustic and optical bands to decrease from 1.45 THz for pure MoS$_2$ down to 1.11 THz for 2.083 at.% Ti. Previous first-principles calculations showed a correlation between smaller frequency gaps and reduced lattice thermal conductivity, κ_l, which is attributed to an increase in both the number and strength of scattering events between acoustic and optical phonon modes.[11] Therefore, it is reasonable to assume that the presence of substitutional Ti here is likewise increasing acoustic-optical phonon scattering. Finally, in the optical band, the highest frequency modes decrease with increasing Ti concentration from about 14.3 THz (at 0, 0.926, and 1.333 at.% Ti) down to about 13.1 THz (at 8.333 at.% Ti). This implies a lower dispersion gradient and therefore lower phonon group velocities for these modes. These alterations to the phonon

properties of 2D MoS$_2$ indicate potential alterations to phonon transport in the material due to Ti doping.

The phonon DoS was also calculated for the V-doped system in comparison with the Ti-doped system (see Figure 6.9). The acoustic band region is smooth for both substitutions, implying an increase in phonon-phonon interaction. However, the optical band is not shifted to the lower frequencies as in the Ti case. The most significant difference between the Ti- and V-doped phonon DoS results is in the mid-gap peak which is shifted to higher frequencies for the V case. This shift causes the V-doped system to have effectively the same frequency gap (1.43 THz) as that of the pure MoS$_2$ (1.45 THz). Therefore, it might be expected that V dopants do not increase acoustic-optical phonon scattering in 2D MoS$_2$ as greatly as the Ti dopants. However, the bond lengths about the V dopant differ from that of both the Ti dopant and the Mo in the matrix. The work of Yildirim *et al*. showed a correlation between differing bond lengths and increased anharmonicity of phonon modes.[49] This suggested that the V has greater anharmonicity than Ti. The V dopant also has a weaker binding energy than Ti (-7.15 eV compared to -7.44 eV) implying a lower sound velocity. For these reasons, we expect the nature of phonon transport in these two systems to differ.
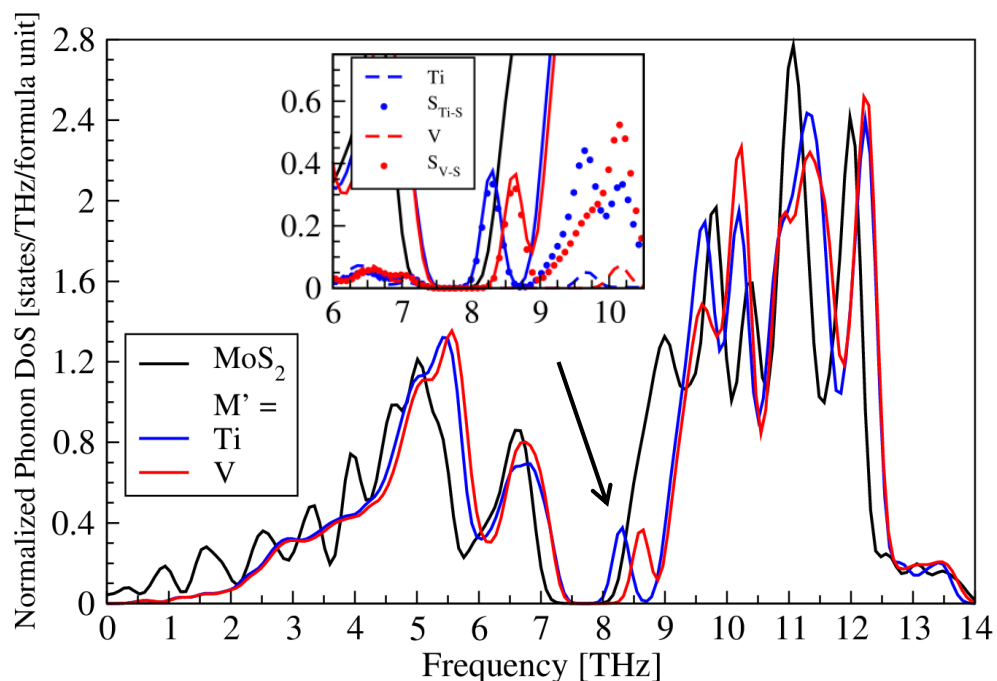
Figure 6.9. **Total phonon DoS calculated for MoS$_2$ doped with 2.083 at.% Ti (blue) and 2.083 at.% V (red). The black plot represents pure MoS$_2$. Data is shown normalized per formula unit. Insert compares these results against the partial contributions from the dopant atoms (dashed lines) and S atoms bonded to the dopants (circles), focusing on the frequency gap region.**

Interestingly, the source of the mid-gap state is actually not the V and Ti atoms but instead the S atoms immediately neighboring the dopant site. The insert in Figure 6.9 shows the partial phonon DoS contributions from the dopant atoms individually as well as the 6 S atoms coordinated about the dopant. In both cases, the mid-gap peak is predominantly composed of those neighboring S atoms. This indicates that the nature of the M'-S bond differs from that of the Mo-S bond. Each of these results reveals significant alterations to the phonon properties of 2D MoS$_2$ upon Ti-/V-doping. With the potential increase in phonon mode scattering and reduction in phonon lifetimes, one could infer a corresponding reduction in κ_l.

6.4 Conclusion

DFT-based calculations were conducted to investigate the effects of metal-site substitutional dopants on structural, energetic, electrical, transport, and phonon properties of 2D MX_2. The supercell approach was employed to simulate various concentrations of Ti dopants on MoS_2. We found that increasing dopant concentration (8.333 at.% Ti) does not greatly distort the 2D MoS_2 structure. The defects were found to be effectively isolated at a concentration of 2.083 at.% Ti when their separation was about 12.8 Å. The effect of various dopants were screened at this concentration having the chemical formula $M'M_{15}X_{32}$ (M' = Mo, Ni, Sc, Ti, V, or W; M = Mo or W; and X = S, Se, or Te). The dopants mostly exhibit minimal structural distortion on 2D MX_2 with the exception of Ni and Sc. Comparison of their geometry effects and binding energies suggests that their atomic radii may have a larger impact on dopant stability than their oxidation states. Binding energy results also indicate decreasing overall dopant stability with increasing chalcogen atomic number. Electronic bandgaps generally decrease with increasing Ti concentration, suggesting an increase in electrical conductivity. The general shape of the electronic DoS and phonon DoS results converge with decreasing Ti concentration until 2.083 at.% Ti. Only the W-doped MoX_2 and Mo-doped WX_2 are direct bandgap semiconductors. All other doped systems (with the exception of Sc-doped $MoSe_2$ which has a very small bandgap) introduce mid-gap states on and above E_F implying p-type semiconducting behavior and an increased electrical conductivity. This goes against the doping propensity of MoS_2 which is experimentally determined to be n-type. Even the semiconducting Mo- and W-doped systems mostly have reduced bandgap sizes compared to the undoped systems. The p-type Boltzmann transport properties reveal a significant

reduction in $S^2\sigma$ upon doping, despite many of these structures having small increases in σ. This is due to their reduced S values. Features of the phonon DoS, *e.g.*, acoustic region peak-broadening and narrower frequency gaps, indicate that Ti dopants cause more of a reduction in the lattice thermal conductivity of 2D MoS_2 than the V dopants. However, the shorter bond lengths about the V dopant and weaker covalent bonds suggest greater phonon anharmonicity, reducing the lattice thermal conductivity. This work explores various dopants and their effects on 2D MX_2 structures which is useful for guiding development of these materials for electronic and energy applications.

<div align="center">

Acknowledgements

</div>

References

(1)   Shishidou, T.; Freeman, A. J.; Asahi, R. Effect of GGA on the half-metallicity of the itinerant ferromagnet CoS2. *Phys Rev B* **2001**, *64*, 180401.

(2)   Ogawa, S. Magnetic-Properties of 3d Transition-Metal Dichalcogenides with the Pyrite Structure. *J Appl Phys* **1979**, *50*, 2308.

(3)   Ataca, C.; Sahin, H.; Ciraci, S. Stable, Single-Layer MX2 Transition-Metal Oxides and Dichalcogenides in a Honeycomb-Like Structure. *Journal of Physical Chemistry C* **2012**, *116*, 8983.

(4)   Rasmussen, F. A.; Thygesen, K. S. Computational 2D Materials Database: Electronic Structure of Transition-Metal Dichalcogenides and Oxides. *Journal of Physical Chemistry C* **2015**, *119*, 13169.

(5)   Butler, S. Z.; Hollen, S. M.; Cao, L. Y.; Cui, Y.; Gupta, J. A.; Gutierrez, H. R.; Heinz, T. F.; Hong, S. S.; Huang, J. X.; Ismach, A. F.; Johnston-Halperin, E.; Kuno, M.; Plashnitsa, V. V.; Robinson, R. D.; Ruoff, R. S.; Salahuddin, S.; Shan, J.; Shi, L.; Spencer, M. G.; Terrones, M.; Windl, W.; Goldberger, J. E. Progress, Challenges, and Opportunities in Two-Dimensional Materials Beyond Graphene. *Acs Nano* **2013**, *7*, 2898.

(6)   Gong, C.; Colombo, L.; Wallace, R. M.; Cho, K. The Unusual Mechanism of Partial Fermi Level Pinning at Metal-MoS2 Interfaces. *Nano Lett* **2014**, *14*, 1714.

(7)   Wang, Q. H.; Kalantar-Zadeh, K.; Kis, A.; Coleman, J. N.; Strano, M. S. Electronics and optoelectronics of two-dimensional transition metal dichalcogenides. *Nat Nanotechnol* **2012**, *7*, 699.

(8)   Huang, W.; Da, H. X.; Liang, G. C. Thermoelectric performance of MX2 (M = Mo, W; X = S, Se) monolayers. *J Appl Phys* **2013**, *113*, 104304.

(9)   Huang, W.; Luo, X.; Gan, C. K.; Quek, S. Y.; Liang, G. C. Theoretical study of thermoelectric properties of few-layer MoS2 and WSe2. *Physical Chemistry Chemical Physics* **2014**, *16*, 10866.

(10)   Lee, C.; Hong, J.; Whangbo, M. H.; Shim, J. H. Enhancing the Thermoelectric Properties of Layered Transition-Metal Dichalcogenides 2H-MQ(2) (M = Mo, W; Q = S, Se, Te) by Layer Mixing: Density Functional Investigation. *Chem Mater* **2013**, *25*, 3745.

(11)   Gu, X. K.; Yang, R. G. Phonon transport in single-layer transition metal dichalcogenides: A first-principles study. *Appl Phys Lett* **2014**, *105*, 131903.

(12)   Ganatra, R.; Zhang, Q. Few-Layer MoS2: A Promising Layered Semiconductor. *Acs Nano* **2014**, *8*, 4074.

(13)   Lopez-Sanchez, O.; Lembke, D.; Kayci, M.; Radenovic, A.; Kis, A. Ultrasensitive photodetectors based on monolayer MoS2. *Nat Nanotechnol* **2013**, *8*, 497.

(14)   Baugher, B. W. H.; Churchill, H. O. H.; Yang, Y. F.; Jarillo-Herrero, P. Optoelectronic devices based on electrically tunable p-n diodes in a monolayer dichalcogenide. *Nat Nanotechnol* **2014**, *9*, 262.

(15)   Coleman, J. N.; Lotya, M.; O'Neill, A.; Bergin, S. D.; King, P. J.; Khan, U.; Young, K.; Gaucher, A.; De, S.; Smith, R. J.; Shvets, I. V.; Arora, S. K.; Stanton, G.; Kim, H. Y.; Lee, K.; Kim, G. T.; Duesberg, G. S.; Hallam, T.; Boland, J. J.; Wang, J. J.; Donegan, J. F.; Grunlan, J. C.; Moriarty, G.; Shmeliov, A.; Nicholls, R. J.; Perkins, J. M.; Grieveson, E. M.; Theuwissen, K.; McComb, D. W.; Nellist, P. D.; Nicolosi, V. Two-Dimensional Nanosheets Produced by Liquid Exfoliation of Layered Materials. *Science* **2011**, *331*, 568.

(16)   Kam, K. K.; Parkinson, B. A. Detailed Photocurrent Spectroscopy of the Semiconducting Group-Vi Transition-Metal Dichalcogenides. *J Phys Chem-Us* **1982**, *86*, 463.

(17)   Mak, K. F.; Lee, C.; Hone, J.; Shan, J.; Heinz, T. F. Atomically Thin MoS2: A New Direct-Gap Semiconductor. *Phys Rev Lett* **2010**, *105*, 136805.

(18)   Kuc, A.; Zibouche, N.; Heine, T. Influence of quantum confinement on the electronic structure of the transition metal sulfide TS2. *Phys Rev B* **2011**, *83*, 245213.

(19)   Splendiani, A.; Sun, L.; Zhang, Y. B.; Li, T. S.; Kim, J.; Chim, C. Y.; Galli, G.; Wang, F. Emerging Photoluminescence in Monolayer MoS2. *Nano Lett* **2010**, *10*, 1271.

(20)   Yin, Z. Y.; Li, H.; Li, H.; Jiang, L.; Shi, Y. M.; Sun, Y. H.; Lu, G.; Zhang, Q.; Chen, X. D.; Zhang, H. Single-Layer MoS2 Phototransistors. *Acs Nano* **2012**, *6*, 74.

(21)   Hicks, L. D.; Dresselhaus, M. S. Effect of Quantum-Well Structures on the Thermoelectric Figure of Merit. *Phys Rev B* **1993**, *47*, 12727.

(22)   Hicks, L. D.; Dresselhaus, M. S. Thermoelectric Figure of Merit of a One-Dimensional Conductor. *Phys Rev B* **1993**, *47*, 16631.

(23)   Mahan, G. D.; Sofo, J. O. The best thermoelectric. *P Natl Acad Sci USA* **1996**, *93*, 7436.

(24)   Zahid, F.; Lake, R. Thermoelectric properties of Bi2Te3 atomic quintuple thin films. *Appl Phys Lett* **2010**, *97*, 212102.

(25)   Wickramaratne, D.; Zahid, F.; Lake, R. K. Electronic and thermoelectric properties of few-layer transition metal dichalcogenides. *J Chem Phys* **2014**, *140*, 124710.

(26)   Hochbaum, A. I.; Chen, R. K.; Delgado, R. D.; Liang, W. J.; Garnett, E. C.; Najarian, M.; Majumdar, A.; Yang, P. D. Enhanced thermoelectric performance of rough silicon nanowires. *Nature* **2008**, *451*, 163.

(27)   Boukai, A. I.; Bunimovich, Y.; Tahir-Kheli, J.; Yu, J. K.; Goddard, W. A.; Heath, J. R. Silicon nanowires as efficient thermoelectric materials. *Nature* **2008**, *451*, 168.

(28)   Williamson, I.; Correa Hernandez, A.; Wong-Ng, W.; Li, L. High-Throughput Computational Screening of Electrical and Phonon Properties of Two-Dimensional Transition Metal Dichalcogenides. *JOM* **2016**, *68*, 2666.

(29)   Graedel, T. E.; Harper, E. M.; Nassar, N. T.; Nuss, P.; Reck, B. K. Criticality of metals and metalloids. *P Natl Acad Sci USA* **2015**, *112*, 4257.

(30)   Zhou, Y. G.; Su, Q. L.; Wang, Z. G.; Deng, H. Q.; Zu, X. T. Controlling magnetism of MoS2 sheets by embedding transition-metal atoms and applying strain. *Physical Chemistry Chemical Physics* **2013**, *15*, 18464.

(31)   Cheng, Y. C.; Zhu, Z. Y.; Mi, W. B.; Guo, Z. B.; Schwingenschlogl, U. Prediction of two-dimensional diluted magnetic semiconductors: Doped monolayer MoS2 systems. *Phys Rev B* **2013**, *87*, 100401.

(32)   Ramasubramaniam, A.; Naveh, D. Mn-doped monolayer MoS2: An atomically thin dilute magnetic semiconductor. *Phys Rev B* **2013**, *87*, 195201.

(33)   Saab, M.; Raybaud, P. Tuning the Magnetic Properties of MoS2 Single Nanolayers by 3d Metals Edge Doping. *Journal of Physical Chemistry C* **2016**, *120*, 10691.

(34)   Chen, Y. F.; Xi, J. Y.; Dumcenco, D. O.; Liu, Z.; Suenaga, K.; Wang, D.; Shuai, Z. G.; Huang, Y. S.; Xie, L. M. Tunable Band Gap Photoluminescence from Atomically Thin Transition-Metal Dichalcogenide Alloys. *Acs Nano* **2013**, *7*, 4610.

(35)   Suh, J.; Park, T. E.; Lin, D. Y.; Fu, D. Y.; Park, J.; Jung, H. J.; Chen, Y. B.; Ko, C.; Jang, C.; Sun, Y. H.; Sinclair, R.; Chang, J.; Tongay, S.; Wu, J. Q. Doping against the Native Propensity of MoS2: Degenerate Hole Doping by Cation Substitution. *Nano Lett* **2014**, *14*, 6976.

(36)   Hsu, W. K.; Zhu, Y. Q.; Yao, N.; Firth, S.; Clark, R. J. H.; Kroto, H. W.; Walton, D. R. M. Titanium-doped molybdenum disulfide nanostructures. *Advanced Functional Materials* **2001**, *11*, 69.

(37)   Deepak, F. L.; Cohen, H.; Cohen, S.; Feldman, Y.; Popovitz-Biro, R.; Azulay, D.; Millo, O.; Tenne, R. Fullerene-like (IF) NbxMo1-xS2 nanoparticles. *J Am Chem Soc* **2007**, *129*, 12549.

(38)   Sun, Q. C.; Yadgarov, L.; Rosentsveig, R.; Seifert, G.; Tenne, R.; Musfeldt, J. L. Observation of a Burstein-Moss Shift in Rhenium-Doped MoS2 Nanoparticles. *Acs Nano* **2013**, *7*, 3506.

(39)   Yadgarov, L.; Rosentsveig, R.; Leitus, G.; Albu-Yaron, A.; Moshkovich, A.; Perfilyev, V.; Vasic, R.; Frenkel, A. I.; Enyashin, A. N.; Seifert, G.; Rapoport, L.; Tenne, R. Controlled Doping of MS2 (M=W, Mo) Nanotubes and Fullerene-like Nanoparticles. *Angew Chem Int Edit* **2012**, *51*, 1148.

(40)   Kresse, G.; Furthmuller, J. Efficient iterative schemes for ab initio total-energy calculations using a plane-wave basis set. *Phys Rev B* **1996**, *54*, 11169.

(41)   Perdew, J. P.; Burke, K.; Ernzerhof, M. Generalized gradient approximation made simple. *Phys Rev Lett* **1996**, *77*, 3865.

(42)   Blöchl, P. E. Projector augmented-wave method. *Phys Rev B* **1994**, *50*, 17953.

(43)   Kresse, G.; Joubert, D. From ultrasoft pseudopotentials to the projector augmented-wave method. *Phys Rev B* **1999**, *59*, 1758.

(44)   Liechtenstein, A. I.; Anisimov, V. I.; Zaanen, J. Density-functional theory and strong interactions: Orbital ordering in Mott-Hubbard insulators. *Phys Rev B* **1995**, *52*, R5467.

(45)   Madsen, G. K. H.; Singh, D. J. BoltzTraP. A code for calculating band-structure dependent quantities. *Computer Physics Communications* **2006**, *175*, 67.

(46)   Parlinski, K.; Li, Z. Q.; Kawazoe, Y. First-principles determination of the soft mode in cubic ZrO2. *Phys Rev Lett* **1997**, *78*, 4063.

(47)   Togo, A.; Tanaka, I. First principles phonon calculations in materials science. *Scripta Mater* **2015**, *108*, 1.

(48)   Zhang, H. J.; Lee, G.; Cho, K. Thermal transport in graphene and effects of vacancy defects. *Phys Rev B* **2011**, *84*, 115460.

(49)   Yildirim, T.; Gulseren, O.; Lynn, J. W.; Brown, C. M.; Udovic, T. J.; Huang, Q.; Rogado, N.; Regan, K. A.; Hayward, M. A.; Slusky, J. S.; He, T.; Haas, M. K.; Khalifah, P.; Inumaru, K.; Cava, R. J. Giant anharmonicity and nonlinear electron-phonon coupling in MgB2: A combined first-principles calculation and neutron scattering study. *Phys Rev Lett* **2001**, *87*, 037001.

CHAPTER SEVEN: HETEROSTRUCTURE EFFECTS ON STRUCTURAL, ELECTRICAL, AND PHONON PROPERTIES OF TWO-DIMENSIONAL TRANSITION METAL DICHALCOGENIDES

The formation of a lateral heterostructure between 2D TMDs has promising optical and electronic applications and remains a relatively unexplored area for materials-by-design.[1] First-principles calculations[2] and experimental results[3,4] show a type II (staggered) band alignment between 2D MoS_2 and WS_2 which has potential for optoelectronic applications. In this chapter, the heterostructure interface between 2D MoS_2 and 2D MS_2 (M = Cr, Sc, Ti, and W) are investigated for structural, energetic, electronic, and phonon effects. The physical features of the transition metals along with the geometric and electronic structures of the pure constituent 2D TMDs play large roles in the stability of the heterostructure and the interfacial properties.

7.1 Computational Methods

Structural and energetic calculations were performed using VASP within the framework of DFT.[5] PAW pseudopotentials[6,7] were used along with spin-dependent GGA exchange correlation functionals defined by the PBE formalism.[8] The plane-wave basis sets were expanded to a cutoff of 400 eV. Fermi surface broadening was handled with a Gaussian smearing of 0.05 eV and structures were relaxed until residual forces were reduced to 0.01 eV/Å. To replicate the ideal 2D structure and avoid spurious image interaction, a vacuum space > 16 Å was inserted between periodic sheets. DFT+U[9] was

employed to handle strong correlation effects in the electronic structure calculations. On-site Coulomb potentials of $U = 5.0$, 4.38, 3.0, 8.0, and 8.0 eV were used for Cr, Mo, Sc, Ti, and W, respectively, while 1.0 eV was used for all J values. Brillouin zone integration was handled using a Γ-centered 3x9x1 k-point mesh for electronic structure calculations.

To calculate the phonon properties of a material, second-order force constants must first be generated. This was handled using DFPT within the VASP code.[10] These force constants were then used to generate phonon DoS plots[11] and used as inputs into the Atomistic Green's Function (AGF) code. The AGF code calculates the phonon transmission function $\Xi(\omega)$ for the interface of two materials and the transmission coefficient for individual phonon modes. To calculate the phonon transmission function, the system is partitioned into three components: the semi-infinite left lead, the interface region and the semi-infinite right lead. The AGF describes phonon propagation across the interface region and is calculated from the force constant matrices associated with the aforementioned components. The transmission function $\Theta(\omega)$, which corresponds to the total phonon transmission across the interface region, is computed from the AGF and depends on the phonon dispersion of the leads and the atomistic structure of the interface. Given $\Theta(\omega)$, the thermal boundary conductance (TBC) can be computed using the following expression[12]

$$G(T) = \frac{1}{2\pi} \int_0^\infty d\boldsymbol{\omega} \hbar \boldsymbol{\omega} \frac{dN(\omega,T)}{dT} \Theta(\omega) \tag{7.1}$$

where N and T are the Bose-Einstein function and the temperature, respectively. In addition, recent extensions to the AGF method by Ong and Zhang[12] have also enabled the efficient computation of transmission coefficients for individual phonon modes. These extensions allow for a more detailed and deeper analysis of the distribution of transmitted

phonon modes and its connection to the phonon dispersion of the constituent materials on both sides of the interface.

To minimize error in this chapter, DFT input parameters were optimized through convergence tests similar to that of Sections 4.2, 5.2, and 6.2. The only literature values available for result validation came from pure MS_2 band alignments[13,14] and MoS_2-WS_2 heterostructure bandgap type.[15]

7.2 Results

To broaden the understanding of 2D TMD heterostructures and the factors that contribute to their structural stability, electronic properties, and phonon properties, each result in this work was compared to the physical features of the transition metals. Similar to our previous work,[16] we focused on the most common oxidation state, atomic masses,[17] and atomic radii[18] of the individual transition metals. By comparing these physical features between Mo and M, and analyzing their effects on structure, electronic, and phonon properties, we identified key parameters that govern 2D TMD lateral heterostructures.

<u>Structural Features</u>

DFT-based calculations were conducted to determine the structural effects of forming a heterostructure between 2D MoS_2 and 2D MS_2 (M = Cr, Sc, Ti, and W), see Figure 7.1Figure 7.. Table 7.1 lists the structural mismatch values, Δa and $\Delta d_{S\text{-}S}$, between adjacent structures. Each of these values were derived from the pure 2D TMD lattice constant, a, and S-S separation distance, $d_{S\text{-}S}$ (refer to Figure 6.2), according to the following equations.

$$\Delta a = \left| \frac{a_{MoS2} - a_{MS2}}{a_{MoS2}} \right| * 100\% \tag{7.2}$$

$$\Delta d_{S-S} = \left| \frac{d_{S-S}^{MoS2} - d_{S-S}^{MS2}}{d_{S-S}^{MoS2}} \right| *100\% \qquad (7.3)$$

The W system has the lowest Δa and Δd_{S-S} values meaning its interface will have the least amount of strain compared to the other transition metals in this work. The Cr and Ti systems each had similar Δa values and the Cr had lower Δd_{S-S} (6.09% compared to 8.74%) so the MoS_2-CrS_2 interface has slightly less strain than that of the MoS_2-TiS_2. The pure ScS_2 system has a large difference in lattice constant and S-S distance compared to MoS_2 and likewise has the largest mismatch values. Sc has the lowest atomic mass and largest atomic radius of all transition metals investigated. However, compared to the features of Mo, W has a larger mass difference and Cr has a larger radius difference than Sc suggesting that the size and mass of the metal are not the critical features for minimizing mismatch. The Sc does have the largest difference in oxidation state (+3 compared to Mo's +6) which is likely a dominant factor for finding a stable heterostructure.
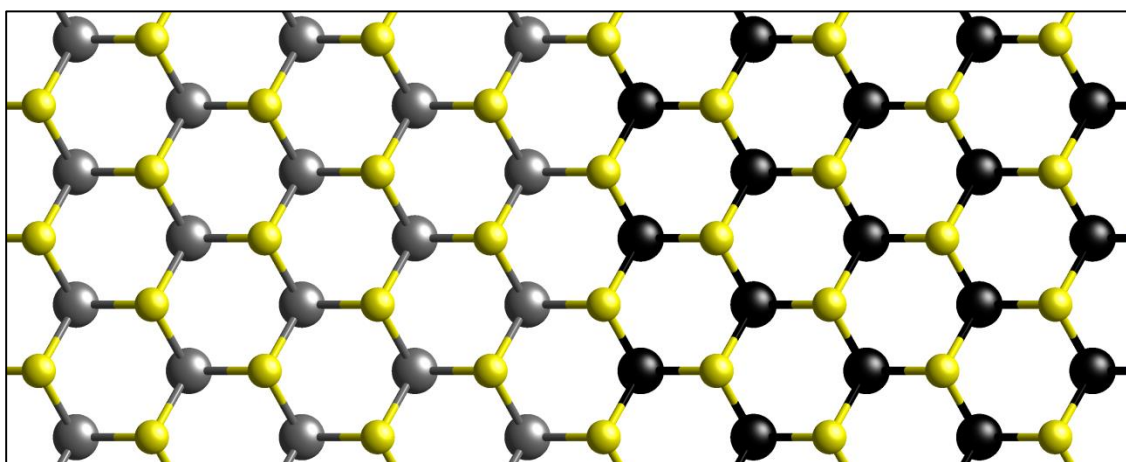
Figure 7.1. **Schematic of the MoS_2-MS_2 (M = Cr, Sc, Ti, or W) heterostructure where the Mo, S, and M atoms are depicted using gray, yellow, and black spheres, respectively**

Table 7.1. **Physical features of the transition metals, M, in 2D MoS₂–MS₂ lateral heterostructures. The lattice, Δ*a*, and S-S distance, Δ*d*$_{S-S}$, mismatches are based off of the pure 2D MoS₂ and MS₂ structures. The formation energy and electronic bandgap of the heterostructure is given as *E*$_f$ and *E*$_g$, respectively.**

M				Mismatch		E_f (eV)	E_g (eV)
symbol	common oxidation state	atomic mass[a] (u)	atomic radius[b] (Å)	Δ*a*	Δ*d*$_{S-S}$		
Cr	+6	51.996	0.69	4.44%	6.09%	-0.02	0.97
Sc	+3	44.956	0.885[c]	18.73%	13.42%	4.29	--
Ti	+4	47.88	0.745	4.80%	8.74%	1.54	--
W	+6	183.85	0.80	0.03%	0.38%	-0.32	1.59
Mo	+6	95.94	0.79				

[a]Reference [14]
[b]Reference [15]. Values taken from crystal radii with +4 charge and 6-fold coordination.
[c]Value for +3 charge

To analyze the thermodynamic stability of these heterostructures, the formation energy, E_f, was calculated for each system. This was done according to the following equation:

$$E_f = E_{tot}^{het.} - n_{uc}^{MoS2} E_{uc}^{MoS2} - n_{uc}^{MS2} E_{uc}^{MS2} \qquad (7.4)$$

where $E_{tot}^{het.}$ is the total energy of the MoS₂-MS₂ heterostructure, E_{uc}^{MoS2} and E_{uc}^{MS2} are the energies of a single unit cell of pure 2D MoS₂ and MS₂, respectively, and n_{uc}^{MoS2} and n_{uc}^{MS2} are the number of unit cells of each material present in the heterostructure. The system with the largest E_f value is the Sc with 4.29 eV. This indicates that the individual pure substances are more stable than the heterostructure, which requires energy in order to form. This is expected given the large difference in oxidation state between Mo and Sc as well as large mismatch in both lattice constant and S-S distance. With a negligible E_f value, the MoS₂-CrS₂ heterostructure is predicted to be stable whereas MoS₂-TiS₂, which

has an E_f of 1.54 eV, is not. With relatively similar mismatch values and atomic mass and weight, the improved stability of the Cr system is likely due to its oxidation state. The only heterostructures that do not yield positive E_f values are Cr and W which are also those that have the same oxidation state as Mo (+6). These results indicate that the formation of stable 2D MS_2 lateral heterostructures is strongly dependent on the oxidation states between transition metals in two compositions.

<u>Electronic Properties</u>

Electronic DoS calculations were performed for each MoS_2-MS_2 (M = Cr, Sc, Ti, and W) heterostructure and their bandgaps are listed in Table 7.1. The two most stable structures, the systems having Cr and W, are also the only heterostructures that have a bandgap. A more detailed view is provided in Figure 7.2 which depicts the electronic band structure diagrams for the Cr and W systems. The VBM for both structures is similar while the CBM for the W system is about 0.6 eV higher. The MoS_2-WS_2 heterostructure is also a direct bandgap semiconductor with VBM and CBM both occurring at the Γ point. Alternatively, the CBM in the MoS_2-CrS_2 system shifts away from the Γ point (as indicated by the blue arrow in Figure 7.2) towards the K point. This transition from direct to indirect semiconducting behavior must originate from the interface since the pure 2D MoS_2, WS_2, and CrS_2 are all direct bandgap semiconductors.[14,16]
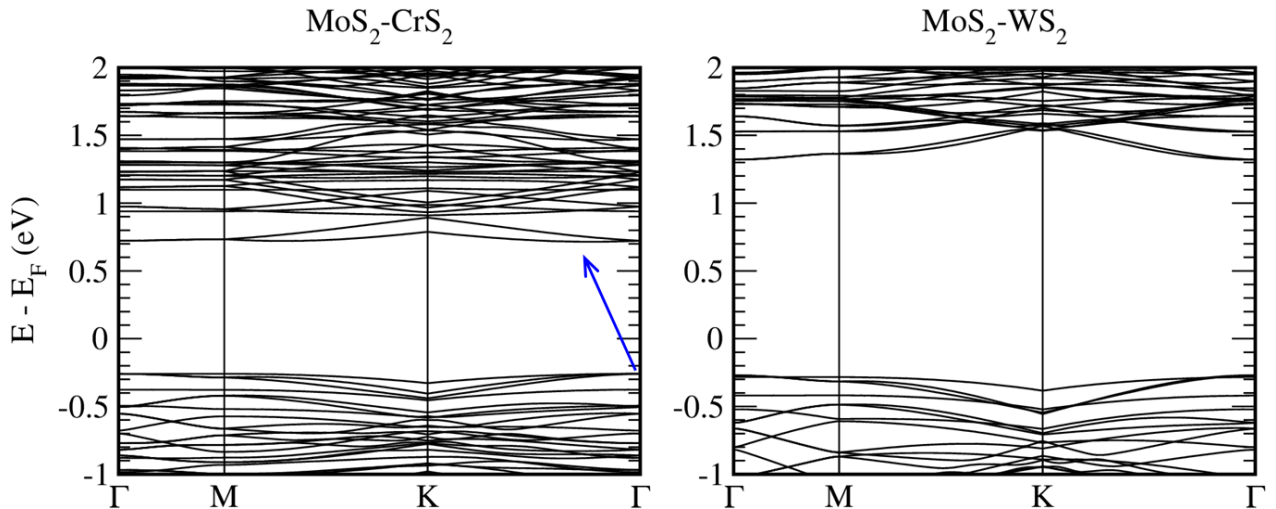
Figure 7.2. Electronic band structure diagrams for MoS₂-CrS₂ and MoS₂-WS₂ lateral heterostructures. The *y*-axis for both plots has been shifted to $E_F = 0$ eV. The MoS₂-WS₂ structure is determined to be a direct semiconductor at the Γ point whereas the lowest conduction band in the MoS₂-CrS₂ structure has shifted slightly towards the K point exhibiting indirect semiconducting behavior (as indicated by the blue arrow).

The bandgap for the MoS₂-CrS₂ system (0.97 eV) is similar to that of the pure 2D CrS₂ compound (0.95 eV) while the MoS₂-WS₂ system (1.59 eV) is smaller than either the pure 2D MoS₂ (1.69 eV) or pure 2D WS₂ (1.85 eV). To clarify this, the band alignments for each of the pure 2D MS₂ systems were plotted in Figure 7.3. The VBM for both CrS₂ and MoS₂ are about -5.80 eV while the CBM of the CrS₂ is significantly lower than that of the MoS₂ (-4.84 eV compared to -4.13 eV). This suggests that the CrS₂ layer in the heterostructure contributes more to the CBM than the MoS₂ layer. It also explains how the bandgap for MoS₂-CrS₂ heterostructure is limited by the bandgap of the pure CrS₂. The MoS₂-WS₂ heterostructure exhibits type II (staggered) band alignment with a bandgap of 1.58 eV.[2,15] This means that the CBM and VBM of one system are each higher than that of the adjacent system. In this case, the CBM/VBM levels for WS₂ (-3.50/-5.35 eV) are each higher than that of MoS₂ (-4.13/-5.82 eV). The VBM of the resulting heterostructure is contributed mostly from the WS₂ layer while the CBM is

contributed from the MoS_2 layer. This results in a reduced bandgap for the heterostructure compared to the individual layers. The difference between the pure WS_2 VBM (-5.35 eV) and the pure MoS_2 CBM (-4.13 eV) is only 1.22 eV, so it was expected that the calculated bandgap of the heterostructure would be around 1.22 eV. However, we calculated a bandgap for the MoS_2-WS_2 heterostructure of 1.59 eV. The orbital overlap for the interface is likely different from that of the pure substances – which have a CBM and VBM originating from the repulsion between anion p and cation d orbitals.[15] The bonding character at the interface plays a crucial role in the electrical properties of the heterostructure. Understanding the correlation between physical features of constituent atoms and the resulting 2D TMD band alignments can guide materials design.
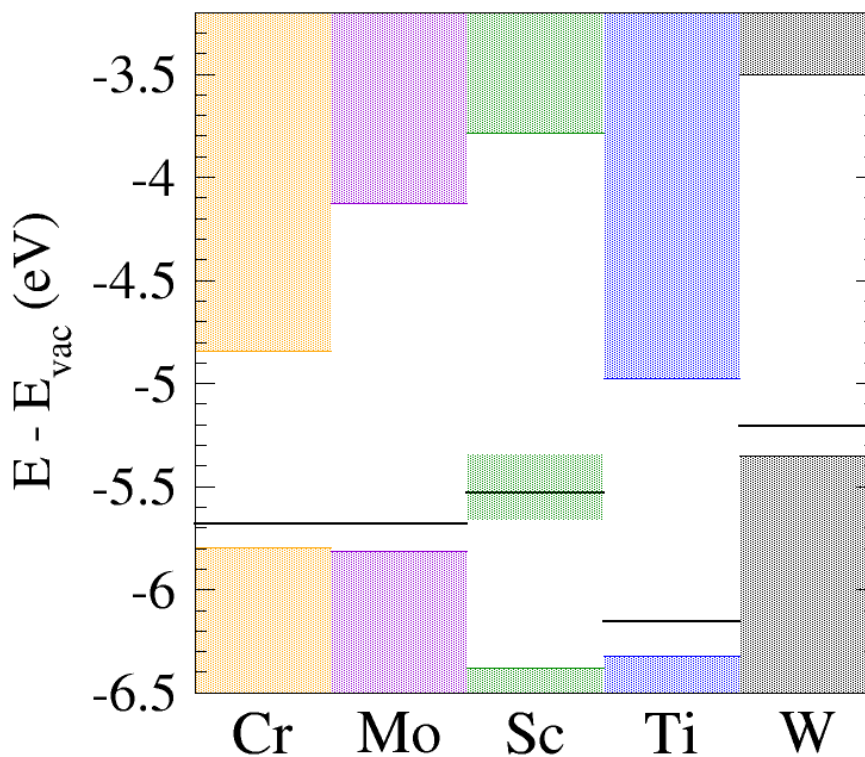
Figure 7.3. **Band alignments for each of the pure 2D MS$_2$ (M = Cr, Mo, Sc, Ti, and W) structures shifted to the vacuum level. Horizontal black lines represent the Fermi level (E_F) for each structure.**

Phonon Properties

Phonon DoS spectra, plotted in Figure 7.4, reveals that the Sc and Ti systems have significant negative (imaginary) phonon frequencies suggesting instability in the structures. These findings are consistent with our E_f results in Table 7.1. Alternatively, the Cr and W heterostructures have negligible negative frequencies and are stable. The Cr has the highest-frequency optical bands among the heterostructures investigated in this work. The W has sharper features and is the only system that has a significant gap between acoustic and optical phonon bands. Previous first-principles calculations have shown a correlation between phonon frequency gaps and high thermal conductivity.[19] This is attributed to fewer and weaker scattering events between acoustic and optical phonon modes that have a large separation in frequency. By this reasoning, the Cr system

which has no frequency gap would be expected to have greater acoustic-optical phonon scattering than W. The calculation of third-order force constants would be required to estimate lattice thermal conductivity and confirm this observation.
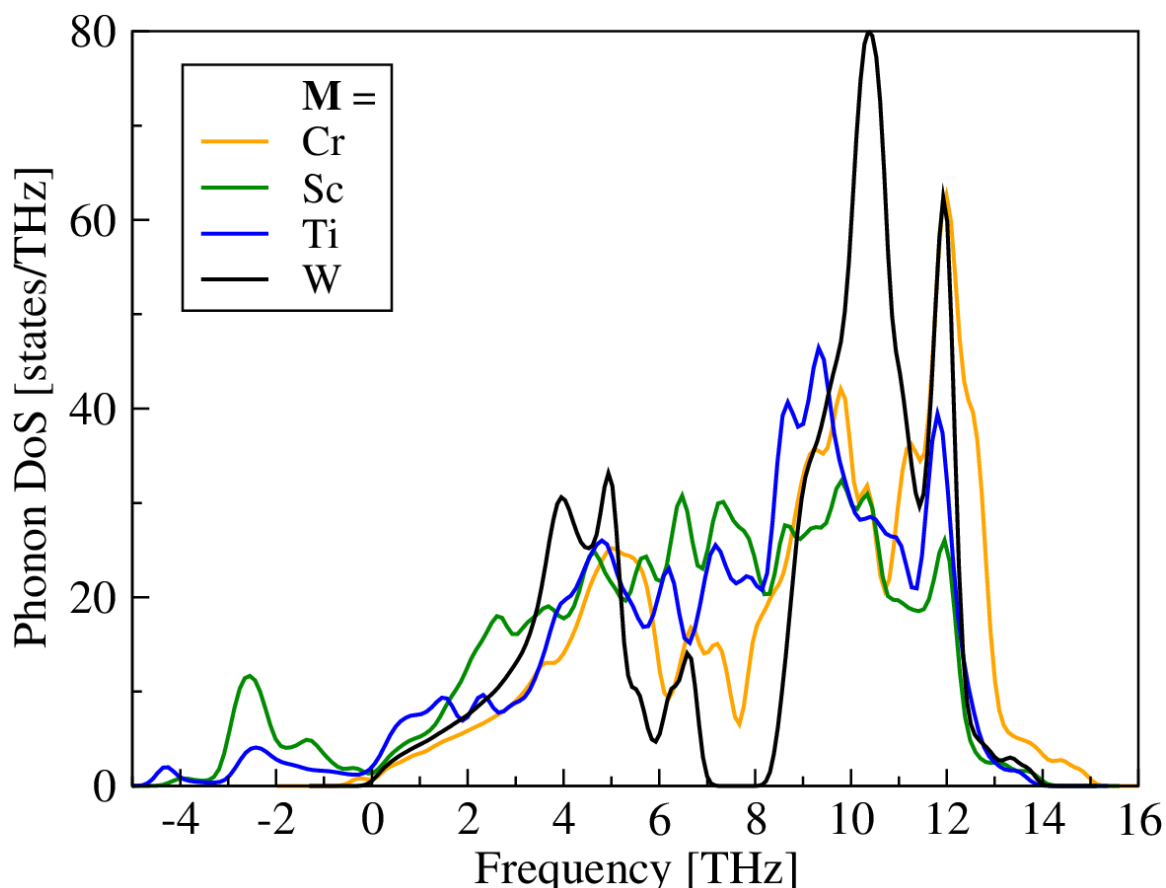
Figure 7.4. **Phonon density of states calculated for each 2D MoS$_2$–MS$_2$ heterostructure where the yellow (Cr), green (Sc), blue (Ti), and black (W) plots represent each respective transition metal, M. Negative (imaginary) phonon frequencies are found for the two least stable (lowest formation energy) heterostructures: M = Sc and Ti.**

Atomistic Green's Function (AGF) Results

Another approach for determining the thermal effects of a heterostructure is through the investigation of the interfacial thermal resistance. This is dependent on the transmission of phonons across the heterojunction. We use the extended AGF to investigate interfacial thermal transport at the MoS$_2$-WS$_2$ interface and the underlying

phonon mechanisms. Using second-order force constants as input into the AGF code, the phonon transmission coefficients can be calculated for each phonon mode in the first Brillouin zone. Each data point in Figure 7.5, which shows the transmission coefficient spectra for the acoustic phonons in MoS_2 and WS_2, represents a phonon mode while the color indicates the transmission coefficient or fraction of energy transmitted across the interface. The gray-shaded points correspond to phonon modes that do not contribute to the interfacial head flux because their group velocities are in the direction away from the interface. Most of the transmission in this heterostructure is contributed by the acoustic phonon modes so, for the sake of brevity, only the transmissions from the three acoustic modes are provided. The left column in Figure 7.5 represents the rightward interfacial heat flux contribution from MoS_2 phonons while the right column represents the leftward interfacial heat flux contribution from WS_2 phonons.
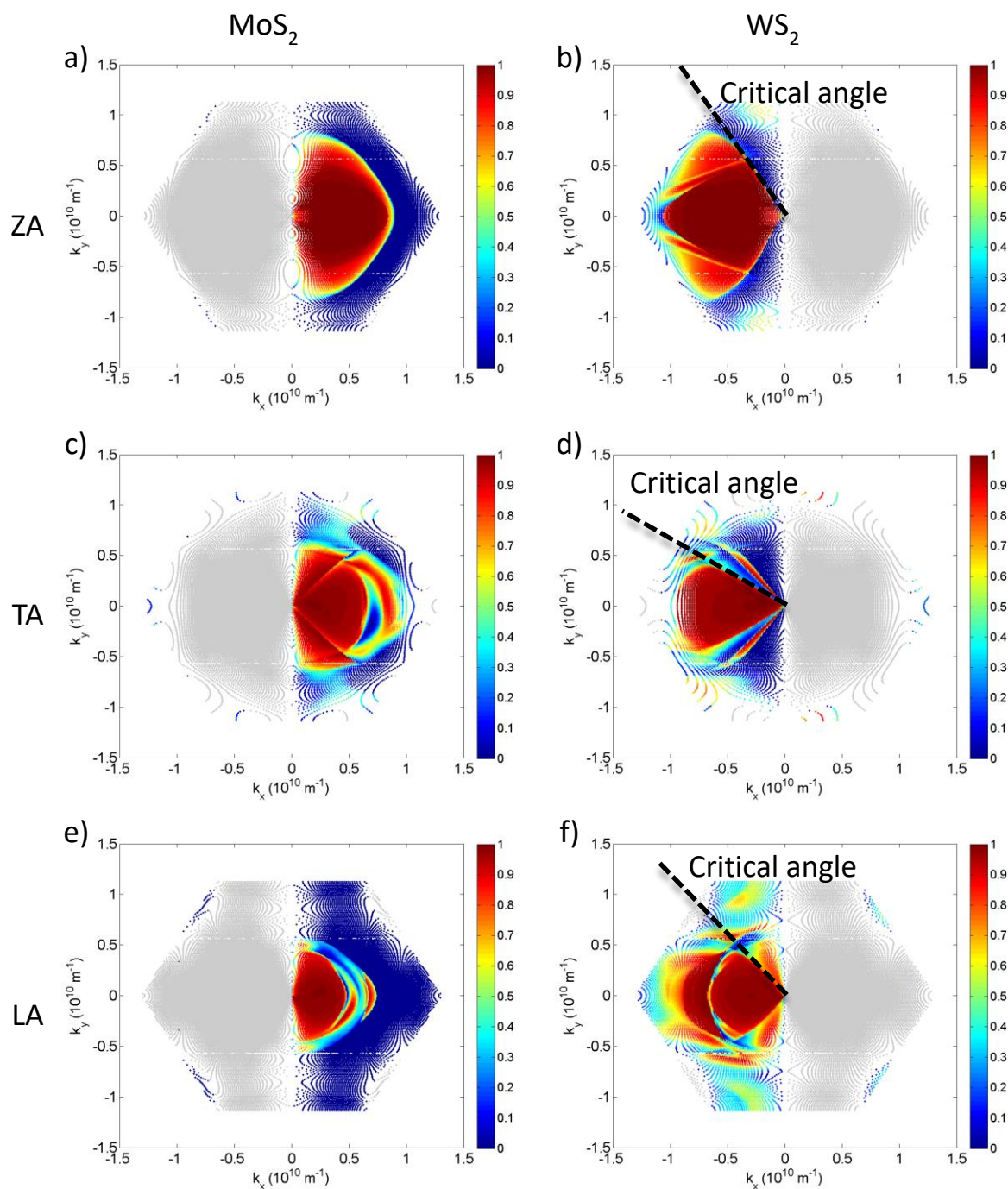
Figure 7.5. **Phonon transmission coefficients across the MoS₂-WS₂ interface for the ZA (a and b), TA (c and d), and LA (e and f) acoustic phonon modes. The left column (a, c, and e) represents MoS₂ phonons contributing to leftward interfacial heat flux whereas the right column (b, d, and f) represents WS₂ phonons contributing to rightward interfacial heat flux.**

In general, the transmission coefficients converge to unity when the wave vectors for the phonons are small, corresponding to long wavelengths and low frequencies. This implies that the interface is highly permeable to the low-frequency, long-wavelength acoustic phonons. However, as we move radially away from the center of the Brillouin zone towards the zone boundaries, the phonon frequencies increase and the associated phonon transmission coefficients become smaller since higher-frequency phonons are strongly scattered by the interface. In addition, a 'critical angle' is observed for phonon transmission from the WS_2 phonons while no such phenomenon is observed for MoS_2 phonons. Beyond this angle, there is no transmission on the WS_2 side. This manifestation of the critical angle is analogous to the critical angle in the refraction of light between two media of different refractive indices and is due to the lower acoustic phonon group velocity in WS_2 which is denser because of the heavier W atoms. The transmission coefficient also depends on the frequency alignment of phonons with similar polarizations in MoS_2 and WS_2. In MoS_2, because its phonon velocities are generally higher, a wider angular distribution of phonon modes contribute to the heat flux while in WS_2, a lower angular distribution of phonon modes are involved in interfacial thermal transport because of the critical angle. Although, a larger portion of the phonon modes with the arc defined by that critical angle are transmitted across the interface.

The TBC, G, relates the interfacial heat flux, Q, to the temperature drop across a boundary, ΔT, according to the following equation:

$$Q = G\Delta T \tag{7.5}$$

For large values of G, the temperature drop across the boundary is small. In Figure 7.6, the total TBC is plotted as a function of temperature up to 500 K. We note that the TBC

increases as a function of temperature because more phonon modes become populated and contribute to interfacial thermal transport at higher temperatures. One advantage of our use of the extended AGF method is that it also allows us to distinguish and quantify the contribution of the phonons by their band indices. In MoS_2 and WS_2, there are 3 atoms in the primitive unit cell and thus a total of 3x3=9 phonon bands (3 acoustic and 6 optical) since each band corresponds to an atomic degree of freedom. Acoustic phonons are expected to contribute more disproportionately to interfacial thermal transport because they have much higher group velocities and are more easily transmitted across the interface. To verify this, we computed the TBC from only the acoustic phonons and from the acoustic and optical phonons (see Figure 7.6). The contribution from the acoustic phonon modes dominates the TBC for all temperatures. At room temperature (300 K), the contribution from the optical phonons, which accounts for the difference between the two curves in Figure 7.6, only comprises about 16% of the TBC, confirming the commonly held assumption that interfacial heat flux is primarily mediated by acoustic phonons.[20] Nonetheless, the optical phonon contribution is not insignificant and can be a source of discrepancy if not included in the computation of the TBC, especially at high temperatures. We also note that the TBC for the MoS_2-WS_2 interface is much lower than that of the graphene/h-BN interface.[12,21] At room temperature, the MoS_2-WS_2 TBC is ~351 $MWK^{-1}m^{-2}$ while the graphene/h-BN TBC is 2.5 $GWK^{-1}m^{-2}$, almost an order of magnitude larger. This is due to the lower acoustic phonon velocities in MoS_2 and WS_2, which limit their maximum interfacial heat flux, compared to graphene and h-BN.

The use of this extended AGF method allows for a thorough analysis of the heat flux across a heterojunction and can further the understanding of transport properties

within these nanostructures. The expansion of this technique towards other 2D TMD

heterostructures will be crucial to develop these materials for energy applications.
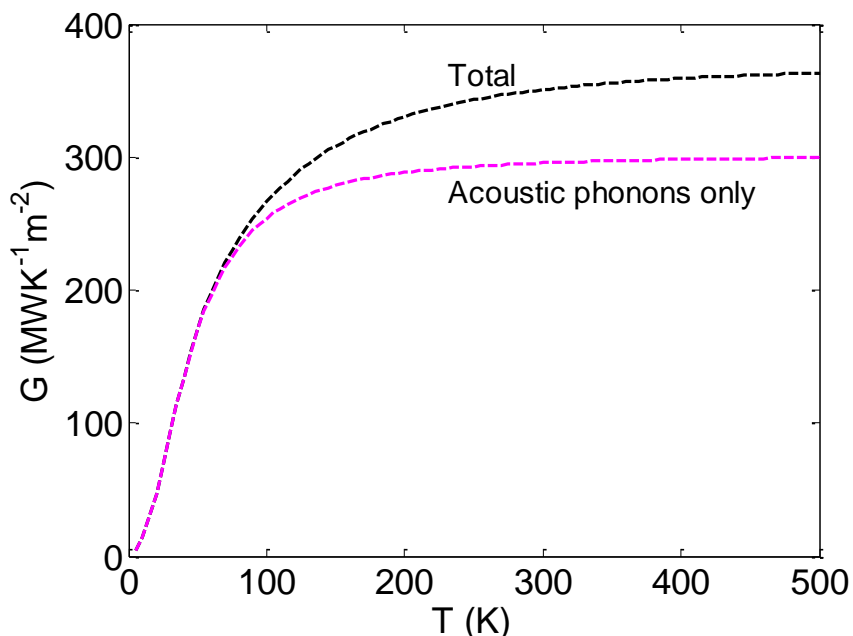
Figure 7.6. **Thermal boundary conductance (TBC) for MoS₂-WS₂ lateral interface. The dotted black plot represents the total TBC for the system and the dotted pink plot represents the TBC contribution from the acoustic phonon modes.**

7.3 Conclusion

DFT calculations were performed to analyze the structural, energetic, electronic,

and phonon effects of a lateral heterostructure formation between 2D MoS_2 and 2D MS_2

(M = Cr, Sc, Ti, or W). The choice of transition metals having similar oxidation states

had a much greater effect on the stability of the heterostructure than the atomic mass,

atomic radius, or mismatch between the TMDs (Δa or Δd_{S-S}). The MoS_2-ScS_2 and MoS_2-

TiS_2 heterostructures were determined to be the least stable systems due to their positive

formation energies (E_f) and negative phonon frequencies. The E_f values for both the

MoS_2-CrS_2 and MoS_2-WS_2 heterostructures are low and neither exhibit significant

negative phonon frequencies, suggesting that both heterostructures are stable. The Cr and

W systems are also the only systems to exhibit an electronic bandgap. The heterostructure bandgaps are determined by the VBM and CBM values from the constituent pure TMDs. The VBMs for both pure CrS_2 and MoS_2 are aligned but the CrS_2 CBM is lower than the MoS_2, so the resulting heterostructure has a bandgap that matches that of the pure CrS_2. However, the MoS_2-WS_2 forms a type II (staggered) alignment so the resulting heterostructure bandgap is smaller than that of either TMD. The MoS_2-WS_2 phonon DoS was found to be the only system with a frequency gap between acoustic and optical bands, suggesting that it experiences the least amount of acoustic-optical phonon scattering among these heterostructures.

Our simulation of the thermal boundary conductance at the MoS_2-WS_2 interface shows that the TBC is dominated by the acoustic phonons and primarily limited by the differences in acoustic phonon velocities between MoS_2 and WS_2. Our results also indicate that the optical phonons have a small but significant contribution to the TBC especially at high temperatures. Compared to the graphene/h-BN interface, our calculated TBC for the MoS_2-WS_2 system is almost an order of magnitude smaller. This is due to the lower acoustic phonon velocities in MoS_2 and WS_2. This may potentially be a source of impediment to efficient heat dissipation in nanoelectronic devices with such interfaces.

References

(1)   Wang, H. T.; Yuan, H. T.; Hong, S. S.; Li, Y. B.; Cui, Y. Physical and chemical tuning of two-dimensional transition metal dichalcogenides. Chem Soc Rev 2015, 44, 2664.

(2)   Wang, Q. W.; Wu, P.; Cao, G. Y.; Huang, M. First-principles study of the structural and electronic properties of MoS2-WS2 and MoS2-MoTe2 monolayer heterostructures. J Phys D Appl Phys 2013, 46, 505308.

(3)   Huang, C. M.; Wu, S. F.; Sanchez, A. M.; Peters, J. J. P.; Beanland, R.; Ross, J. S.; Rivera, P.; Yao, W.; Cobden, D. H.; Xu, X. D. Lateral heterojunctions within monolayer MoSe2-WSe2 semiconductors. Nature Materials 2014, 13, 1096.

(4)   Chen, K.; Wan, X.; Wen, J. X.; Xie, W. G.; Kang, Z. W.; Zeng, X. L.; Chen, H. J.; Xu, J. B. Electronic Properties of MoS2-WS2 Heterostructures Synthesized with Two-Step Lateral Epitaxial Strategy. Acs Nano 2015, 9, 9868.

(5)   Kresse, G.; Furthmuller, J. Efficient iterative schemes for ab initio total-energy calculations using a plane-wave basis set. Phys Rev B 1996, 54, 11169.

(6)   Blöchl, P. E. Projector augmented-wave method. Phys Rev B 1994, 50, 17953.

(7)   Kresse, G.; Joubert, D. From ultrasoft pseudopotentials to the projector augmented-wave method. Phys Rev B 1999, 59, 1758.

(8)   Perdew, J. P.; Burke, K.; Ernzerhof, M. Generalized gradient approximation made simple. Phys Rev Lett 1996, 77, 3865.

(9)   Liechtenstein, A. I.; Anisimov, V. I.; Zaanen, J. Density-functional theory and strong interactions: Orbital ordering in Mott-Hubbard insulators. Phys Rev B 1995, 52, R5467.

(10)   Parlinski, K.; Li, Z. Q.; Kawazoe, Y. First-principles determination of the soft mode in cubic ZrO2. Phys Rev Lett 1997, 78, 4063.

(11)   Togo, A.; Oba, F.; Tanaka, I. First-principles calculations of the ferroelastic transition between rutile-type and CaCl(2)-type SiO(2) at high pressures. Phys Rev B 2008, 78, 134106.

(12)   Ong, Z. Y.; Zhang, G. Efficient approach for modeling phonon transmission probability in nanoscale interfacial thermal transport. Phys Rev B 2015, 91, 174302.

(13)   Ataca, C.; Sahin, H.; Ciraci, S. Stable, Single-Layer MX2 Transition-Metal Oxides and Dichalcogenides in a Honeycomb-Like Structure. Journal of Physical Chemistry C 2012, 116, 8983.

(14)   Rasmussen, F. A.; Thygesen, K. S. Computational 2D Materials Database: Electronic Structure of Transition-Metal Dichalcogenides and Oxides. Journal of Physical Chemistry C 2015, 119, 13169.

(15)   Kang, J.; Tongay, S.; Zhou, J.; Li, J. B.; Wu, J. Q. Band offsets and heterostructures of two-dimensional semiconductors. Appl Phys Lett 2013, 102, 012111.

(16)   Williamson, I.; Hernandez, A. C.; Wong-Ng, W.; Li, L. High-throughput computational screening of electrical and phonon properties of two-dimensional transition metal dichalcogenides. JOM 2016.

(17)   Sansonetti, J. E.; Martin, W. C.; July 1, 2009 ed.; National Institute of Standards and Technology: http://www.nist.gov/pml/data/handbook/, 2014.

(18)   Shannon, R. D. Revised Effective Ionic-Radii and Systematic Studies of Interatomic Distances in Halides and Chalcogenides. Acta Crystallogr A 1976, 32, 751.

(19)   Gu, X. K.; Yang, R. G. Phonon transport in single-layer transition metal dichalcogenides: A first-principles study. Appl Phys Lett 2014, 105, 131903.

(20)   Swartz, E. T.; Pohl, R. O. Thermal-Boundary Resistance. Reviews of Modern Physics 1989, 61, 605.

(21)   Zhu, T. S.; Ertekin, E. Phonon transport on two-dimensional graphene/boron nitride superlattices. Phys Rev B 2014, 90, 195209.

CHAPTER EIGHT: CONCLUSIONS

The research goal for this dissertation is to generate large data sets and analyze trends and relationships between structure, properties, and performance of skutterudite and 2D TMD compounds for electronic and energy applications. By understanding these design principles, we can tailor the structures to enhance and optimize material properties and performance. These materials are known to have good intrinsic electrical properties and tailorable structures making them excellent candidates for a number of energy and electrical applications. First-principles DFT calculations were employed to investigate skutterudites and 2D TMDs and how their electrical and phonon properties can be enhanced by two main structural changes: (1) doping and (2) the formation of a heterojunction.

Chapter One provides an overview of the goal and motivation for this dissertation. Four main objectives were used to achieve the goal including: (1) understanding dopant effects on skutterudite materials, (2) screening 2D TMD materials compositions, (3) understanding the effects of substitutional dopants in 2D TMDs, and (4) evaluating the impact of a lateral heterojunction between 2D TMDs. A summary of the dissertation, including the published works produced from this work, is also included in this chapter.

Chapter Two explains the background for each materials system investigated and highlights their applications and current state of research. Skutterudites are a widely studied class of materials because of their low-cost, easy processing, and intrinsic transport properties. Currently of interest for thermoelectric applications, their open,

cage-like structures offer a unique opportunity for materials-by-design exploration. Much work has been done to investigate the effects of single-, double-, and multi-filled skutterudites which show promising enhancement in electrical and thermal properties. Substitutional doping has been shown to further enhance these properties, yet a fundamental investigation of fillers and substitutions is still required to fully optimize skutterudite compounds. TMDs also have large degrees of freedom in their structure including structure type, dimensionality, and composition. Single-layer, 2D TMD sheets have attracted interest as candidates for magnetics, electronics, optoelectronics, catalysis, and thermoelectric applications. Quantum confinement effects and diffusive boundary scattering can be exploited for improved electrical and transport properties. Smaller device features have shown promising enhancement of FETs. There remain three key areas for property improvement for these materials: identification of optimum compositions, substitutional doping, and heterostructure formation. A thorough investigation of these factors is necessary for further development of 2D TMD materials.

Chapter Three reviews the theoretical and computational methods employed in this dissertation. It explains how DFT is used to calculate the electronic and geometric ground state of a material through total energy minimization calculations. The resulting geometric, electrical, and phonon structures can be used to investigate the effects of dopants and heterostructures. Band energies can be expanded through the use of star functions to determine semi-classic transport coefficients while DFPT-based force constant calculations can be used to calculate phonon DoS, transmission coefficients across an interface, and thermal boundary conductance.

Chapter Four investigates the structural, electrical, and thermal properties of two dopant types in skutterudite compounds: filler atoms and Sb-site substitution. Both the incorporation of Ca/Ce filler atoms in $FeSb_3$ and Te/Ge substitution in $CoSb_3$ decrease the lattice constant for the compounds. Te/Ge substitution leads to distortion in the pnictogen rings and a break in the cubic symmetry of the compound. Both dopants cause an increase in electrical conductivity through the reduction in electronic bandgap while Te/Ge substitution also causes a transition from direct to indirect semiconducting behavior for $x = 3$. Phonon band broadening is observed in both doped systems and each are assumed to exhibit acoustic-mode dominated lattice thermal conductivity. Of the substitution concentrations, $x = 3$ has the lowest acoustic phonon dispersion gradient implying that it experiences the lowest lattice thermal conductivity. This is consistent with experimental measurements. The presence of either dopant has shown enhancements in the thermoelectric properties of these skutterudite compounds. This computational study provided insight into experimental observations, advanced the understanding of dopant effects on skutterudite materials.

Chapter Five covers high throughput screening of 2D TMD compositions based on electrical and phonon properties. With the large number of potential compositions, focus was narrowed to three chalcogens (S, Se, Te) and six transition metals (Mo, Ni, Sc, Ti, V, and W) based on environmental implications, supply risk, and vulnerability to supply restrictions known as "criticality scores." These scores allowed for the exploration of compositional effects while focusing on materials that are better-suited for development. The physical features of constituent transition metals (*e.g.*, atomic mass, atomic radius, and oxidation state) have significant impact on the overall properties of the

2D TMD. For instance, as the metal mass increases, the *n*-type power factor, $S^2\sigma$, and

phonon frequency gap increases. Also, increasing the radius causes an increase in 2D

TMD layer thickness and Seebeck coefficient, *S*. The results of Chapter Five help

identify principles for optimizing 2D TMD compositions for desired performance.

Chapter Six investigates the metal-site substitution effects on 2D TMD properties.

These were analyzed with respect to their effect on structural, energetic, electrical,

transport, and phonon properties. The overall dopant effect was found to decrease with

concentration until they converge at 2.083 at.% where the dopants are effectively

isolated. Structural distortion, dopant binding energy, electron DoS, and phonon DoS

confirm this convergence at 2.083 at.%. Therefore, this concentration was used to

investigate dopant type with a large number of different compositions corresponding to

the formula, $M'M_{15}X_{32}$ (M' = Mo, Ni, Sc, Ti, V, or W; M = Mo or W; and X = S, Se, or

Te). Most structures exhibit minimal distortion upon doping except those doped with Ni

or Sc. These are also the metals with the lowest oxidation states (+2 and +3, respectively,

compared to the host metals' +6). Only the W-doped MoX_2 and the Mo-doped WX_2

compounds consistently exhibit semiconducting behavior and have the largest *p*-type

$S^2\sigma$. Also, the presence of W and Mo dopants in the selenide and telluride compounds

increase σ by as much as 60% (at carrier concentration $N = 10^{14}$ holes/cm^2). However,

due to the reduction in *S*, the $S^2\sigma$ decreases for each doped system investigated. Phonon

DoS results show acoustic region peak-broadening and narrower frequency gaps for Ti-

doped MoS_2 suggesting a reduction in phonon lifetimes and increased acoustic-optical

phonon scattering. A large amount of information on doping effects was discussed in this

chapter which is useful for guiding the development of doped 2D TMD materials.

Chapter Seven highlights the formation of a lateral heterostructure between 2D

MoS_2 and 2D MS_2 (M = Cr, Sc, Ti, and W). The structural, energetic, electronic, and

phonon effects of this interface were investigated. The difference in oxidation state

between the Mo and the M atoms plays a larger role in the heterostructure stability than

the atomic mass or radius. The least stable systems – the ones having the highest

formation energy and presence of negative (imaginary) phonon frequencies – involved Sc

(+3) and Ti (+4) which had the largest difference in oxidation state compared to Mo (+6).

Alternatively, the Cr and W, which both have +6 oxidation states, had low formation

energies and no significant negative phonon frequencies suggesting mechanical stability.

These were also the only systems to exhibit semiconducting behavior. The VBM and

CBM for the heterostructures were found to be determined by the band alignment of the

pure 2D TMD constituents. For the Cr system, the pure CrS_2 VBM is aligned with that of

the pure 2D MoS_2 while the CrS_2 CBM is significantly lower. This causes the resulting

bandgap of the heterostructure to be equivalent to the pure CrS_2. The W system, however,

forms a type II (staggered) alignment making the resulting heterostructure bandgap (1.59

eV) smaller than the bandgap of either constituent (1.69 eV for 2D MoS_2 and 1.85 eV for

2D WS_2). The phonon DoS results for the W system are also the only ones that exhibit a

frequency gap between acoustic and optical phonon bands, suggesting that the MoS_2-WS_2

heterostructure experiences the lowest acoustic-optical phonon mode scattering among

these heterostructures. The TBC of the MoS_2-WS_2 interface was found to be dominated

by the acoustic phonons and limited by the difference in acoustic phonon velocities

between the MoS_2 and WS_2. Our calculated TBC for this system is almost an order of

magnitude smaller than that of the graphene/*h*-BN heterostructure due to the reduced acoustic phonon velocities of the TMDs.

This dissertation offers an analysis of the structure-property relationship for a wide range of properties on bulk skutterudite and 2D TMD materials. An investigation of filler and substitutional dopant effects on skutterudite compounds provide insight to advance the understanding of electrical and phonon properties that experiments could not measure. This also offered a good benchmark material for developing a modeling scheme that was employed for 2D TMD materials. The three key outcomes of this work are: (1) a high throughput approach to compute and analyze electrical and phonon properties, (2) a screening method for investigating 2D TMD materials and highlighting preferred compositions, and (3) design principles for predicting structures and properties to guide experiments. The high throughput approach include: DFT-based total energy minimization calculations to investigate the geometric, energetic, and electronic structure data; Boltzmann transport theory, in combination with electronic band energies, to estimate σ, S, and $S^2\sigma$ values; DFPT-based second-order force constant calculations to determine phonon dispersion and DoS spectra; and the AGF method, using force constants as input, to compute interfacial heat flux, phonon transmission coefficients, and TBC. The input parameters and structures for each model were optimized prior to calculation. DFT-based input parameters include cutoff energies, *k*-point meshes, partial-occupancy smearing widths, and on-site DFT+U terms. For phonon calculations, supercell sizes were similarly determined through convergence tests. Literature values were used where available to compare resultant lattice constants, bond lengths/angles, bandgaps, and phonon dispersion data. This approach mitigated errors in the model,

which can now be used to analyze electrical and phonon properties of similar systems, in a fraction of the time. Due to this work, dozens of 2D TMD structures can be analyzed within days, whereas initial optimization calculations for each structure took up to one week to compute. The design principles determined in this dissertation compare known literature values for common oxidation states, atomic masses, and atomic radii of constituent transition metal atoms to the properties of resulting 2D TMD compounds. These principles include:

- Metal-site dopant stability is dependent on matching atomic radii between the dopant and solvent metal

- Dopants can increase electrical conductivity in TMD selenides and tellurides but decrease $S^2\sigma$

- The choice of similar oxidation states between transition metals in adjacent TMDs is crucial for lateral heterostructure stability.

Future work includes a broader investigation of 2D TMD heterostructures and the effects of structure, composition, and transition metal physical features on stability, electrical, and phonon properties. The primary areas of interest for this investigation include the effects of: (i) structure type (*i.e.*, 2H- vs. 1T-type), (ii) composition – including choice of transition metal and chalcogen, (iii) heterostructure interface between TMDs and other 2D structures such as graphene, and (iv) alternate heterostructure interfaces such as vertical 2D TMD stacking. Further property improvements can be achieved by combining these structures with substitutional doping. Overall, these materials offer great potential for materials-by-design exploration and understanding their

structural, electrical, and phonon properties are essential for advancement towards

commercial applications.